The Far Reach of Megathrust Earthquakes: Evolution of Stress, Deformation and Seismicity Following the 2004 Sumatra-Andaman Rupture

by

Kelly Wiseman

A dissertation submitted in partial satisfaction of the
requirements for the degree of
Doctor of Philosophy

in

Earth and Planetary Science

in the

Graduate Division

of the

University of California, Berkeley

Committee in charge:

Professor Roland Bürgmann, Chair
Professor Michael Manga
Professor George Johnson

Fall 2012

The Far Reach of Megathrust Earthquakes: Evolution of Stress, Deformation and Seismicity Following the 2004 Sumatra-Andaman Rupture

Abstract

The Far Reach of Megathrust Earthquakes: Evolution of Stress, Deformation and Seismicity Following the 2004 Sumatra-Andaman Rupture

by

Kelly Wiseman

Doctor of Philosophy in Earth and Planetary Science

University of California, Berkeley

Professor Roland Bürgmann, Chair

Starting with the 2004 M_w 9.2 megathrust event, Southeast Asia has been home to an exceptional amount of seismic activity over the past eight years. The series of megathrust earthquakes have been imperfect dominoes, rupturing the northernmost section of the Sunda subduction zone in 2004, then the Nias segment next in line to the south in 2005, followed by the Bengkulu earthquake ∼750 km further south in 2007. The Bengkulu earthquake skipped over the northern Mentawai segment, which has not ruptured in a great event since 1797. However, the subduction zone has not been silent is this section. Analysis of focal mechanisms and geodetic data reveals the reactivation of the Mentawai backthrust system in the overriding plate, and a large, deep earthquake near the city of Padang in 2009 is shown through finite fault inversions and aftershock analysis to have obliquely ruptured the subducting slab. At the same time, the entire region spanning from the Indian Ocean, through the trench and forearc islands, and throughout Thailand has been aseismically deforming in response to the stress changes in the mantle following the megathrust earthquakes. Geodetic observations of postseismic deformation during the first five years following the 2004 earthquake have shown that the far-field regions of Thailand and the Malay Peninsula have moved more postseismically than coseismically, peaking at ∼0.4 m of horizontal displacement in Phuket. In 2012, the stress changes associated with this continued postseismic deformation, along with the initial push from the megathrust earthquakes, appears to have triggered the largest instrumentally recorded strike-slip earthquake. This was a complex earthquake, consisting of four conjugate fault segments, that ruptured the diffuse India-Australia plate boundary zone. Understanding how the faults interact throughout the subduction system, from the incoming plate, to the slab, to the megathrust interface, and overriding plate is an essential part of determining the future seismic hazard for Southeast Asia.

Contents

List of Figures **iv**

List of Tables **vii**

1 Introduction **1**

2 Stress and Seismicity Changes on the Sunda Megathrust Preceding the 2007 M_w 8.4 Earthquake **5**

2.1 Abstract . . . 5
2.2 Introduction . . . 5
2.3 Stress Modeling Method and Data . . . 8
2.3.1 Coseismic and Postseismic Deformation Calculations . . . 8
2.3.2 Input Source Models . . . 9
2.3.3 Coulomb Failure Stress-Change Calculations . . . 10
2.3.4 Megathrust Geometry . . . 10
2.4 Stress Modeling Results . . . 12
2.4.1 Interseismic Loading Rate . . . 12
2.4.2 Stress Change from the 2004 Sumatra-Andaman Earthquake . . . 16
2.4.3 Stress Change from the 2005 Nias Earthquake . . . 18
2.4.4 Stress Change from the 2000 Enggano Earthquake . . . 18
2.5 Seismicity Rate Comparison Method and Data . . . 20
2.5.1 Seismicity Rate Change Calculation . . . 20
2.5.2 Earthquake Catalog . . . 22
2.6 Seismicity Rate Comparison Results . . . 24
2.6.1 Seismicity Rate Changes from 2005 to 2007 . . . 24
2.6.2 Seismicity in the 2007 Epicentral Region . . . 24
2.7 Discussion . . . 27
2.7.1 Differentiating Contributions from Different Postseismic Processes . . . 27
2.7.2 Influence of Fault Friction . . . 27
2.7.3 The Skipped 1797 Rupture Patch . . . 30
2.7.4 Delayed Dynamic Long-Distance Triggering . . . 33
2.8 Conclusions . . . 34

3 Another Potential Source of Destructive Earthquakes and Tsunami Offshore of Sumatra **35**
3.1 Abstract . . . 35
3.2 Introduction . . . 35
3.3 Cluster Seismic Activity . . . 36
3.4 GPS Measurements . . . 40
3.5 Deformation Modeling . . . 40
3.6 Megathrust-Backthrust Stress Interaction . . . 45
3.7 Discussion . . . 47
3.8 Conclusions . . . 49

4 Source Model of the 2009 M_w 7.6 Padang Intraslab Earthquake and its Effect on the Sunda Megathrust **50**
4.1 Abstract . . . 50
4.2 Introduction . . . 50
4.3 Data . . . 53
4.3.1 Broadband Waveforms . . . 53
4.3.2 Geodetic Data . . . 54
4.4 Inversion Method . . . 55
4.4.1 Model Geometry . . . 55
4.4.2 Green's Functions . . . 57
4.4.3 Finite Fault Inversion Method . . . 59
4.5 Inversion Results . . . 59
4.5.1 Seismic Waveform Inversions . . . 59
4.5.2 Geodetic Inversions . . . 64
4.5.3 Joint Inversions . . . 64
4.6 Aftershocks . . . 68
4.7 Stress Interactions Within the Subduction Zone . . . 72
4.7.1 Induced Stresses in the Slab . . . 72
4.7.2 Induced Stresses on the Megathrust . . . 75
4.8 Discussion . . . 77
4.9 Conclusions . . . 80

5 Stress Triggering of the Great Indian Ocean Strike-slip Earthquakes in a Diffuse Plate Boundary Zone **82**
5.1 Abstract . . . 82
5.2 Introduction . . . 82
5.3 Seismicity in the Northern Wharton Basin . . . 84
5.4 The April 11 2012 Ruptures . . . 85
5.5 Stress Changes Induced by the Megathrust Earthquakes . . . 88
5.6 Discussion and Conclusions . . . 95

6 Viscoelastic Relaxation in a Heterogenous Earth from Transient Deformation in Southeast Asia Following the 2004 Sumatra-Andaman Earthquake 99
6.1 Abstract . . . 99
6.2 Introduction . . . 100
6.3 Geodetic Observations . . . 100
6.3.1 Near-field Observations . . . 102
6.3.2 Intermediate-field Observations . . . 102
6.3.3 Far-field observations . . . 105
6.4 Viscoelastic Modeling Method . . . 105
6.4.1 Finite Element Model . . . 105
6.4.2 Model Geometry and Rheology . . . 110
6.4.3 Input Source Models . . . 112
6.5 Model results . . . 117
6.5.1 1-D Model . . . 117
6.5.2 Slab Model . . . 117
6.5.3 Strong Ocean Model . . . 117
6.5.4 Back-arc Model . . . 120
6.6 Discussion and Conclusions . . . 123

7 Conclusion and Recommendations 125

List of Figures

1.1 Overview map 2

2.1 Tectonic overview of the Sunda subduction zone 7
2.2 Earthquake locations 11
2.3 Comparison of Sunda plate-interface geometries 13
2.4 The effect of receiver fault geometry 14
2.5 Interseismic model for the 2007 hypocentral region. 15
2.6 Coulomb failure stress changes on the Sunda megathrust resulting from the 2004 Sumatra-Andman earthquake 17
2.7 Coulomb failure stress changes on the Sunda megathrust resulting from the 2005 Nias earthquake 19
2.8 Coulomb failure stress changes on the Sunda megathrust resulting from the 2000 earthquake 21
2.9 2000 poroelastic rebound models 22
2.10 Accumulated CFS change at the 2007 hypocenter since the time of the 2000 earthquake 23
2.11 Seismicity catalog comparisons 25
2.12 Beta values showing the relative change in seismicity following the 2004 earthquake compared with the time period $1980 - 2004$ 26
2.13 Seismicity in the 2007 epicentral region 28
2.14 Beta values showing the relative change in seismicity compared with the time period $1980 - 1999$ 29
2.15 Total stress changes resulting from the combination of the 2000, 2004, and 2005 coseismic and postseismic deformation on the Sunda megathrust 31
2.16 Accumulated stress change at the 2007 hypocenter since the time of the 2000 earthquake 32

3.1 Earthquake cluster location map 37
3.2 Regional seismicity between 1976 to 2010 38
3.3 Cluster GPS time series 41
3.4 Deformation observations and slip models 44
3.5 Stress transfer from the megathrust to the backthrust 46
3.6 Historic earthquake models 48

4.1 Context of the 30 September 2009 earthquake . . . 52
4.2 Velocity waveforms . . . 54
4.3 Comparison of GPS data and joint model displacement vectors . . . 56
4.4 Seismic sensitivity tests . . . 60
4.5 Rupture velocity sensitivity analysis for Collings earth model . . . 61
4.6 Comparison of displacement data and synthetics for the seismic finite fault models using the Collings earth model . . . 62
4.7 Comparison of slip distributions for seismic finite fault inversions . . . 63
4.8 Preferred finite-fault models . . . 65
4.9 Effect of Model Smoothing . . . 66
4.10 Comparison of GPS data and GPS-only model displacement vectors . . . 67
4.11 GPS data and model fits . . . 69
4.12 Point source model comparison for GPS data . . . 70
4.13 Point souce model comparison for seismic data . . . 71
4.14 Aftershock activity following the 2009 mainshock . . . 73
4.15 Intraslab seismicity . . . 74
4.16 Stress changes resolved on the EWNP fault geometry . . . 76
4.17 Stress changes resulting from slip on the EWNP and NSNP . . . 78
4.18 Stress changes resolved on the megathrust . . . 81

5.1 Tectonic overview of the India-Australia Plate . . . 83
5.2 Northern Wharton Basin seismicity . . . 86
5.3 Recent stress changes in the Indian Ocean . . . 87
5.4 One month of seismic activity following the 2012 mainshock . . . 89
5.5 Recent stress changes in the Indian Ocean resolved on the NNE-SSW plane . 90
5.6 Recent stress changes in the Indian Ocean using alternate megathrust slip models . . . 91
5.7 Recent stress changes in the Indian Ocean using alternate megathrust slip models resolved on the NNE-SSW plane . . . 92
5.8 The effects of source depth . . . 93
5.9 The effects of source depth resolved on the NNE-SSW plane . . . 94
5.10 The effects of receiver depth resolved on the WNW-ESE plane . . . 95
5.11 The effects of receiver depth resolved on the NNE-SSW plane . . . 96
5.12 Stress time series . . . 97

6.1 Viscoelastic modeling overview map . . . 101
6.2 Andaman Islands time series . . . 103
6.3 Sumatran Islands time series . . . 104
6.4 Sumatran time series . . . 106
6.5 Thai time series . . . 107
6.6 Malay Peninsula time series . . . 108

6.7 Indian Ocean and Indian time series 109
6.8 Earth model schematics 111
6.9 Earth models schematics 113
6.10 3-D model geometry 114
6.11 FEM Mesh 115
6.12 Fits to coseismic data 116
6.13 5 years of viscoelastic relaxation using the 1-D Earth Model 118
6.14 5 years of viscoelastic relaxation using the Slab Earth Model 119
6.15 5 years of viscoelastic relaxation using the Strong Ocean Earth Model 120
6.16 5 years of viscoelastic relaxation using the Back-arc Earth Model 122
6.17 CARI time series comparison 124

List of Tables

2.1 2004 average coseismic CFS changes under the Sumatran Forearc Islands . . 12

3.1 Backthrust cluster focal mechanisms 39
3.2 Backthrust model fault geometries 43

4.1 The Lange earth model 58
4.2 The Collings earth model 58
4.3 CFS Changes at the 2009 Padang earthquake hypocenter 75

Chapter 1

Introduction

Subduction zones are home to a majority of the world's earthquakes, including the largest, and most hazardous events - megathrust earthquakes. Megathrust earthquakes are plate interface events, that occur when the upper plate is thrust above the subducting oceanic plate, releasing the bulk of the relative plate motion within the subduction zone. The hazards associated with megathrust earthquakes include both shaking damage and tsunamis.

The 2004 Sumatra-Andaman megathrust earthquake was the largest earthquake since the 1960's and the first M 9+ event to occur during the era of modern seismology and space geodesy. This earthquake produced measurable static surface displacements at distances as large as 4500 km away from the rupture. The earthquake lasted for 8-10 minutes, and ruptured a 1300-1500 km long segment of the Sunda megathrust [Shearer and Bürgmann, 2010]. The vertically upthrusted seafloor spawned a tsunami that devastated northern Sumatra, with maximum wave run-up heights of 50 m in Aceh, and damaged coastal regions around the Indian Ocean basin [Choi et al., 2006]. The combined affect of the severe shaking and tsunami led to an estimated 230,000 casualties and 1.7 million displaced persons in fourteen countries in South Asia and East Africa [`http://earthquake.usgs.gov/earthquakes/eqinthenews/2004/us2004slav/#summary`].

The 2004 earthquake statically triggered additional plate interface events, including the 2005 M_w 8.7 Nias earthquake. The Nias earthquake occurred 3 months after the Sumatra-Andman earthquake, and $\sim$200 km south of the 2004 epicenter. Two and a half years later in September 2007, the M_w 8.4 Bengkulu earthquake ruptured the southern portion of the Mentawai segment of the Sunda megathrust. The Bengkulu earthquake initiated $\sim$750 km south of the Nias earthquake epicenter, skipping over a segment of the megathrust that has not ruptured in a megathrust event since 1797. In Chapter 2, and published in Wiseman and Bürgmann [2011], I analyze stress changes induced by both the coseismic deformation and early postseismic deformation following the 2004 and 2005 earthquakes to ascertain whether the Bengkulu earthquake was also a triggered event.

The 2004 Sumatra-Andaman earthquake not only induced additional plate interface

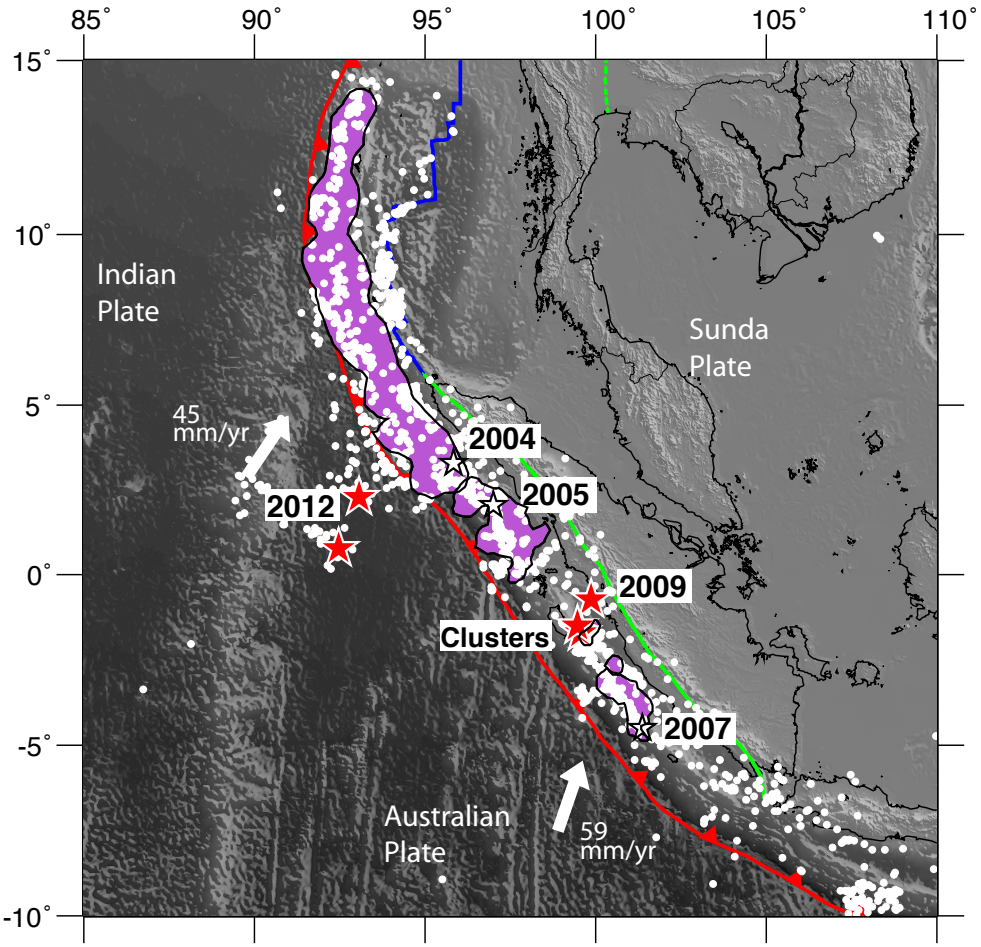

Figure 1.1: Overview map that highlights the locations of all of the earthquakes discussed in this dissertation. The megathrust ruptures zones are shaded purple [Chlieh et al., 2007; Konca et al., 2008, 2007], and the epicenters of the non-interface earthquakes are marked with red stars. All of the magnitude 5+ earthquakes following the 2004 Sumatra-Andaman earthquake through April 30, 2012 are marked with white circles [NEIC catalog].

events, but it also affected seismictiy rates throughout the entire subduction zone. In this dissertation, I analyze several exotic earthquakes that occurred during the eight years following the 2004 megathrust earthquake, including two clusters of backthrust earthquakes in the upper plate, a M_w 7.6 oblique earthquake that ruptured the subducting slab, and two M 8+ strike-slip earthquakes that ruptured the incoming oceanic plate.

In Chapter 3, and published in Wiseman et al. [2011], I analyze two clusters of shallow, moderate magnitude, reverse mechanism earthquakes that occurred in 2005 and 2009 between the Mentawai Islands and western Sumatra. I use Global Positioning System (GPS) data from the Sumatran GPS Array (SuGAr) to show that these clusters have reactivated a 900-km long backthrust fault arising from the Sunda megathrust. These two clusters represent the first activity on the backthrust in more than 30 years. I also reevaluate existing coral vertical deformation data from the Mentawai Islands, that previous researchers had attributed to megathrust ruptures. The sparse paleogeodetic data leaves open the possibility of historic magnitude 7-8+ backthrust earthquakes, which would pose an additional seismic and tsunami hazard to the coastal communities of central Sumatra.

In Chapter 4, and published in Wiseman et al. [2012], I investigate the source of the 2009 M_w 7.6 Padang earthquake. This deep earthquake had an unusual oblique-reverse mechanism, and ruptured the down-going Sunda slab. This earthquake is located just north of the backthrust clusters, below the skipped portion of the Sunda megathrust that has not ruptured since 1797. I invert GPS data and broadband regional seismic-displacement waveforms to try and resolve the causative focal plane of this deep earthquake and determine its source parameters. The aftershock pattern proves to be the best dataset for distinguishing the causative focal plane, and they preferentially align with the E-W plane. I also model the coseismic static stress changes induced by the 2009 earthquake and determine that it has moved closer to failure the deepest portion of the overlying Sunda megathrust, that is late in its seismic cycle.

In Chapter 5, and published in Wiseman and Bürgmann [2012], I analyze the relation between the 2004 and 2005 megathrust earthquakes and the two great magnitude 8+ strike-slip earthquakes that ruptured in April 2012, off the west coast of northern Sumatra, in the broadly distributed India-Australia plate boundary zone. The mainshock involved sequential ruptures of multiple fault planes oriented nearly perpendicular to each other. I determine that the adjacent 2004 megathrust earthquake statically loaded the northern Wharton Basin oceanic lithosphere on both of the 2012 mainshock fault plane orientations, both coseismically and postseismically, through viscoelastic relaxation of the asthenosphere. The earthquake activity in the oceanic plate was greatly enhanced following the megathrust ruptures, and included several M 7+ events before the 2012 earthquakes.

Given the tremendous size of the 2004 earthquake, accelerated asthenospheric flow is

expected to perturb the regional deformation field for many decades to come. In Chapter 6, I explore a variety of viscoelastic relaxation models, using a finite element model approach, ranging from a simple 1-D layered earth model to a 3-D model that includes an elastic subducting slab and a low-viscosity back-arc spreading center, to determine the effects on crustal deformation in the near-to-far field range. The Sunda-Andaman subduction zone is unusual in that it has forearc islands located between the trench and the island arc. This allows me to compare my viscoelastic models with postseismic GPS data from the near-field, on these islands located directly above the megathrust fault, and the intermediate to far-field data from the Sumatra mainland, Thailand, the Malay peninsula and India.

In Chapter 7, I present conclusions and recommendations for further research.

Chapter 2

Stress and Seismicity Changes on the Sunda Megathrust Preceding the 2007 M_w 8.4 Earthquake

2.1 Abstract

The Bengkulu M_w 8.4 earthquake on 12 September 2007, close in time and space to the 2004 M_w 9.2 Sumatra-Andaman and 2005 M_w 8.7 Nias megathrust events, suggests that it could be a triggered earthquake. It was located in the southern portion of the historic 1833 M_w 8.9 rupture. However, it appears perplexing that the portion of the Sunda subduction zone between the Nias and Bengkulu rupture patches, which last ruptured in a 1797 M_w 8.7 event, did not recur first. Coulomb failure stress (CFS) modeling of the 2004 and 2005 megathrust earthquakes and subsequent postseismic relaxation processes fails to explain why the 2007 patch ruptured before the northern 1797 segment. Surprisingly, the much smaller 2000 M_w 8.0 Enggano earthquake produced a much larger positive CFS change at the 2007 hypocenter and may help to explain the southern location of the 2007 earthquake. Investigation of changes in seismicity rates in the region following the 2004−2005 events shows that the megathrust earthquakes may have dynamically triggered slip near the northern end of the 2007 rupture zone. A large increase in seismicity levels following the 2000 earthquake may also have influenced the eventual initiation point of the 2007 earthquake. Regrettably, the section of the Sunda megathrust near Siberut that last ruptured in 1797 still poses a great seismic hazard to the region as the only segment not to have ruptured in the sequence of twenty-first century megathrust earthquakes.

2.2 Introduction

The 2004 M_w 9.2 Sumatra-Andaman earthquake was the largest in 40 yr and extended for $1300 - 1500$ km [Shearer and Bürgmann, 2010]. It apparently triggered a second great megathrust event, the 28 March 2005 M_w 8.7 Nias earthquake, which initiated just ∼200 km south of the 2004 epicenter [McCloskey et al., 2005; Nalbant et al., 2005; Pollitz et al., 2006a].

Earthquake triggering is the process by which static and/or dynamic stress changes associated with an earthquake can induce or retard seismic activity in the surrounding region or trigger other earthquakes at great distances [Freed, 2005]. The 12 September 2007 Bengkulu M_w 8.4 earthquake initiated ∼750 km south of the 2005 epicenter, and was followed 12 hr later by a deeper Mw 7.9 aftershock (Figure 2.1,Figure 2.2a). Their occurrence, close in time and space to the 2004 Sumatra-Andaman earthquake, the 2005 Nias earthquake, and the 2000 M_w 8.0 Enggano earthquake, suggest the possibility of these being triggered events.

The 2007 earthquakes ruptured a portion of the 700-km-long Mentawai patch, a section of the Sunda megathrust that has been observed to fail in sequences of earthquakes about every two centuries for the past 700 yr [Sieh et al., 2008]. The last earthquake supercycle ended in a pair of magnitude 8+ events in 1797 and 1833. The 1797 earthquake ruptured directly south of the 2005 Nias rupture patch, which apparently also slipped in 1861, while the 1833 segment is farther south and overlaps with the 2007 events (Figure 2.1). The study of coral growth histories offshore Sumatra by Natawidjaja et al. [2006] indicates that interseismic strain accumulated along the 1833 segment has approached levels relieved in the historic earthquake. In addition, the accumulated interseismic strain appears to have exceeded previously relieved levels along the 1797 segment [Chlieh et al., 2008]. Although there are moment magnitude uncertainties ranging from 0.2 to 0.3 for the historic 1797 and 1833 source models, historic reports and coral microatoll data indicate that the 1833 rupture was larger, along with being the more recent event, and should therefore rerupture after the 1797 segment.

Previous investigations of coseismic and viscoelastic deformation following the 2004−2005 sequence show that the 1797 segment experienced higher Coulomb failure stress increases (CFS) than the more distant 1833 segment [Nalbant et al., 2005; Pollitz et al., 2006a]. Therefore, assuming that the stress distribution at the time of these events was relatively uniform, it is unclear why the 1797 and northern portion of the 1833 rupture zone did not break before the southern 1833 segment. We model stress changes from coseismic and postseismic processes, including viscoelastic relaxation, afterslip, and poroelastic rebound, in an attempt to find scenarios that can explain why the southern 1833 segment was triggered prior to the 1797 segment. In addition, we investigate the seismicity changes in the years leading up to the 2007 earthquake for alternative triggering evidence.

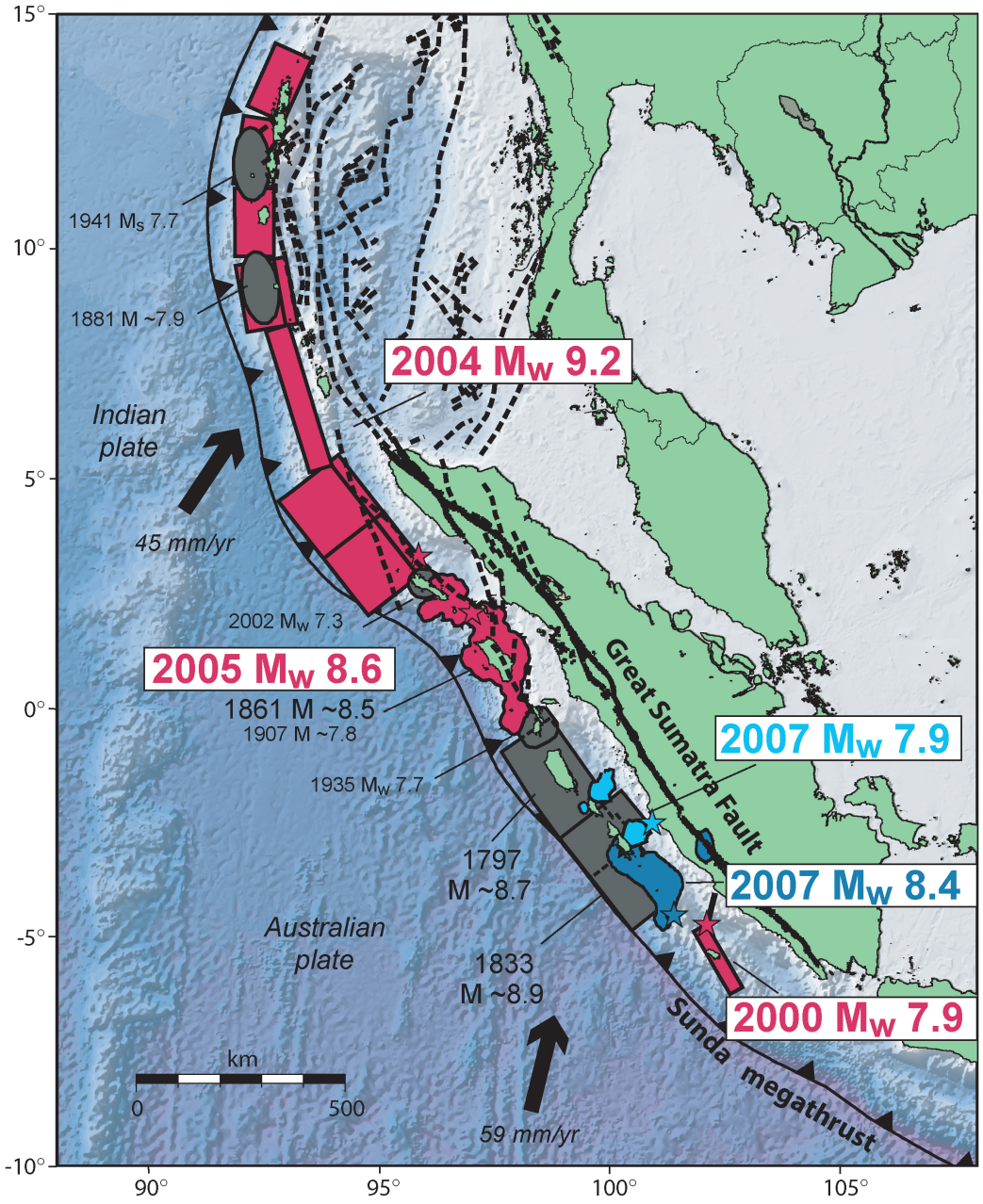

Figure 2.1: Tectonic overview of the Sunda subduction zone. Rupture patches and estimated magnitudes from recent great earthquakes are from Abercrombie et al. [2003]; Banerjee et al. [2007]; Konca et al. [2007] and historic earthquakes are from Briggs et al. [2006]; Natawidjaja et al. [2006]. High-slip patches from the 2007 M_w 8.4 and M_w 7.9 events are from Konca et al. [2008].

2.3 Stress Modeling Method and Data

2.3.1 Coseismic and Postseismic Deformation Calculations

We model the coseismic and postseismic deformation from the 2000, 2004, and 2005 earthquakes, constrained by geodetic and seismological observations [Abercrombie et al., 2003; Banerjee et al., 2007; Hsu et al., 2006; Konca et al., 2007; Pollitz et al., 2008, 2006b], in order to quantify the associated stress changes in the hypocentral region of the 2007 earthquake. The elastic coseismic deformation is calculated in a layered spherical geometry using the direct Greens function method of Pollitz [1996]. We also use this method to model the cumulative elastic deformation from the aseismic afterslip observed after the $2004 - 2005$ earthquake sequence [Banerjee et al., 2007; Chlieh et al., 2007; Hsu et al., 2006]. The elastic structure of the Earth is based on the seismically determined global Earth model PREM [Dziewonski and Anderson, 1981].

Deep-seated transient postseismic relaxation can produce time-dependent deformation and stress changes, exceeding those from the earthquake itself in the intermediate-to-far-field range. The $2004 - 2005$ earthquake sequence produced large stress increases downdip from the coseismic rupture zone, which are expected to drive viscoelastic relaxation of the low-viscosity asthenosphere. A number of studies have examined the viscoelastic relaxation resulting from the 2004 earthquake for the year following the event [Pollitz et al., 2006a, 2008, 2006b], but we extend our model to the time of the 2007 earthquake. Postseismic deformation resulting from the viscoelastic relaxation is calculated on a layered, laterally homogeneous, spherical earth using the method of Pollitz [1992]. This method sums viscoelastic normal modes from earthquake excitation. We employ the oceanic rheology model of Pollitz et al. [2006b] that fits the initial horizontal postseismic velocity, and the GPS time-series, between the 2004 and 2005 events. This model includes a bi-viscous asthenosphere with an initial short-term viscosity of 5×10^{17} Pa s and a long-term viscosity of 1×10^{19} Pa s. We extend the elastic lid to 80 km depth in accordance with the potentially deep, isolated 2007 M_w 8.4 rupture patch [Konca et al., 2008].

The strain field resulting from a coseismic dislocation produces changes in pore-fluid-pressure in the brittle upper crust. The subsequent decay of the excess pore-fluid-pressure gradients will lead to fluid flow and poroelastic deformation. Masterlark et al. [2001] and Masterlark [2003] have previously modeled the effects of poroelastic rebound in a subduction setting and demonstrated that poroelastic effects are generally only significant in the near field directly surrounding the rupture area. We approximate the fully relaxed poroelastic response by subtracting the undrained solution for coseismic deformation from the drained solution for coseismic deformation. Based on the Fialko [2004] study of poroelastic rebound following the 1992 Landers strike-slip earthquake and the Masterlark [2003] study of the 1995 Jalisco-Colima subduction zone earthquake, the crust is assumed to be fluid saturated down

to ∼15 km depth. Ogawa and Heki [2007] propose that the downgoing slab releases fluids into the mantle wedge in sufficiently high quantities, with sufficiently large pore pressure diffusivities, to contribute to the poroelastic rebound during the early postseismic period. Therefore, we test a range of earth models, with undrained Poissons ratio values 0.05 above the drained value for the top 15 km, 30 km, and 60 km of the lithosphere.

2.3.2 Input Source Models

For the coseismic and postseismic deformation calculations, we use previously derived slip distributions based on geodetic and seismological data. For the 2004 Sumatra-Andaman earthquake, we use the GPS-based slip model by Banerjee et al. [2007]. The coseismic slip model includes 15 rupture patches from 0 to 50 km depth with a maximum of ∼19 m of slip. In a few places where sufficient near-field measurements were made following the 2004 earthquake, rapidly decaying deep afterslip can be resolved [Banerjee et al., 2007; Paul et al., 2007]. We consider a simple afterslip model that includes 1 m of slip over the 30- to 50-km depth coseismic rupture patches and over a 50- to 60-km depth extension downdip of the coseismic rupture patches.

For the Nias earthquake, we adapt the slip model from Konca et al. [2007], which is based on continuous GPS (cGPS), seismic, and coral data. We discretize their slip model into 35 segments, ranging from 4 to 59 km depth. The maximum slip is ∼15 m at 27 km depth. In addition, Hsu et al. [2006] and Prawirodirdjo et al. [2010] observed significant afterslip updip and downdip from the main Nias rupture. For modeling purposes, we logarithmically extend the 9-month afterslip distribution from Hsu et al. [2006] to the time of the 2007 earthquake.

Along with the $2004 - 2005$ megathrust sequence, we also consider the smaller 2000 Enggano M_w 8.0 earthquake, which ruptured to the south of the 2007 epicenter. This earthquake is not as well constrained as the later sequence, but is reported to be primarily a left-lateral strike-slip event in the downgoing Australian plate [Abercrombie et al., 2003; Zhou et al., 2002]. Zhou et al. [2002] uses teleseismic body waves to estimate a 95-km-long, 60-km-wide rupture area with an average slip of 11 m. Abercrombie et al. [2003] find that the rupture was com- prised of two subevents. The predominant strike-slip component released ∼65% of the moment and triggered a thrust subevent on the plate-interface (Figure 2.2a). Most of the Enggano aftershocks are located to the southeast of the mainshock and are consistent with the rupture area of the thrust subevent (Figure 2.2b). The aftershock catalog shows a diversity of mechanisms, also consistent with a two-subevent model. Therefore, we use the Abercrombie et al. [2003] solution as our preferred slip model. For the rupture area, we took the average values of the along-strike length ranges given for the two subevents, 75 km and 175 km, respectively. Since there were no aftershocks in the top ∼15 km of the crust, we assume that the downdip extent of the rupture was from the 57-km-deep hypocenter up

to 15 km depth. Given a moment of 1.23×10^{21} Nm, the strike-slip subevent had an average of 4 m of slip, and the thrust subevent had 1 m of slip.

2.3.3 Coulomb Failure Stress-Change Calculations

The deformation calculations are used as input to model the CFS changes along the Sunda megathrust. Previous studies have shown that CFS increases of $100 - 300$ kPa are generally capable of triggering seismicity, and it has been suggested that even tens of kPa are sufficient to advance (or retard) the occurrence of large earthquakes [Lin and Stein, 2004; Rydelek and Sacks, 1999]. Toda et al. [2005] suggested that CFS calculations, in combination with knowledge of the background seismicity rate, could even be used as an earthquake forecasting tool. Due to a lack of knowledge of the total stress field on the Sunda megathrust, and the nonlinear nature of the earthquake triggering process, the use of CFS calculations in forecasting has its limits. However, retrospectively analyzing earthquakes using the CFS method helps to sharpen our limited forecasting skills by better understanding the levels of stress necessary to initiate an earthquake.

We use a CFS function given by $\Delta CFS = \Delta\tau + \mu'\Delta\sigma_n$, which defines ΔCFS as a sum of the change in shear stress τ and the change in normal stress (clamping is negative) σ_n multiplied by an effective coefficient of friction. We assume low frictional fault strength and use an effective coefficient of friction, $\mu' = 0.1$. This is comparable to friction estimates in the studies by Wang et al. [1995] and Wang and He [1999],which found the Cascadia subduction zone to be very weak and to basal detachment frictional strengths inferred from accretionary wedge tapers [Suppe, 2007].

2.3.4 Megathrust Geometry

The previously mentioned coseismic slip distributions all use different geometric parameters for their rupture planes. The CFS changes are resolved onto the Sunda megathrust, and variation in the dip, rake, and strike of the source ruptures and receiver geometry can affect the results. Figure 2.3 shows the receiver fault geometry on which we calculate stress changes. The megathrust geometry follows the strike of the Sunda trench [Curray, 2005]. We choose a downward steepening geometry that represents a compromise between the published megathrust geometries of Subarya et al. [2006] and Chlieh et al. [2008]. These two studies fit a curved megathrust surface based on hypocenter locations and the dip angle indicated by interplate earthquake focal mechanisms. Published source and megathrust fault geometries vary by as much as 25°. The stress calculations are most sensitive to geometrical differences near the downdip and updip ends of the high-slip zones. For example, when comparing CFS changes from the 2004 earthquake resolved on both planar and curved plate geometries, the

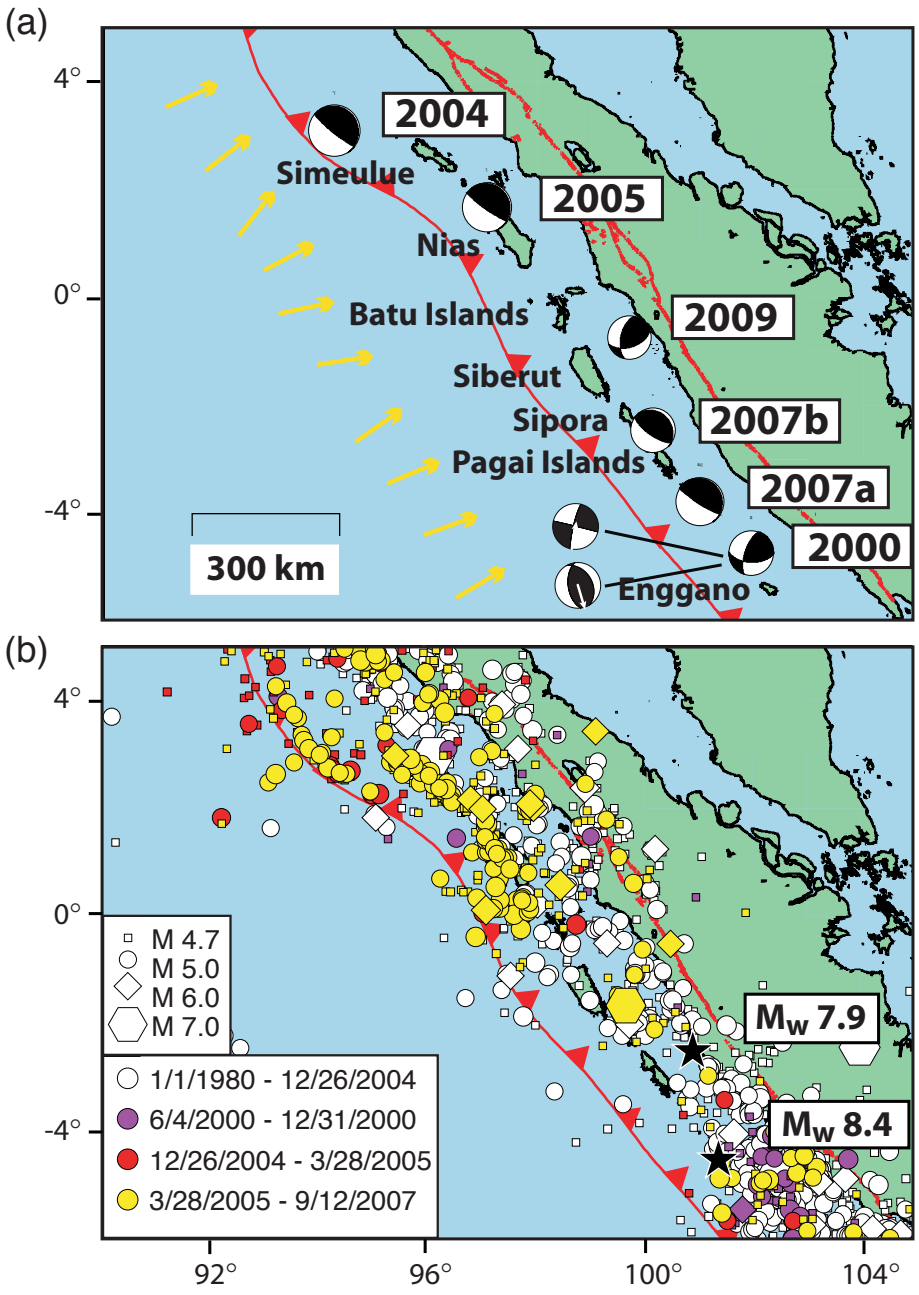

Figure 2.2: (a) Location of Indonesian islands mentioned in the text and focal mechanisms for the recent great earthquakes (Global CMT catalog). The two-subevent focal mechanisms for the 2000 earthquake are also included [Abercrombie et al., 2003]. The slip-vector orientations used in the CFS models are shown with arrows. (b) Earthquake epicenters, sized by magnitude and shaded by time period, for events along the Sunda subduction zone (see text for earthquake catalog description).

Table 2.1: 2004 average coseismic CFS changes under the Sumatran Forearc Islands (kPa)

Megathrust Geometry	Simeulue	Nias	Batu Islands	Siberut
Curved interface	245	22	6	2
10° dip	250	30	5	2
15° dip	220	12	2	< 1
20° dip	205	9	2	< 1

stress-change magnitudes vary by up to a factor of 3 on the subduction thrust below the Sumatran forearc islands due to their proximity to the downdip edge of the 2004 rupture patch (Table 2.1). However, such variations in geometry insubstantially impact the calculated stress-change values on the deeper portions of the megathrust, at depths greater than the source model (Figure 2.4).

Our preferred slip-vector rakes on the receiver fault are based on fault plane parameters for earthquake mechanisms obtained from the Global Centroid Moment Tensor Project (see the Data and Resources section). We filtered the catalog for plate-interface events by restricting the catalog to fault planes with a strike in the range of 280° to 360°, dip in the range of 0° to 35°, and rake in the range of 80° to 130°. This restricted the catalog to 377 events, which we then separated into 1° latitude bins and used their average rake. The rake varies between 95° and 108° (Figure 2.2a).

2.4 Stress Modeling Results

2.4.1 Interseismic Loading Rate

In order to ascertain the relevance of the coseismic and postseismic stresses induced by the megathrust earthquakes, it is important to first calculate the interseismic loading rate. The interseismic loading rate is dependent on the plate convergence rate and the locking depth, which Chlieh et al. [2008] has shown to be considerably heterogeneous along the Sunda megathrust. They use a backslip approach to determine the heterogeneous coupling model that best fits their compilation of paleogeodetic and geodetic data. The coupling on the Sunda megathrust between the Pagai Islands and Enggano is not well constrained, as there are large differences between the forward and inverse models of Chlieh et al. at these latitudes. Their preferred forward model has the megathrust locked between the trench and approximately 40 km depth at the latitude of the 2007 hypocenter, and provides an upper bound on the level of locking for this portion of the megathrust. We determine the static

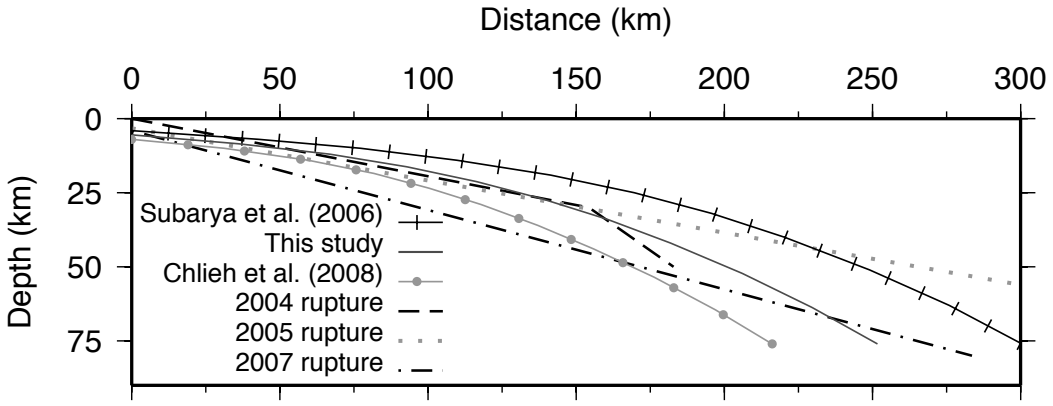

Figure 2.3: Comparison of Sunda plate-interface geometries. The solid line shows our preferred megathrust geometry, intermediate to the geometries used in Subarya et al. [2006] and Chlieh et al. [2008]. The geometry of the southernmost 2004 rupture segment [Banerjee et al., 2007], the 2005 rupture [Konca et al., 2007], and the preferred dip of the two 2007 ruptures [Konca et al., 2008] are also plotted.

stress drop due to the accumulated moment deficit on a rectangular dip-slip fault [Aki, 1966] in order to get an average interseismic loading rate. This interseismic loading rate, of 26 kPa/yr, is an average value for the portion of the plate-interface from the trench to the 40-km locking depth.

We compared this average tectonic loading rate based on the backslip approach with loading due to a buried fault downdip of the 2007 rupture. The buried plate-interface fault starts at the 40-km locking depth and extends to a depth of 600 km. We use a two-segment planar fault model, with the upper segment extending from 40 km to 110 km at a 30° dip and the lower plane extending from 110 km to 600 km at a 40° dip (for representation of interseismic planar fault model, see Figure 2.5a). We impose 4.5 cm/yr of pure reverse slip on the buried faults, based on the long-term convergence rate between the forearc sliver and the Australian plate [Chlieh et al., 2008]. This method leads to a heterogeneous loading of the megathrust, with maximum stresses concentrated at the boundary between the locked and sliding portion of the plate-interface (for cross sections of interseismic changes, see Figure 2.5b,c,d). Based on the buried fault approach, the interseismic loading rate at the hypocentral depth of the 2007 earthquake is 5 kPa/yr.

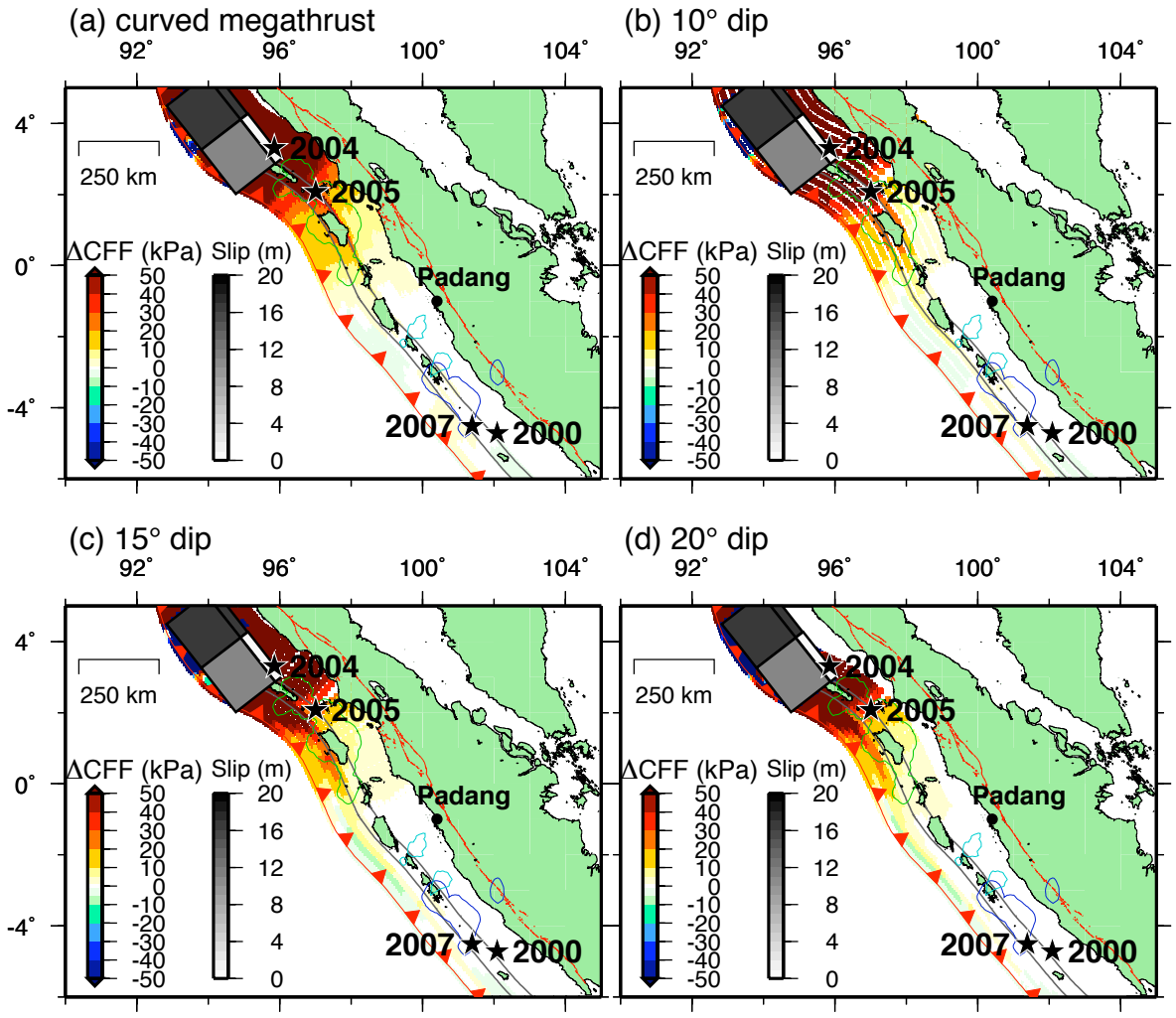

Figure 2.4: The effect of receiver fault geometry. Sumatra coseismic CFS change resolved on (a) preferred curved megathrust, (b) 10° dipping plane, (c) 15° dipping plane, and (d) 20° dipping plane. All of the CFS maps cover the same depth range. The main difference between the varied models is the location of the high stress region that extends past Siberut. This increase in CFS change is due to the increase in elastic stiffness parameters at 15 km and 25 km depth and the downdip edge of the rupture at 30 km depth. The geometrical differences insubstantially impact the CFS change values at the deeper portions of the megathrust, at depths greater than the source model.

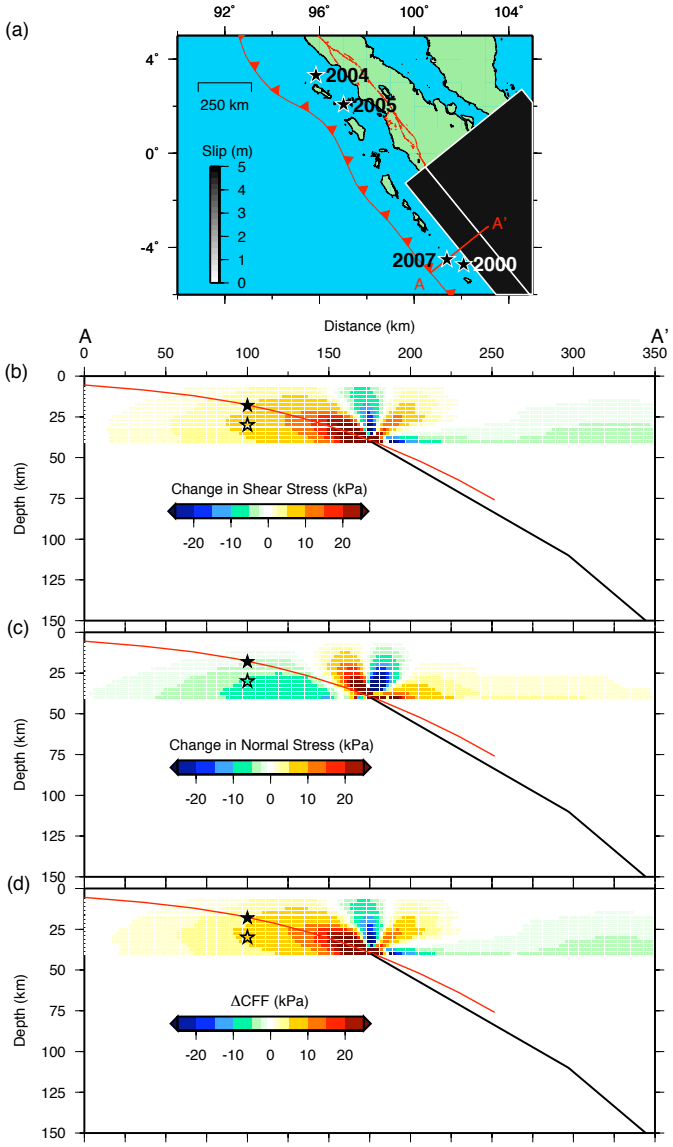

Figure 2.5: Interseismic model for the 2007 hypocentral region. (a) The two-plane interseismic model approximates the geometry of the curved megathrust with plane-1 extending from 40 to 110 km depth at a 30° dip and plane-2 extending from 110 to 600 km depth at a 40° dip. Both planes have a uniform 4.5 cm/yr reverse slip and extend along strike for 800 km. Interseismic annual stressing rates are shown at cross section $A-A'$ for (b) shear stress, (c) normal stress, and (d) CFS with $\mu' = 0.1$. The black planes are the source faults and the red planes are the receiver fault (preferred megathrust geometry). The 2007 hypocenter on our preferred megathrust geometry is shown by a filled star and the USGS hypocenter is shown by an open star. The CFS change is 5 kPa/year at our preferred hypocenter and 6 kPa/year at the USGS hypocenter.

2.4.2 Stress Change from the 2004 Sumatra-Andaman Earthquake

The broad patterns of the modeled CFS change are large stress decreases (i.e., stress drop) over the ruptured region, large stress increases both updip and downdip of the coseismic slip patches, and moderate stress increases past the southern edge of the ruptured region (Figure 2.6a). As shown in previous studies [Gahalaut, 2005; Nalbant et al., 2005; Pollitz et al., 2006a], the future Nias hypocenter was substantially stressed by the 2004 coseismic deformation. The magnitude of the CFS change at the Nias hypocenter is very sensitive to how far south one extends the 2004 slip model and at what depth one calculates the stress. Previously published results have ranged from ∼10 to 100 kPa, and have considered hypocenter depths between 10 to 40 km. When resolving the CFS on the Sunda mega- thrust surface, we find positive stress changes to be focused over the eventual Nias high-slip region (green contours in Figure 2.6a). The 2005 hypocenter is located at 24 km depth using our preferred geometry, with a 49 kPa CFS change. The magnitude of the CFS change varies between 49 to 78 kPa between 24 km depth to the USGS hypocentral depth of 30 km, with an average of 64 kPa CFS change. The coseismic CFS change is particularly high at the 2005 hypocenter because the 2004 source model has a high-slip segment that truncates at 30 km depth. In addition, the elastic properties in the earth model have major increases in stiffness at 15-km and 25-km depth, which causes the CFS change to likewise increase at those depth intervals. However, the positive CFS change decreases rapidly along- strike, and is < 10 kPa before it reaches the 2007 rupture zone. There is no significant CFS decrease over the northern 1797 slip segment to explain why the 2007 earthquake failed to initiate in this region.

Afterslip following the 2004 earthquake increases and expands the coseismic rupture and associated stress changes. Based on a simple afterslip model, with 1 m of slip on planes overlapping and downdip of the coseismic rupture patches, the farthest extent of the > 10 kPa CFS change is the southern edge of Simeulue Island (Figure 2.6b). The CFS change at the 2005 hypocenter is 2 kPa, while the CFS change at the 2007 hypocenter is much less than 1 kPa. It is possible and even likely that small amounts of afterslip closer to the 2005 hypocenter would have produced substantially greater stress changes at this eventual earthquake initiation point. The analysis of geodetic data by Prawirodirdjo et al. [2010] during the year following the 2005 earthquake places up to 8 m of slip updip of the 2004 rupture, between approximately 3.5° N and 6° N. Even with this proposed large amount of afterslip, approaching the amount of slip on the southernmost coseismic rupture segment, the CFS change would still be < 10 kPa over the 2007 rupture zone. More analysis of geodetic data from the time of the 2004 earthquake until the 2007 earthquake is needed to accurately constrain the total aseismic slip following the 2004 earthquake, but it likely did not substantially impact the stress field near the 2007 hypocenter.

The poroelastic effects from the 2004 event are restricted to the shallow portions of the megathrust, updip from the main coseismic slip patch. Figure 2.6c shows that there are no

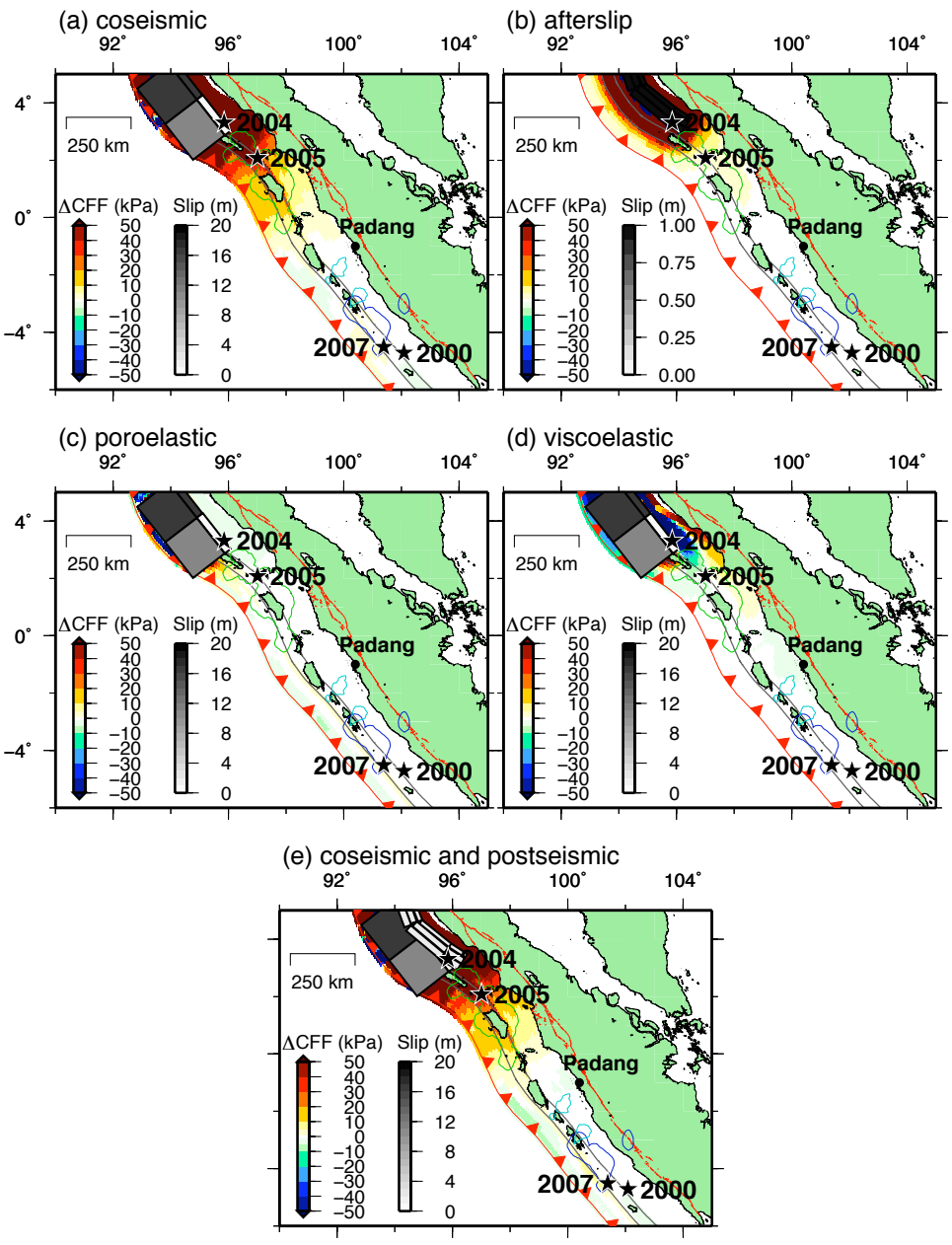

Figure 2.6: Coulomb failure stress changes on the Sunda megathrust resulting from the 2004 (a) coseismic deformation, (b) afterslip deformation from slip on planes at $30-60$ km depth, note the smaller slip scale, (c) poroelastic deformation (with top 15 km of lithosphere fluid-saturated), (d) viscoelastic deformation, (e) total coseismic and postseismic deformation. The earthquake source model overlays the stress changes [Banerjee et al., 2007]. The stress changes are also overlain by the M_w 8.7 2005 5-m slip contour [Konca et al., 2007], the M_w 8.4 2007 1-m slip contour, and the M_w 7.9 2007 1-m slip contour [Konca et al., 2008]. The major increases in elastic moduli, at 15-km and 25-km depth, are marked with gray lines on the megathrust.

large stress changes in the along-strike direction toward the 2007 epicentral region for poroelastic rebound down to 15 km depth. Postseismic poroelastic stress changes from models with variable depths to which fluid flow occurs, ranging from 15 to 60 km, produce CFS changes that are less than 4 kPa everywhere on the 2007 rupture zone.

Viscoelastic relaxation tends to counteract the coseismic stress changes near the rupture patches. Figure 2.6d shows that there are positive CFS changes on the lower half of the coseismic slip segments, at approximately 15 to 40 km depth, and negative CFS changes in the surrounding region. Large positive CFS in the shallow portion of the megathrust only extends as far south as central Simeulue Island.

Although the 2004 earthquake was an M_w 9.2 event, the ∼950 km separation distance prevented the coseismic and postseismic CFS changes at the 2007 hypocenter from being $>$ 10 kPa (Figure 2.6e). As shown in previous subduction zone studies [Goldfinger et al., 2008; Lin and Stein, 2004], this study highlights the fact that megathrust ruptures such as the 2004 Sumatra-Andaman earthquake load the plate-interface updip and downdip of the main rupture and adjacent nearby faults much more than faults further along-strike.

2.4.3 Stress Change from the 2005 Nias Earthquake

The 2005 earthquake was also too far north to produce large coseismic and postseismic CFS changes at the 2007 hypocenter (Figure 2.7d) with total stress changes of $<$ 1 kPa. However, Figure 2.7a shows that the coseismic CFS is $>$ 10 kPa beneath and to the east of Siberut Island, stressing the northern 1797 rupture zone. The CFS change resulting from postseismic afterslip is shown in Figure 2.7b. The CFS $>$ 10 kPa from afterslip extends to the southern edge of the Batu Islands, while substantial CFS increase from viscoelastic relaxation only reaches the northern tip of the islands (Figure 2.7c). If one assumes that only the top 15 km of the lithosphere are saturated with fluids, the poroelastic CFS change of $>$ 10 kPa is restricted to the top ∼10 km of the megathrust down to 0.5° S. If the lithosphere were saturated with fluids down to 30 km depth, then the poroelastic rebound would lead to a negative CFS change below the Batu Islands.

2.4.4 Stress Change from the 2000 Enggano Earthquake

The largest contributor to positive CFS change at the 2007 hypocenter was the M_w 8.0 2000 earthquake (Figure 2.8). The coseismic CFS change at the 2007 hypocenter is 18 kPa, a factor of 3 times larger than the interseismic loading rate at that depth. For the case of only the top 15 km being fluid-saturated, there was only a small contribution of up to ∼1 kPa from poroelastic rebound because the 2000 earthquake rupture occurred below 15 km

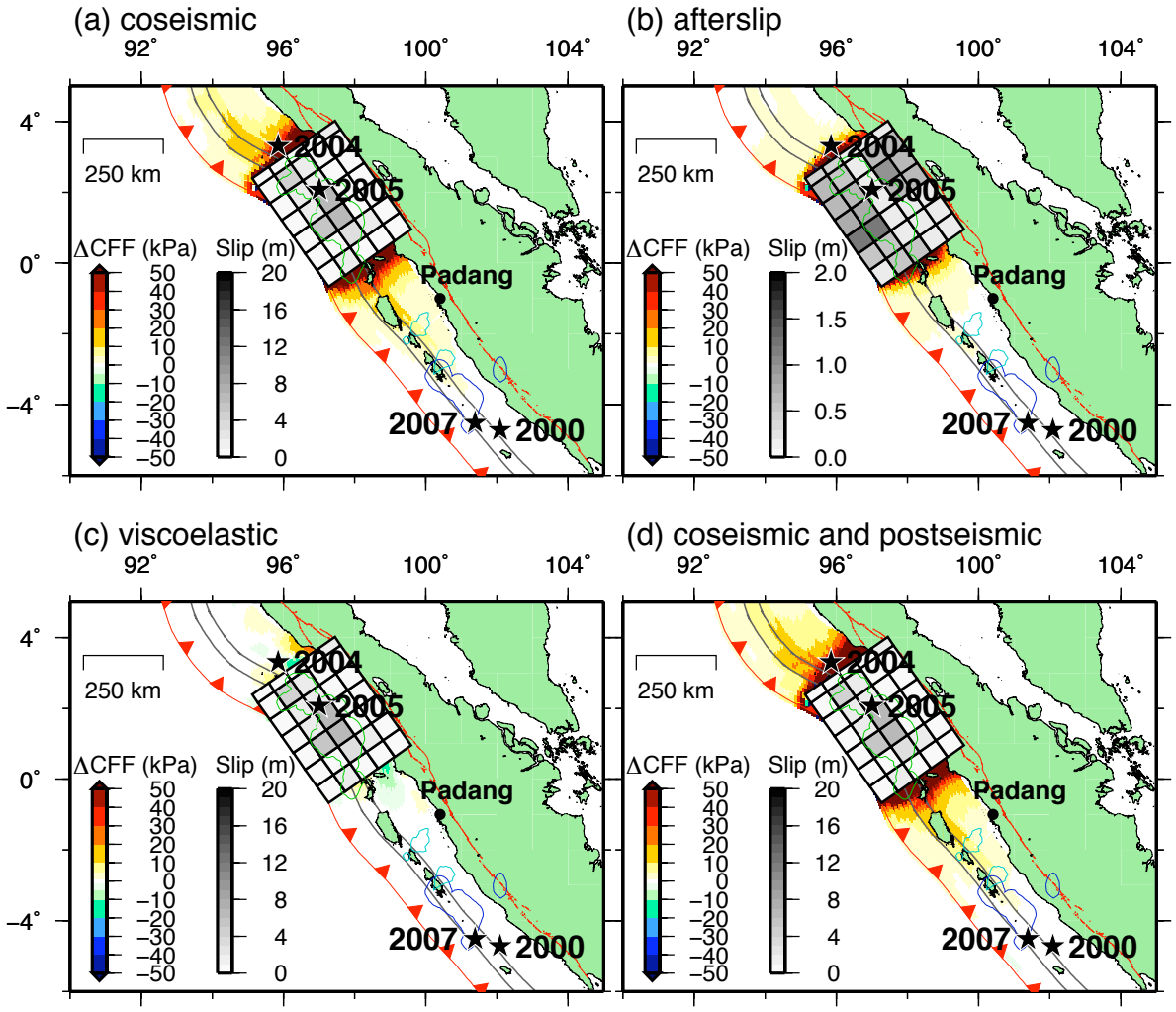

Figure 2.7: Coulomb failure stress changes on the Sunda megathrust resulting from the 2005 (a) coseismic deformation, (b) afterslip deformation, note the smaller slip scale, (c) viscoelastic deformation, (d) total coseismic and postseismic (including poroelastic) deformation. The 2005 earthquake source models [Hsu et al., 2006; Konca et al., 2007] and 2007 slip contours overlay the stress changes [Konca et al., 2008]. The major increases in elastic moduli, at 15-km and 25-km depth, are marked with gray lines on the megathrust.

depth. The models that assumed the lithosphere is fluid-saturated down to 30 km and 60 km depth did increase the range of high CFS changes beyond the 2000 rupture zone, but the 2007 hypocenter is too far away to be sensitive to these changes (for CFS change maps from poroelastic deformation with top 15 km, 30 km, and 60 km of lithosphere fluid-saturated, see Figure 2.9). Seven years of viscoelastic deformation relieved ∼4 kPa of CFS (Figure 2.8b) and brought the total CFS change to ∼16 kPa at the time of the 2007 earthquake (Figure 2.8c). Since the 2000 earthquake epicenter is only ∼80 km southeast of the 2007 epicenter, variations in megathrust geometry can significantly impact the CFS changes in the 2007 hypocentral region. Figure 2.8d, a cross section of coseismic CFS changes on faults parallel to the megathrust from the trench to Sumatra and through the 2007 hypocenter, shows how the stress greatly increases below the megathrust. The coseismic CFS change increases from 18 kPa to 51 kPa, between the location of the 2007 earthquake on our preferred megathrust geometry and the USGS hypocenter. The total response, including coseismic and postseismic stress changes, varies between 16 kPa to 43 kPa.

By comparing the CFS changes at the 2007 hypocenter from the 2000, 2004, and 2005 earthquakes, it is evident that the 2000 event had the largest impact on the stress field. Figure 2.10 displays a time-series of the CFS changes at the 2007 hypocenter due to interseismic loading and the coseismic and postseismic CFS changes from the 2000, 2004, and 2005 earthquakes, relative to the state of stress at the beginning of 2000. The variability between the CFS change calculations at our preferred rupture depth and the USGS hypocenter is strongest for the 2000 coseismic response, but it is also evident in the viscoelastic decay following the 2000 and 2005 earthquakes. There is a larger positive coseismic CFS change at greater depths with an accompanying larger postseismic decay. The total coseismic and postseismic CFS changes from the 2000, 2004, and 2005 earthquakes is approximately equal to the interseismic loading between the 2000 and 2007 earthquakes for the USGS hypocenter, and approximately 1/2 the accumulated interseismic loading for our preferred hypocenter. Thus, although the 2000 earthquake provided the greatest triggering potential out of the three modeled earthquakes, it appears that the 2007 earthquake segment needed the additional loading provided by the seven years of interseismic stress accumulation.

2.5 Seismicity Rate Comparison Method and Data

2.5.1 Seismicity Rate Change Calculation

We investigated seismicity changes following the 2004 earthquake using the standard beta-statistic approach [Hough, 2005; Reasenberg and Simpson, 1992]. Beta is defined as $\beta = (N_a - N_e)/\sqrt{variance}$, where N_a is the number of earthquakes in a given area occurring after a major event and N_e is the expected number of earthquakes based on preevent

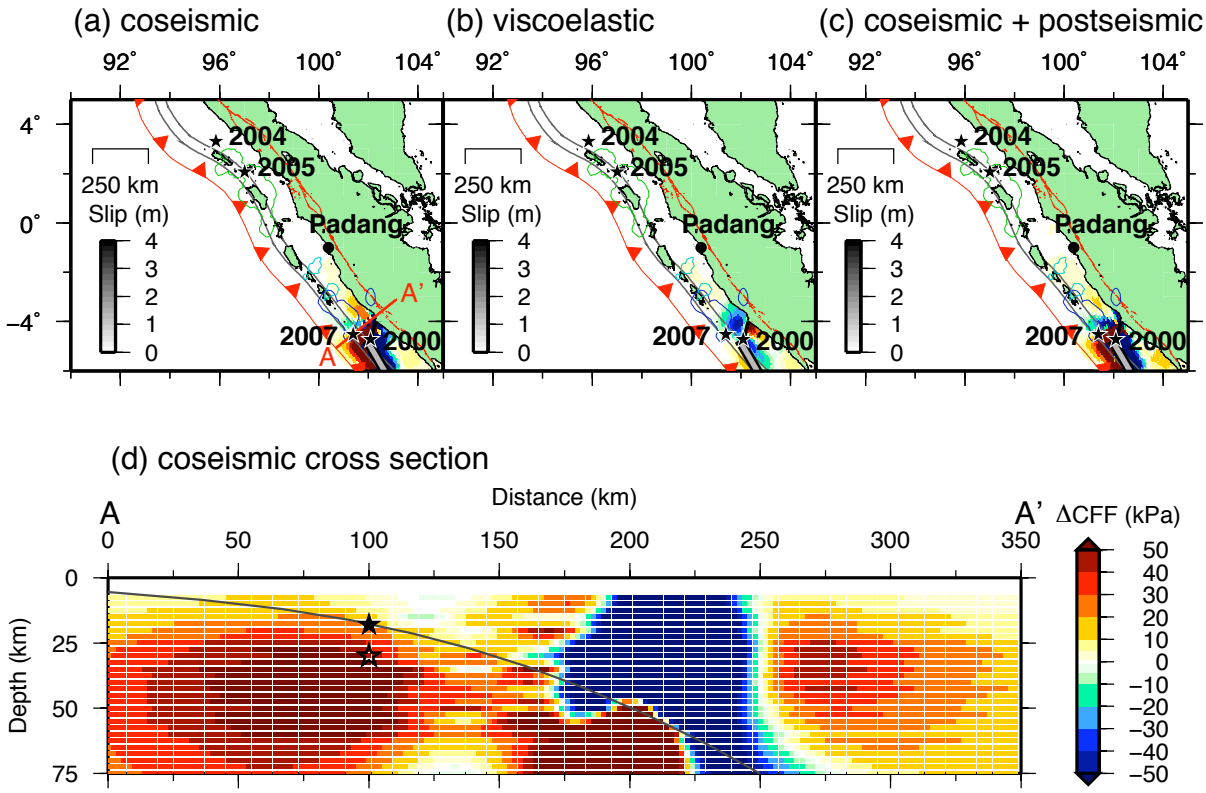

Figure 2.8: Coulomb failure stress changes on the Sunda megathrust resulting from the 2000 (a) coseismic deformation, (b) viscoelastic deformation, (c) total coseismic and postseismic (including poroelastic) deformation. The 2000 earthquake source model [Abercrombie et al., 2003], 2005 slip contour [Konca et al., 2007] and 2007 slip contours [Konca et al., 2008] overlay the stress changes. The major increases in elastic moduli, at 15-km and 25-km depth, are marked with gray lines on the megathrust. (d) Cross section of coseismic CFS changes on megathrust parallel faults. The filled star marks the 2007 hypocenter for our preferred megathrust geometry and the open star marks the USGS hypocenter.

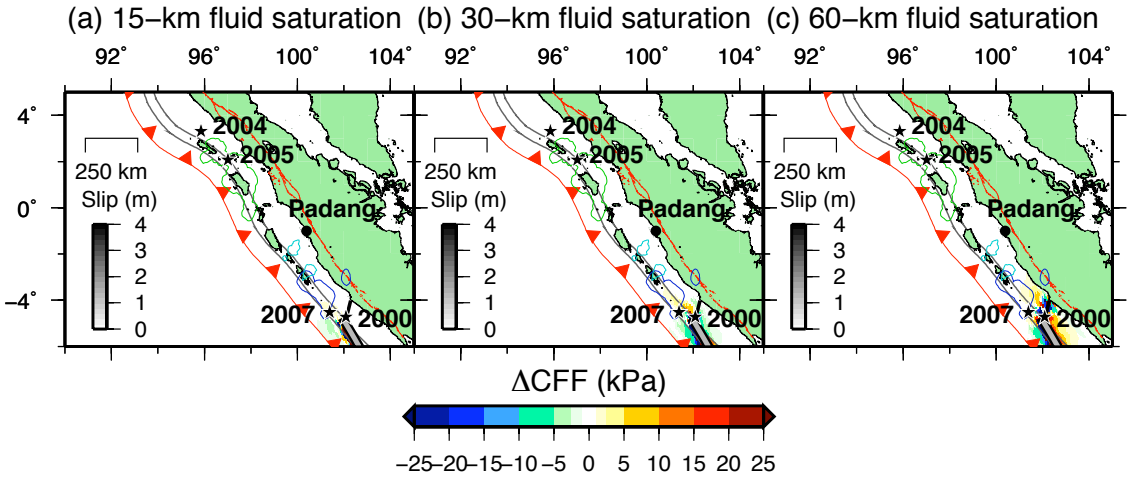

Figure 2.9: 2000 poroelastic CFS change model for (a) pore-fluid saturation down to 15-km depth, (b) pore-fluid saturation down to 30-km depth, and (c) pore-fluid saturation down to 60-km depth. Although the extent of the large poroelastic CFS changes increases with increased pore fluid saturation depth, the 2007 hypocenter is too distant to be sensitive to these changes.

seismicity. Beta will be positive when the postseismic rate is higher than the background seismicity rate and negative when it is lower. We calculated β for 1-yr time intervals in 1° square cells. The preseismic period considered is between 1 January 1980 and 26 December 2004, but we also evaluate seismicity changes using a catalog ending in 1999, prior to the 2000 Enggano earthquake. The postseismic period starts on 26 December 2004, after the Sumatra-Andaman earthquake, and lasts until 12 September 2007.

2.5.2 Earthquake Catalog

Our earthquake catalog consists of the preferred events from IRIS SeismiQuery (`http://www.iris.washington.edu/SeismiQuery/sq?events.htm`, last accessed 12 December 2007), with contributors limited to the International Seismological Center and the National Earthquake Information Service (Figure 2.2b). The magnitude of completeness for the catalog, assuming a power law distribution of earthquakes with magnitude, is 4.7. For this rate comparison study, it is more important to have a larger number of earthquakes in the catalog than more precise locations. Therefore, we chose not to use the Engdahl relocated earthquake catalog [Engdahl et al., 2007] in order to maximize the magnitude of completeness, and thereby the number of earthquakes in the catalog. Our catalog has a similar number of events as the Engdahl catalog at magnitudes greater than 5.0, but is more complete at lower

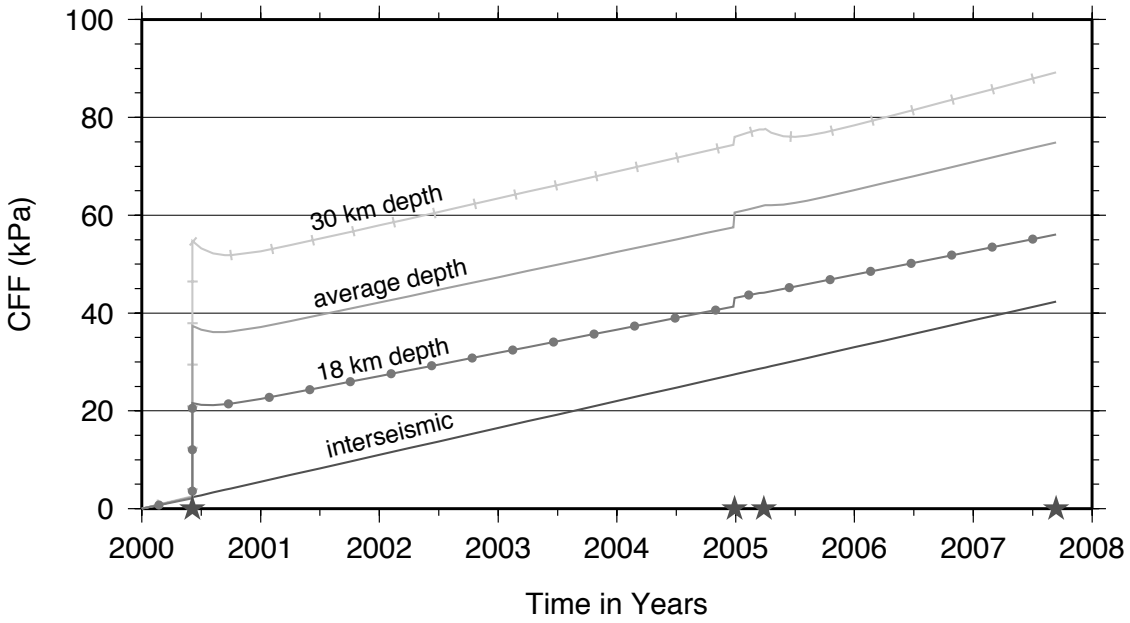

Figure 2.10: The CFS change is plotted for our preferred hypocentral depth on the plate-interface of 18 km, the USGS hypocentral depth of 30 km, and an average of the values between 18 km and 30 km depth. The accumulated CFS change includes coseismic and postseismic stress changes from the 2000, 2004, and 2005 earthquakes along with an interseismic stressing rate. Lacking knowledge of their time-dependence, the poroelastic and afterslip stress changes are added to the coseismic stress changes for the 2000, 2004, and 2005 earthquakes. The interseismic stressing rate is 5 kPa/yr at 18 km depth and 6 kPa/yr at 30 km depth. The average interseismic rate is plotted. The timing of the 2000, 2004, 2005, and 2007 earthquakes is marked with stars.

magnitudes. We used ZMAP [Wiemer, 2001] to decluster the catalog in order to reduce the effect of aftershocks (for a comparison of the full catalog and declustered catalog,see Figure 2.11). The ZMAP declustering program uses Reasenberg [1985] approach.

2.6 Seismicity Rate Comparison Results

In addition to modeling the static stress changes on the Sunda megathrust, we compare the level of seismicity before and after the 2004 earthquake to examine to what degree static and/or dynamic stress changes impacted seismicity rates along the Sunda subduction zone. Dynamic triggering induced by passing seismic waves can have a wider-reaching effect than static stress triggering [Freed, 2005]. Such dynamically triggered aftershocks can in turn trigger more earthquakes, including large ones [Felzer et al., 2002]. Increased levels of seismicity can also be associated with transient aseismic slip, as reflected in the apparent correlation of afterslip and aftershocks following the Nias earthquake [Hsu et al., 2006]. The distribution of the first nine months of Nias afterslip was strongly correlated with positive coseismic CFS changes on the plate interface. This statically triggered aseismic slip may further stress the plate interface, and therefore enable a delay time between the initial earthquake and a triggered event. Similarly, notable far-field seismicity increases could indicate the occurrence of a larger, dynamically triggered slow-slip transient.

2.6.1 Seismicity Rate Changes from 2005 to 2007

Figure 2.12 shows the β values for the years 2005 to 2007 in the Sumatra region, with the year 2004 until the Sumatra-Andaman earthquake also shown for comparison. In general, the seismicity level has been extremely elevated in western Sumatra and the offshore region north of the equator. The downdip width of the high-seismicity zone has narrowed each year since 2005, but seismicity levels still remain an order of magnitude higher in the $2004-2005$ epicentral regions. In 2005, there was a vigorous cluster of aftershocks near Siberut Island, as evidenced by $\beta > 10$. From 2005 to 2007, there was a more moderate increase in seismicity in the region that slipped during the 2007 earthquake sequence, near the Mentawai Islands of Sipora, North Pagai, and South Pagai.

2.6.2 Seismicity in the 2007 Epicentral Region

In 2005, there were moderate seismicity increases of up to $\beta = 4$, in the 1° squares just north and south of the 2007 epicenter (Figure 2.12b). There was a slight decrease in seismicity in the squares containing the 2007 and 2000 epicenters. In 2006, the seismicity increased

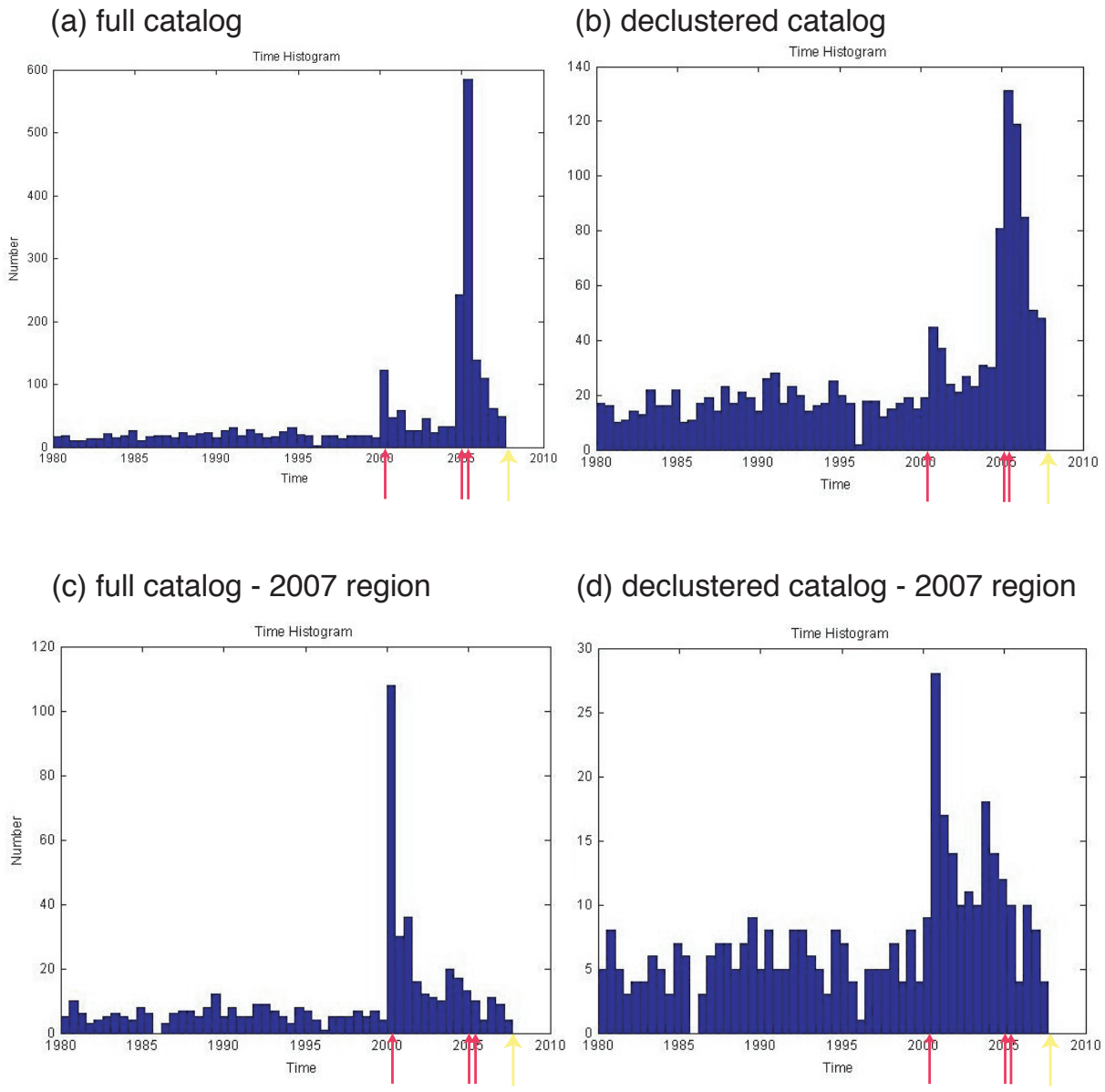

Figure 2.11: $M \geq 4.7$ and depth$<$ 100 km seismicity from (a) full catalog, (b) declustered catalog, (c) catalog restricted to 2007 epicentral region, and (d) declustered catalog restricted to 2007 epicentral region. The red arrows point to the 2000, 2004, and 2005 earthquakes and the yellow arrow points to the 2007 earthquake.

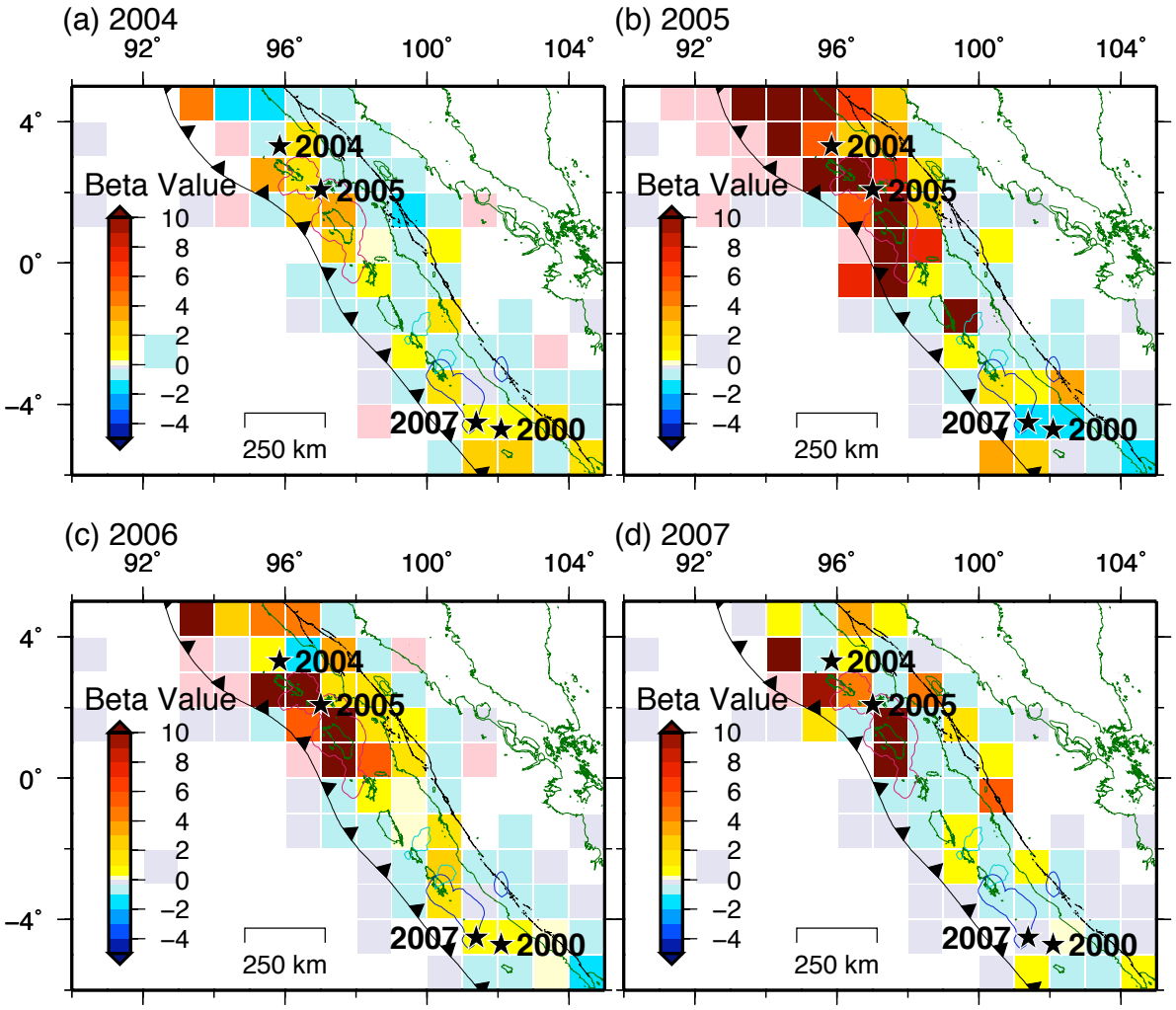

Figure 2.12: For the year: (a) 2004 (compared with 1980 – 2003), (b) 2005, (c) 2006, and (d) 2007 up to the September earthquake. The pink squares signify regions with earthquakes where there were no events during the preseismic period. The 2005 slip contour [Konca et al., 2007] and 2007 slip contours [Konca et al., 2008] overlay the beta values.

to slightly positive in the 2007 and 2000 squares, but decreased in the surrounding region (Figure 2.12c). The β values continued to decrease down to average levels during the first nine months of 2007 before the September earthquake (Figure 2.12d).

When calculating β for the combined nine squares surrounding the 2007 epicenter, longitude $100° - 103°$E and latitude $3° - 6°$S, we see only small fluctuations in the pre-Enggano earthquake seismicity with a mean $\beta = -0.7$ and standard deviation of 0.8 for the years 19801999 (Figure 2.13). The number of earthquakes increased greatly for the time period following the 2000 earthquake with a maximum $\beta \sim 10$; there was a second peak of moderate sized earthquakes from mid-2003 through 2004 (Figure 2.12a, Figure 2.13; for additional β value maps for 2000 to 2003, see Figure 2.14). The seismicity level quickly drops down to within 1-σ of the pre-2000 mean during 2005; however, the β values stay above the pre-2000 mean for 90% of the 2000-2007 time period. Overall, the seismicity levels are appreciably accelerated in the 2007 epicentral region following the 2000 Enggano earthquake with the increased seismicity levels decaying to near average rates by the time of the 2007 Bengkulu earthquake (for β value map using the 1980 to 1999 catalog, see Figure 2.14).

2.7 Discussion

2.7.1 Differentiating Contributions from Different Postseismic Processes

There continues to be some uncertainty about the relative contributions from viscoelastic relaxation, afterslip, and poroelastic rebound to the deformation following the 2004 and 2005 earthquakes. Previous studies have fit the early postseismic geodetic data in the near field as afterslip updip and downdip from the main rupture patches [Gahalaut et al., 2008; Hsu et al., 2006; Paul et al., 2007], whereas viscoelastic deformation is strongly indicated to dominate the far-field time-series [Pollitz et al., 2008, 2006b]. Although all three postseismic processes are almost certain to be occurring during the time span between the 2004 and 2007, none of these mechanisms produce substantial stress changes at the 2007 hypocenter or elsewhere on its rupture zone.

2.7.2 Influence of Fault Friction

For this study, we assumed a weak megathrust with a low effective coefficient of friction, $\mu' = 0.1$. Cattin et al. [2009] analyzed the CFS and seismicity changes on faults adjacent to the Sunda megathrust, after the $2004 - 2005$ earthquake sequence, as a way of estimating the effective coefficient of friction for non-megathrust faults over a broad region from central

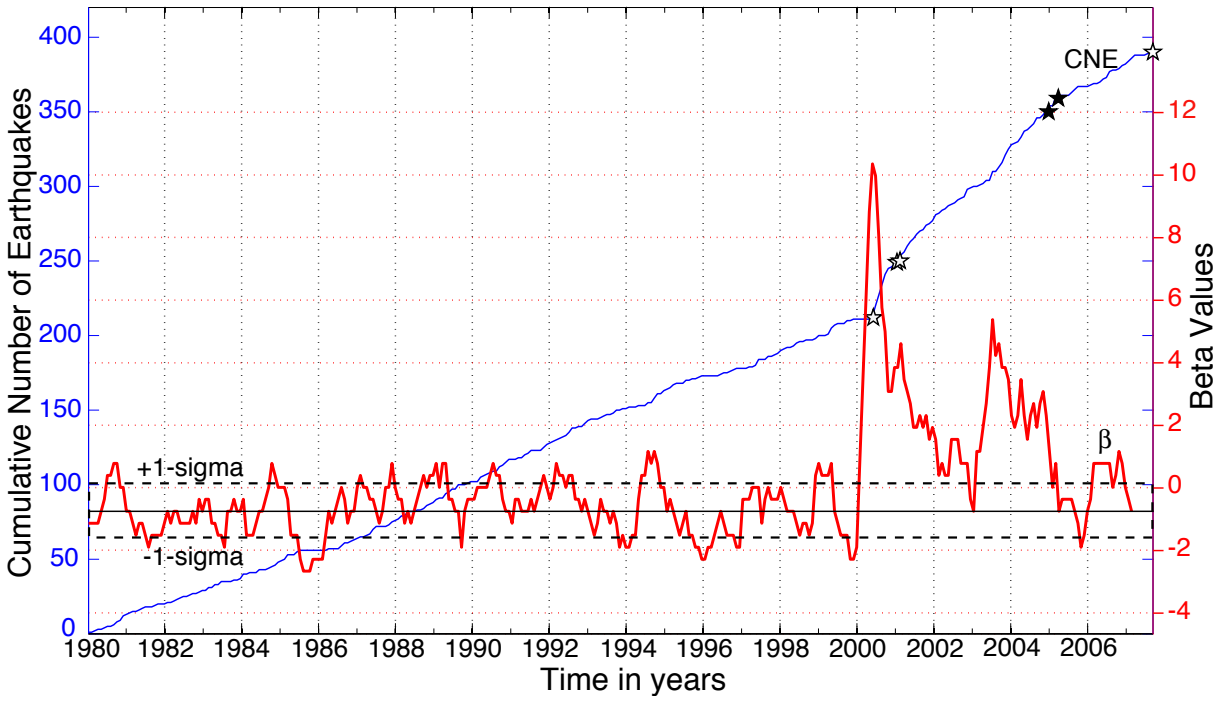

Figure 2.13: Beta values through time in a $3° \times 3°$ area around the 2007 epicentral region are plotted with a thick line. The β value is calculated for 0.5-yr time windows, with 30-day overlapping bins, and uses the declustered $M \geq 4.7$ catalog. In this case, each 0.5-yr interval (N_a) is compared with the entire $1980 - 2007$ catalog (N_e). The cumulative number of earthquakes (CNE) since 1980 is plotted with a gray line. Earthquakes with $M \geq 6.5$ are marked with an open star, and the 2004 and 2005 earthquakes (not in the region) are marked with filled stars. A dashed rectangle encloses the mean ± 1-σ values based on years $1980 - 1999$, before the 2000 Enggano earthquake.

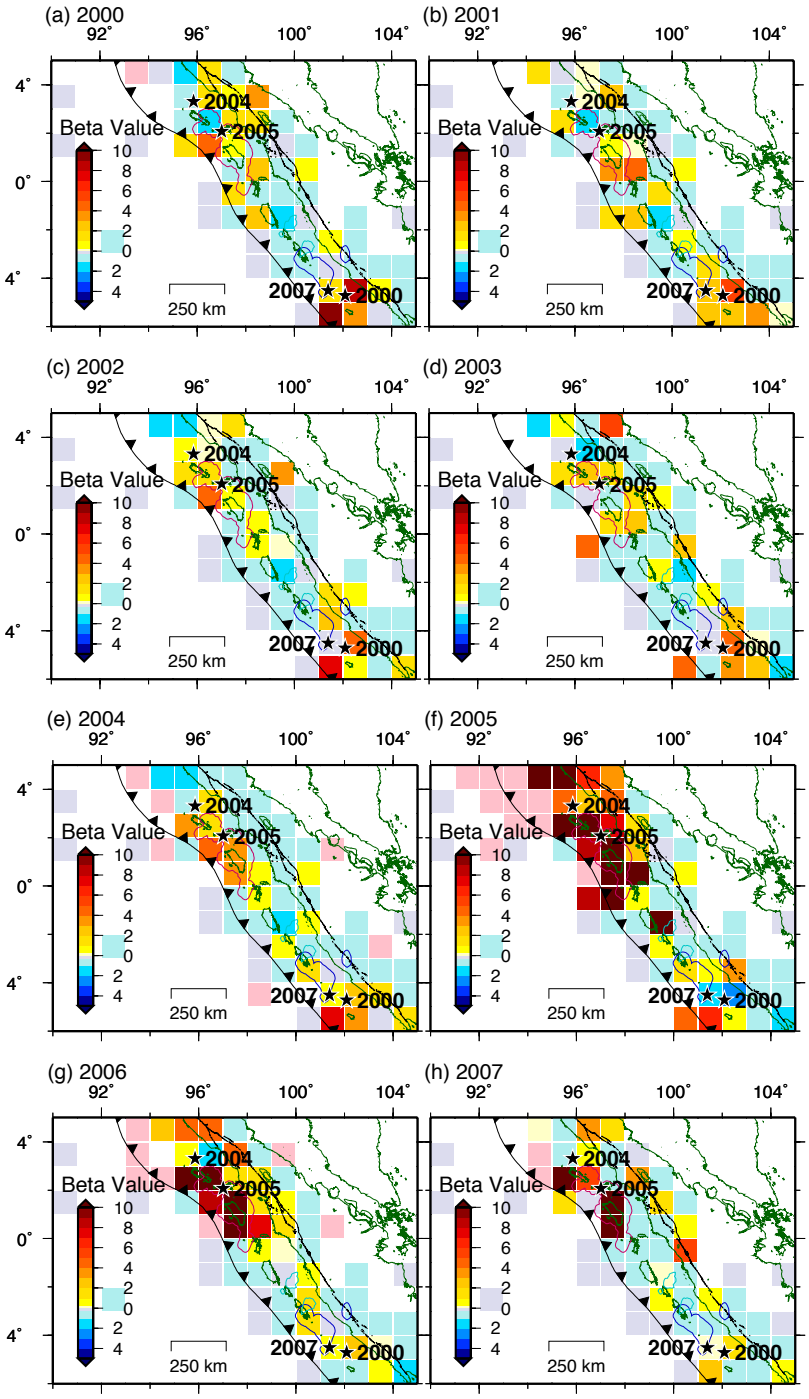

Figure 2.14: For the year: (a) 2000, (b) 2001, (c) 2002, (d) 2003, (e) 2004, (f) 2005, (g) 2006, and (h) 2007 up to the September earthquake.. The pink squares signify regions with aftershocks where there were no earthquakes during the preseismic period. The 2005 slip contour [Konca et al., 2007] and 2007 slip contours [Konca et al., 2008] overlay the β values.

Sumatra to southern Myanmar. Their analysis north of our study area, in the Andaman rift zone, strongly suggests that $\mu' > 0.5$ to explain the triggered seismicity there. They conclude that either the whole region has a high fault friction such as the Andaman rift zone, or there are significant spatial variations in the friction coefficient. Likewise, it is possible that there are variations in the friction coefficient along the megathrust, and we compare our results with models using $\mu' = 0.5$. we find that there are no defining differences in the 2007 hypocentral region due to the coseismic and postseismic CFS changes from the 2000, 2004, and 2005 earthquakes (Figure 2.15c,d), as the large shear stress change overshadows the normal stress change (Figure 2.15a, b). Interseismic creep at depth does impart a negative normal stress change on the shallower portions of the megathrust, therefore a smaller μ' would lead to larger CFS over time (see Figure 2.16 for a stress timeline at the 2007 hypocenter using different values of μ'). Interestingly, when using $\mu' = 0.5$ there is increased CFS change (up to 15 kPa) downdip of the 2007 main rupture patch, near the poorly resolved deep slip patch below the mainland of Sumatra.

2.7.3 The Skipped 1797 Rupture Patch

Again we pose the question, why did the 2007 earthquake rupture the southern portion of the 1833 rupture zone instead of re-rupturing the historic 1797 rupture zone? Natawidjaja et al. [2006] found that the accumulated interseismic slip deficit since 1797 is greater than what was released during the earthquake, while the interseismic slip deficit accumulated over the 1833 segment has reached a maximum of 75% of the 1833 event slip. Total CFS changes since 2004 are positive and > 10 kPa over the Siberut region in the northern half of the 1797 rupture zone. The total CFS changes are > 10 kPa over a larger portion of the historic 1797 rupture segment than they are over the eventual 2007 rupture zone, which has a large positive value only near the hypocentral region (Figure 2.15c).

Although previous studies have suggested that the 1797 earthquake had a smaller magnitude than the 1833 earthquake and has since accumulated a larger interseismic slip deficit, heterogeneities in the regional stress field may account for the southern initiation point of the 2007 earthquake. Slip distributions of the 1797 and 1833 earthquakes are not known in a detailed manner; it could be that in 1833 there was a relatively low-slip area over the future 2007 hypocentral region, and the positive CFS change imparted by the 2000 earthquake was enough to trigger the southern 1833 segment. Heterogeneities in the structure of the incoming oceanic crust may also affect the strength of the megathrust and the interseismic coupling rate and lead to a nonlinear relationship between the region with the largest CFS change and the locations of triggered events. One such crustal complexity is the Investigator Fracture Zone, which enters the Sunda trench in the region between the Batu Islands and Siberut, in the northernmost section of the 1797 rupture zone. This small section of the megathrust is likely poorly coupled [Chlieh et al., 2008] and may explain why the 2005

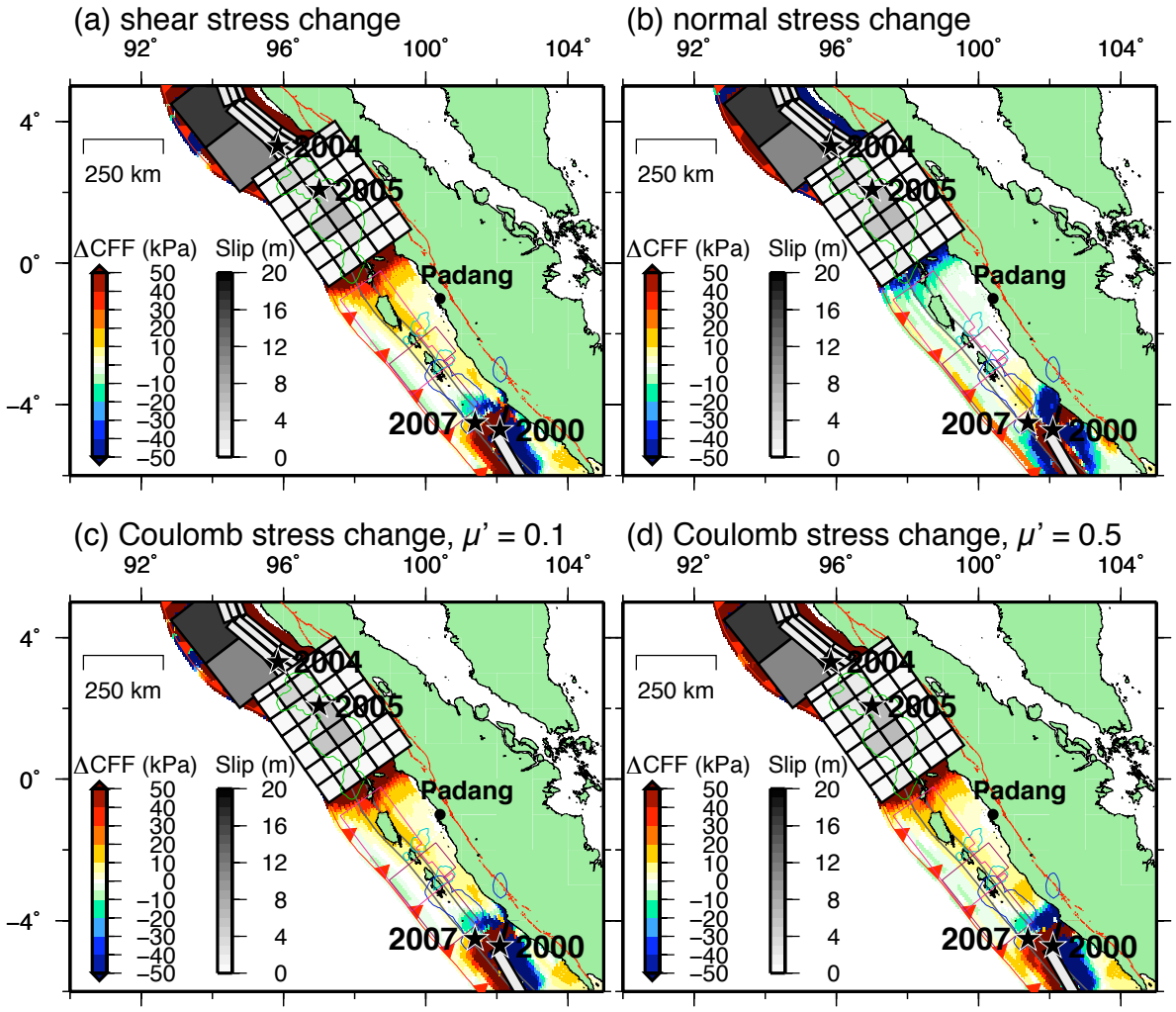

Figure 2.15: Shown are (a) the shear stress component, (b) the normal stress component, (c) CFS with $\mu' = 0.1$, and (d) CFS with $\mu' = 0.5$. The earthquake source models [Abercrombie et al., 2003; Banerjee et al., 2007; Konca et al., 2007], 2005 slip contour [Konca et al., 2007], and 2007 slip contours [Konca et al., 2008] overlay the stress changes. The 1797 and 1833 slip patches are also outlined [Natawidjaja et al., 2006]. The major increases in elastic moduli, at 15-km and 25-km depth, are marked with gray lines on the megathrust.

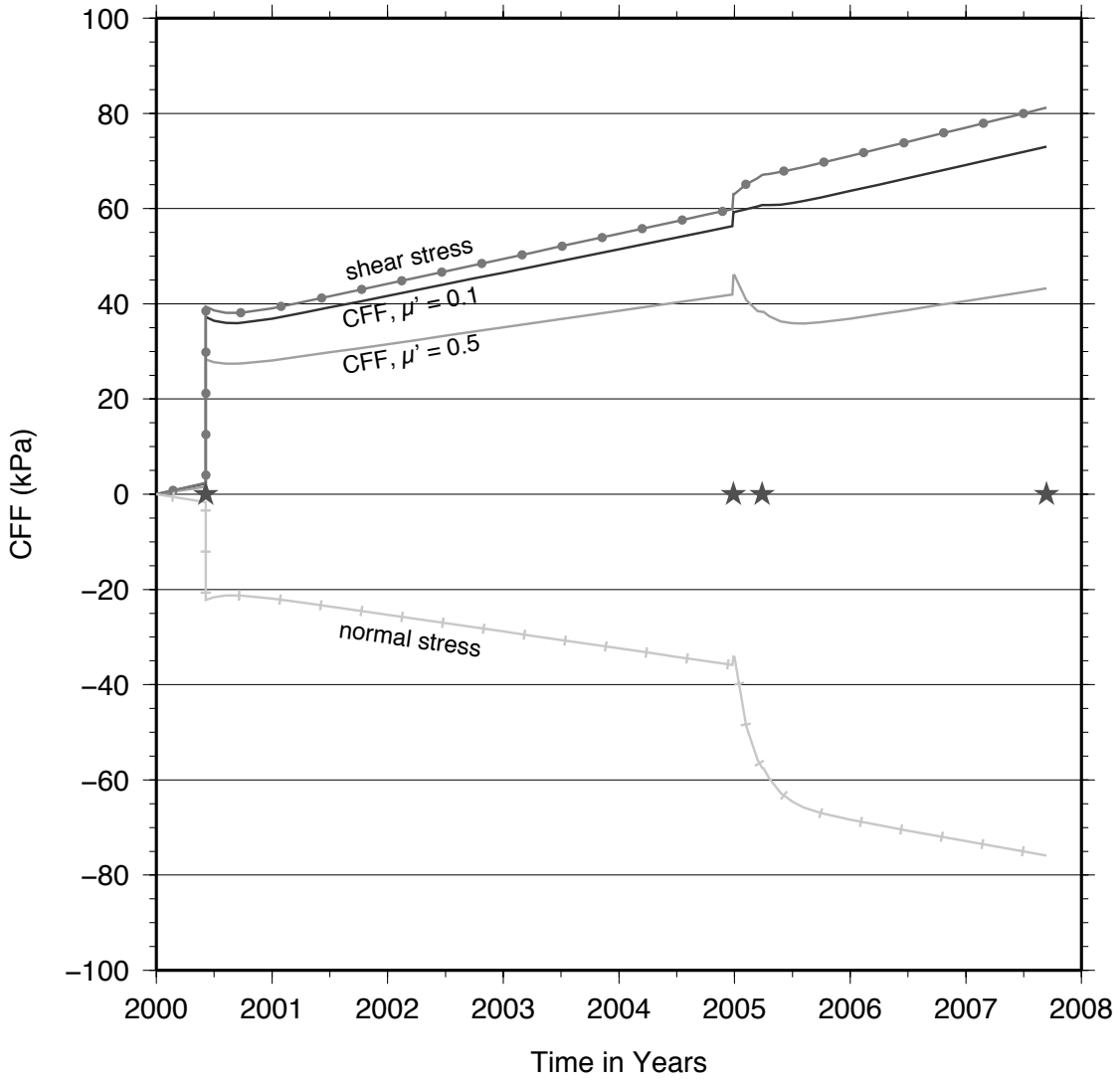

Figure 2.16: The normal stress change, shear stress change, and CFS change ($\mu' = 0.1$ and 0.5) is plotted at the average hypocentral depth (between our 18 km depth and the USGS 30 km depth). The accumulated CFS change includes coseismic and postseismic stress changes from the 2000, 2004, and 2005 earthquakes along with an interseismic stressing rate. Lacking knowledge of their time-dependence, the poroelastic and afterslip stress changes are added to the coseismic stress changes for the 2000, 2004, and 2005 earthquakes. The timing of the 2000, 2004, 2005, and 2007 earthquakes are marked with stars.

earthquake did not trigger a large earthquake in this nearest, highly stressed portion of the Sunda megathrust. Nonetheless, the section just south of this poorly coupled segment, the Siberut segment, is strongly coupled, has not ruptured since 1797, has $\Delta CFS > 10$ kPa from the 2005 earthquake, must be close to failure, and represents a substantial remaining earthquake and tsunami hazard in the region.

However, the total normal stress changes are negative (clamping) over the 1797 rupture zone and positive over the 2007 rupture zone (Figure 2.15b). This may indicate that the relatively small normal stress changes have a greater impact on triggered seismicity than is assumed by Coulomb failure theory. Similarly, Perfettini et al. [1999] observed an association between the peak slip locations from the 1989 Loma Prieta earthquake and portions of the fault that had been unclamped by the preceding Lake Elsman events. They suggest that the unclamping could have indirectly triggered the Loma Prieta earthquake by triggering aseismic creep. The periphery of the creep zone would sustain high shear stress increases, with the Loma Prieta hypocenter being located in this high stress region. Similarly, the 2000 earthquake unclamped the deeper half of the future 2007 rupture zone, which could have induced aseismic creep. A combination of coseismic CFS increases at the 2007 hypocenter from the 2000 earthquake and aseismic creep induced shear stress increases may explain why the southern 1833 segment ruptured before the 1797 segment.

2.7.4 Delayed Dynamic Long-Distance Triggering

It is also possible that seismic waves could trigger aseismic slip episodes at large distances, and these slow-slip events can further stress the plate-interface and trigger additional earthquakes. One such far-field triggering example is the tremor triggered by teleseismic earthquakes in Cascadia, and the possible correlation between large teleseismic events and episodic tremor and slip episodes [Rubinstein et al., 2009]. Similarly, the 1992 Landers, California, earthquake was initiated by a swarm of foreshocks that appears to represent a slow-slip transient triggered by the preceding Joshua Tree earthquake [Dodge et al., 1996]. The observed increase in seismicity levels over the two eventual 2007 rupture zones during 2005 and 2006 (Figure 2.12b,c), along with the increase in seismicity during the few years following the 2000 earthquake (Figure 2.14a,b,c), may be evidence of such a delayed triggering mechanism. The increased level of moderate sized earthquakes could have promoted (or be a reflection of) aseismic creep over the portion of the 2007 rupture zone that was unclamped by the previous stress changes (Figure 2.15b). Unfortunately, there is a lack of geodetic data during the two years following the 2000 earthquake; however, a comparison of GPS velocities for the years $1992-1994$ and $2002-2007$ at Enggano suggests a change in coupling of the plate-interface at this region south of the 2000 hypocenter [Prawirodirdjo et al., 2010]. Future analysis of the cGPS data spanning the time between the 2004 and 2007 earthquakes may be able to confirm whether there indeed was transient aseismic slip on this southern portion of the

Sunda megathrust leading up to the two 2007 earthquakes.

2.8 Conclusions

Coulomb failure stress change at the 2007 M_w 8.4 hypocenter, resulting from the combined $2004-2005$ coseismic and postseismic deformation, is likely too small to have triggered the recent earthquake. There are also no large negative CFS changes in the Siberut region from the combined 2004-2005 coseismic and postseismic deformations that could help explain the delayed recurrence of the 1797 earthquake. However, the normal stress change was negative over the Siberut region and positive over the 2007 segment; this unclamping of the 2007 segment may have promoted an aseismic slip event and eventual rupture. The smaller 2000 Enggano earthquake turns out to have had the largest CFS change at the 2007 hypocenter and may help to explain its southern location. Investigations of seismicity rate changes across the region, for the years following the 2004 earthquake, show that there was increased seismic activity along the two 2007 rupture zones and overall higher levels of seismicity since the 2000 earthquake. Geodetic investigations are necessary to determine whether this increased level of seismicity was associated with accelerated aseismic slip on the Sunda megathrust, a potential contributing factor to the timing and location of the 2007 earthquake. Unfortunately, the earthquake and tsunami hazard still remains high for the Siberut region that last slipped in 1797.

Chapter 3

Another Potential Source of Destructive Earthquakes and Tsunami Offshore of Sumatra

3.1 Abstract

We link geodetic data from the Sumatran GPS Array (SuGAr) and earthquake focal mechanisms to show that a 900-km long backthrust, arising from the Sunda megathrust offshore of Sumatra, has recently become active following the series of great megathrust earthquakes of this past decade. Shallow failure of the Mentawai backthrust explains coseismic displacements during moderate earthquake clusters in 2005 and 2009. These two clusters represent the first activity on the backthrust in more than 30 years. Existing paleogeodetic evidence of vertical deformation in past centuries is too sparse to characterize earlier major activity, but leaves open the possibility of historic great magnitude 8+ backthrust earthquakes. Geodetic evidence for rupture of the Mentawai backthrust during the two recent earthquake clusters suggests that this large fault may well pose an additional seismic and tsunami hazard to the coastal communities of central Sumatra.

3.2 Introduction

Since 2004, three great earthquakes have focused considerable attention on the Sumatran section of the Sunda megathrust [Briggs et al., 2006; Chlieh et al., 2007; Konca et al., 2008, 2007]. Another long fault, the Mentawai fault, runs parallel to the Sunda megathrust from about 1° to 7°S (Figure 3.1, inset), and for decades its sense of motion was misinterpreted as strike-slip [Diament et al., 1992; Sieh and Natawidjaja, 2000]. Very recent high-resolution seismic reflection and bathymetric data have shown that it is principally a trenchward-dipping reverse fault system [Singh et al., 2010]. Singh et al. [2010] highlight several steeply-dipping recent seismic events that may be located on the Mentawai backthrust. We analyze SuGAr geodetic data and earthquake focal mechanisms to confirm that the backthrust is indeed active and has produced two M_w 6.7 earthquakes. We also discuss

sparse, existing paleogeodetic data that bear on whether it has generated very large earthquakes and tsunamis within the past several millennia.

3.3 Cluster Seismic Activity

Recent, detectable seismic activity on the Mentawai fault started with the 2005 earthquake sequence, which originated just east of the strait that separates Siberut and Sipora islands (Figure 3.1). The seismic activity started gradually within a week of the great 2005 Nias earthquake. The largest (M_w 6.7) earthquake occurred on the 10th of April and was followed within the next seven hours by M_w 6.5 and 6.1 events. Between the 2nd and 17th of April the cluster included twenty-eight M 5+ earthquakes, whose cumulative seismic moment equals a M_w 6.9 earthquake. The arrival of a tsunami up to a meter high on the southeastern coast of Siberut implies a nearby shallow source for the M_w 6.7 earthquake.

Global centroid moment tensor (GCMT) focal mechanism solutions and centroid locations (www.globalcmt.org) of the 2005 cluster are consistent with slip on the Mentawai backthrust (Table 3.1). The dips of all trench-parallel nodal planes between the 7th and 17th of April are > 40. These steep dips and the shallow (12 to 29-km) centroid depth range, signify that these earthquakes were likely not produced by slip on the megathrust (Figure 3.1, cross-section). Instead, it appears that the earthquakes originated on a relatively steep NE- or SW-dipping fault within the accretionary prism. The 2005 cluster is the first occurrence of such shallow, steeply dipping earthquakes near this recently mapped portion of the Mentawai backthrust system since the beginning of the GCMT catalog in 1976 (Figure 3.2.)

The second cluster began on 16 August 2009 with a M_w 6.7 earthquake just east of Siberut. The 2009 cluster overlaps with but is predominantly northwest of the 2005 cluster. It was a less energetic sequence. Only one M 6+ earthquake and nine M 5+ earthquakes (combined moment magnitude of M_w 6.7) occurred from the 16th to 23rd of August. The focal mechanisms and shallow depths of the 2009 earthquakes (12 to 19-km) are also consistent with slip on the SW-dipping Mentawai backthrust (Figure 3.1, cross-section).

The global centroid moment tensors (GCMT) focal mechanisms of the 2005 cluster signify that there is structural complexity in this region. They divide into two groups with the northern group 1 represented by the M_w 6.7 earthquake and the southern group 2 represented by the M_w 6.5 earthquake (Figure 3.1 and Table 3.1). The 2005 cluster earthquakes are located near the bend in the frontal backthrust (FBT) fault trace, and the observed focal mechanism complexity could signify that there are structural differences at depth north and south of the bend. The group 1 events have a larger average strike of 145°, similar to the 2009 cluster events average of 153° and to the 151° strike of the northern FBT fault trace.

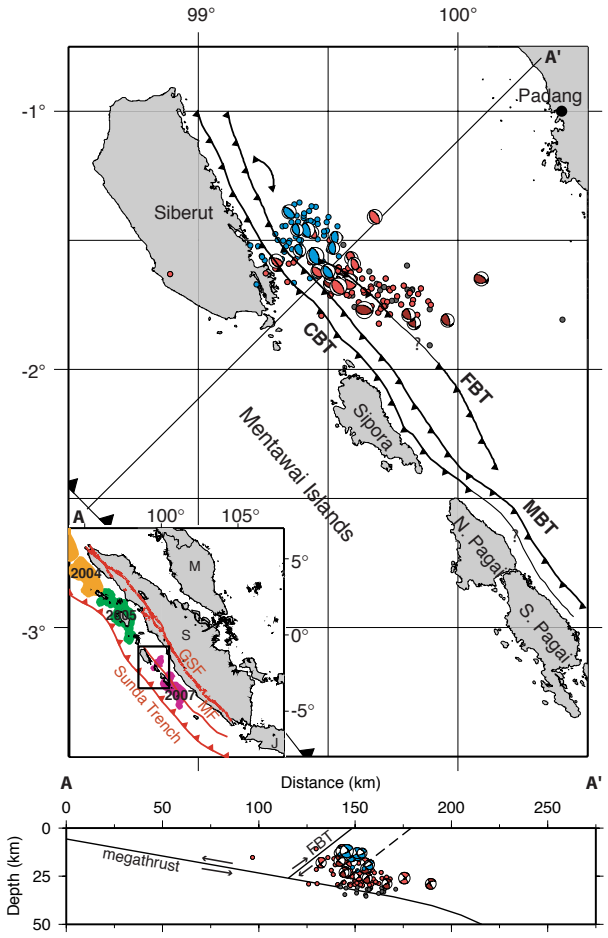

Figure 3.1: Two recent earthquake clusters near the Mentawai fault. The 2005 group-1 and group-2 focal mechanisms are light and dark red, respectively, and the 2009 focal mechanisms are red and blue, respectively. Double-difference relocated earthquakes [Pesicek et al., 2010] from the start of the 2005 cluster until one month following its largest earthquake, above and below 30 km, appear as red and dark gray circles, respectively. EHB earthquake locations from the first month following the 2009 M_w 6.7 earthquake are blue [E. R. Engdahl unpublished data, method from Engdahl et al.,2007]. GCMT focal mechanisms from both clusters are plotted at their centroid locations. Backthrust fault traces are from Singh et al. [2010]: frontal backthrust (FBT), main backthrust (MBT), and coastal backthrust (CBT). (Inset) Recent great earthquake ruptures of the Sunda megathrust [Briggs et al., 2006; Chlieh et al., 2007; Konca et al., 2008]. M, S, and J are Malaysia, Sumatra, and Java. GSF and MF are the Great Sumatran fault and the entire extent of the Mentawai fault. (Cross-section) Relocated earthquakes with reviewed and accepted depths and focal mechanism from the two recent clusters are projected onto the NE-oriented section with megathrust geometry from Hayes and Wald [2009]. The frontal backthrust is projected to the plate interface. The dashed backthrust is fitted to the 2005 and 2009 relocated earthquakes shallower than 30 km depth.

The group 2 events have a lower average strike equal to 100°, with an even larger eastward component than the 132° strike of the southern FBT fault trace. In addition, the group 2 events are significantly left-lateral oblique with an average rake of 53°.

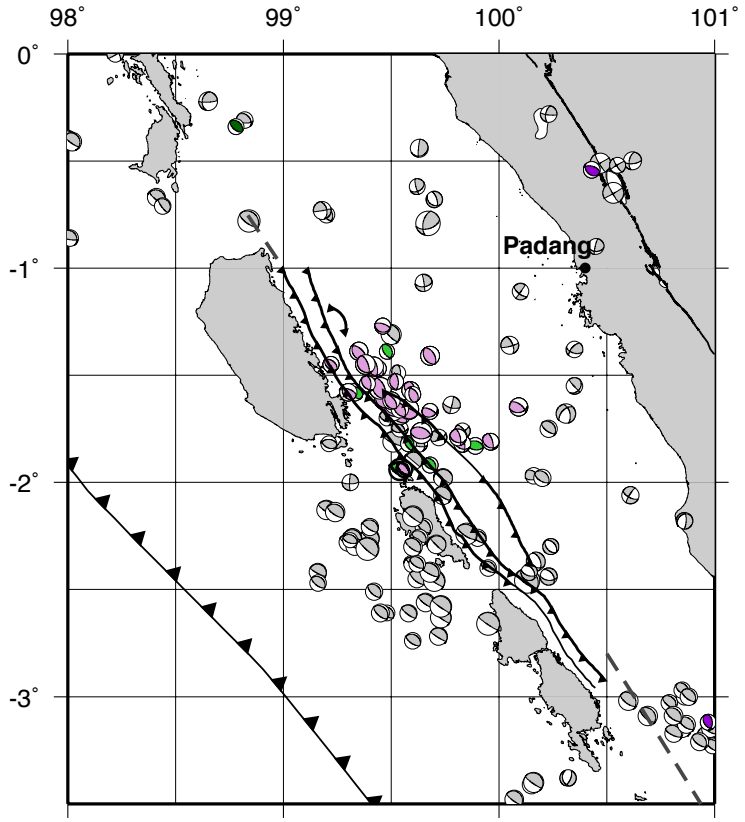

Figure 3.2: All earthquakes in the GCMT catalog from 1976 - June 2010 are shown in light gray. Earthquakes with depth ≤35 km, with nodal plane striking approximately parallel to the Sunda trench and dipping ≥30° before 2005 are shown in dark green, and post-2005 are shown in light green. Earthquakes with depth ≤35 km, with nodal plane striking approximately parallel to the Sunda trench and dipping ≥40° before 2005 are shown in dark purple, and post-2005 are shown in light purple. The two earthquakes north of Sipora, which were triggered by the 2007 M_w 7.9 aftershock, are bolding outlined in black. The Mentawai fault beyond the Singh et al. [2010] mapped backthrust structures is shown in gray.

Table 3.1: Cluster focal mechanisms[1]

Cluster	Date	Moment (Nm)	Depth (km)	Strike	Dip	Rake
2005	02-04-2005[2]	2.255e16	12	348	33	105
2005 Group 1	07-04-2005	1.089e17	18	149	39	123
2005	10-04-2005	1.329e19	12	142	34	89
2005	10-04-2005	0.743e18	26	147	38	88
2005	10-04-2005	0.981e17	21	135	48	61
2005	10-04-2005	1.929e18	17	135	10	107
2005	10-04-2005	2.509e16	25	150	42	92
2005	12-04-2005	2.516e16	18	172	50	110
2005	12-04-2005	0.811e17	13	133	31	95
2005	17-04-2005	1.592e17	23	142	45	86
Group1 Avg.			19	145	37	95
2005 Group2	10-04-2005	6.746e18	15	90	44	73
2005	10-04-2005	2.976e17	17	105	48	82
2005	10-04-2005	2.169e17	29	83	40	53
2005	10-04-2005	4.341e16	23	88	41	43
2005	12-04-2005	5.823e16	21	112	38	39
2005	12-04-2005	7.167e16	26	106	38	36
2005	13-04-2005	6.830e16	29	118	29	47
Group2 Avg.			23	100	40	53
2005 Avg.			21	125	38	77
2009	16-08-2009	1.219e19	12	161	31	92
2009	16-08-2009	6.433e17	14	159	26	86
2009	16-08-2009	2.653e16	15	143	35	65
2009	16-08-2009	3.780e16	19	158	30	69
2009	18-08-2009	2.878e16	12	136	43	58
2009	19-08-2009	2.603e17	13	147	31	103
2009	19-08-2009	3.473e16	13	170	28	84
2009	23-08-2009	1.571e17	12	153	32	99
2009 Avg.			14	153	32	82

3.4 GPS Measurements

Several continuously operating SuGAr stations recorded surface motions associated with the 2005 and 2009 clusters (locations on Figure 3.3). The GAMIT/GLOBK software package [Herring, 2005; King and Bock, 2005] was used to solve for station coordinates, on a daily basis. In addition to the 15 second GPS data from the SuGAr permanent stations, data from nine IGS sites [Dow et al., 2009] surrounding Sumatra were also added in the primary processing stage. The IGS (International GNSS Service) sites used are: COCO, CUSV, DARW, DGAR, IISC, KUNM, PERT, PALK, PIMO. Precise satellite orbits, earth orientation parameters and tightly constrained positions of the IGS sites in a self-consistent reference frame were used to produce daily solutions which include GPS station positions, satellite orbits, earth orientation parameters, and tropospheric delays. The loosely constrained, ambiguity-fixed daily solutions were combined with ambiguity-free quasi-solutions of more than 250 globally distributed IGS sites. The local and IGS daily solutions were combined to estimate positions of each site. Finally, globally distributed IGS core sites were used to define ITRF2005 reference frame with a residual RMS of 3-4 mm.

The position time series from the three stations that detected the 2005 cluster appear on Figure 3.3. The largest recorded offset occurred at NGNG on the 10th of April (day 100), the day of the three M 6+ earthquakes. The northeastward motion and subsidence of NGNG indicates that slip on a NE-dipping fault is not a plausible cause for the cluster. The motions of MSAI and PSKI are small, implying that the source is closer to NGNG.

The position time series for the three GPS sites closest to the 2009 cluster shows that the largest offset appears on the 16th of August (day 228), the day of the M_w 6.7 earthquake (Figure 3.3b). The horizontal motion at NGNG and TLLU is northeastward, whereas MSAI moves to the southeast. The more northerly motion of NGNG in 2009 demonstrates that the 2009 source is north of the 2005 source. Moreover, subsidence of all of Siberut sites implies a shallow source east of the island.

3.5 Deformation Modeling

We model both clusters using the principal component analysis-based inversion method (PCAIM) developed by Kositsky and Avouac [2010]. This method uses the Greens functions for a dislocation in an elastic homogeneous half-space [Okada, 1985]. Clusters of seismicity can be associated with slow slip, which may produce more deformation than is expected by summing the magnitude of all of the events in the cluster. PCAIM allows epoch-by-epoch inversion and enables us to model the time series for the most active period of the clusters. Thus, one can ascertain if the slip was restricted mainly to the days of the M_w 6.7 earth-

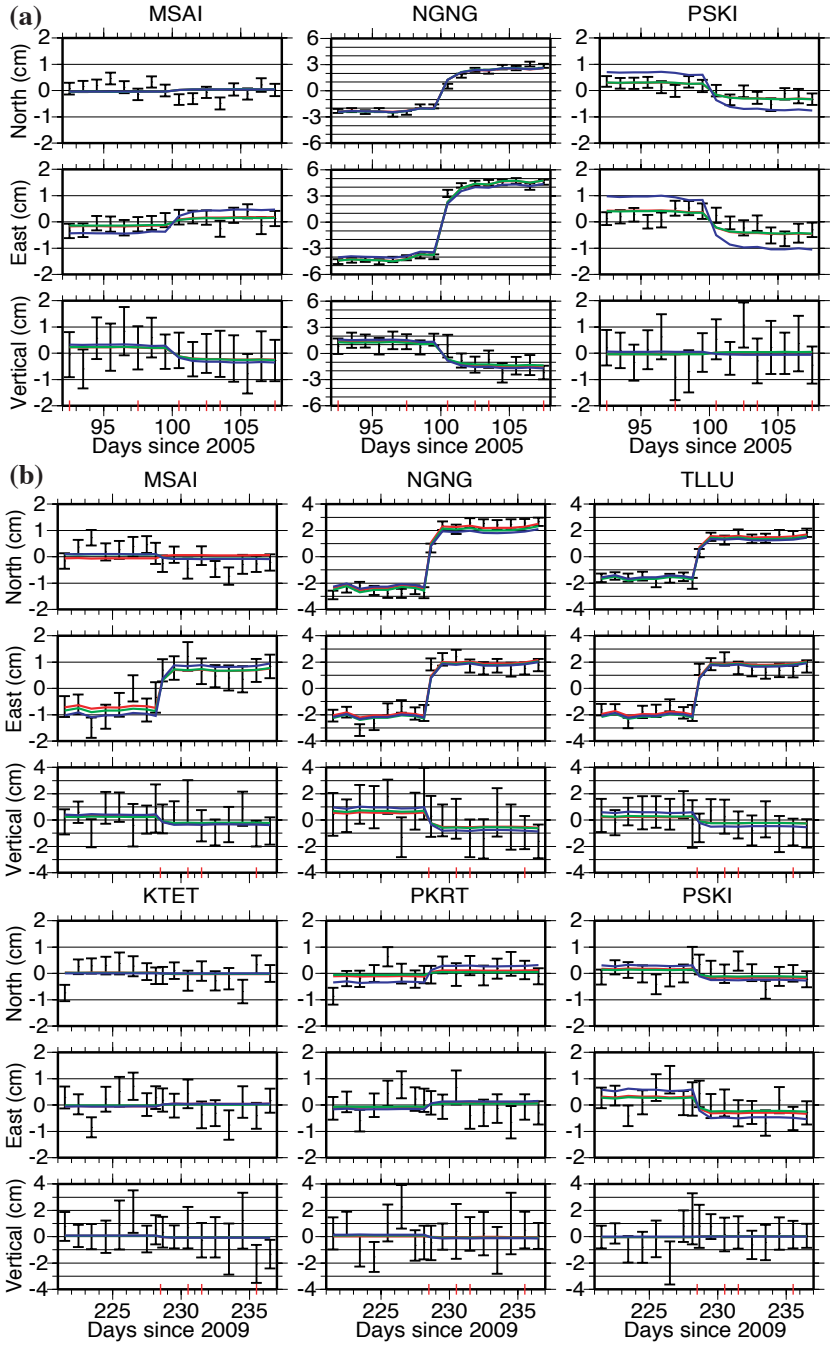

Figure 3.3: Horizontal and vertical position time series with one-sigma uncertainty bars for the (a) 2005 cluster and (b) 2009 cluster. Superimposed are the predictions from the two-segment model (green curves), the one-segment model (red curves), and the eastern model (blue curves). The red vertical bars signify days with earthquakes large enough to have a GCMT solution.

quakes or if there was considerable slow slip.

For simplicity we assume that slip on the FBT fault, the mapped backthrust trace closest to the earthquake clusters, caused all observed motion. The horizontal spread of the earthquakes and the offset between the relocated earthquake hypocenters, consisting of teleseismic double-difference relocations for the 2005 cluster [Pesicek et al., 2010] and EHB relocations for the 2009 cluster [E. R. Engdahl unpublished data, using methods from Engdahl et al., 2007], and the FBT in the Figure 3.1 cross-section may be due to uncertainties and possible bias in the reported earthquake locations. The earthquake location uncertainties are ∼15 km for EHB epicenters and ∼10 km for depths [Engdahl et al., 2007]. For the region southwest of the island of Simeulue, Tilmann et al. [2010] found that CMT centroids have a southwestward bias and EHB locations have a northeastward bias relative to the aftershock locations determined using a temporary seismic array. The teleseismically determined earthquake locations in the Mentawai backthrust region may also suffer from this systematic location bias due to strong local velocity heterogeneities. Alternatively, the earthquake locations east of the FBT may indicate rupture of an unmapped, outward-propagating, blind thrust fault, and we explore this option later.

We invert for distributed slip on a two-segment fault grid, consisting of 5-km square slip patches, to seek the optimal location of peak coseismic slip. We adjust the Laplacian smoothing parameter to allow for the smoothest distribution of slip while fitting the data within uncertainties and ensuring that the majority of the slip was located in a focused patch. The two-segment fault model changes strike at a prominent bend in the FBT (Figure 3.4 and Table 3.2) and extends from the surface to ∼25 km, the depth of the underlying megathrust. The dip and rake values are based on the backthrust focal mechanisms.

Figure 3.4a displays the 2005 cumulative slip model. The main locus of slip is centered at 9 km depth and is consistent with the epicentral location of the 2005 earthquakes, but is 10 km shallower than the average centroid depth for the 2005 cluster. Figure 3.4b shows the 2009 cumulative slip model. The 2009 high-slip region is distinctly northwest of the 2005 patch. Maximum modeled slip in 2009 extends from the surface to ∼8 km, shallower than the modeled 2005 rupture and consistent with the shallower centroid depths for the 2009 earthquakes. The similarity between the geodetically derived cumulative magnitudes, M_w 6.9 in 2005 and M_w 6.7 in 2009, and those derived from summing the seismic moments (also M_w 6.9 and 6.7) implies that nearly all the detectable deformation occurred during the recorded earthquakes.

We compare the two-segment fault model with a simpler one-segment model that uses the average strike of the FBT nearest the clusters (Figures 3.3, 3.4, and Table 3.2). Both modeled faults extend from the surface to ∼25 km, the depth of the underlying megathrust [Hayes and Wald, 2009], with dip and rake values based on the backthrust focal mechanisms.

Table 3.2: Backthrust model fault geometries
Latitude and longitude coordinates of the fault corner located at the surface, in the strike direction

Model	Corner	Length (km)	Width(km)	Strike	Dip	Rake
1-segment	-1.99, 99.93	110	45	139	35	80
2-segment North	-1.58, 99.47	45	45	151	32	82
2-segment South	-2.00,99.94	75	40	132	38	77

The only significant improvement of the two-segment over the one-segment model is a better fit to the southward motion of MSAI in 2009.

We also explore modeling slip on a backthrust that is located further to the east of the FBT to better fit the relocated earthquake locations [Pesicek et al. [2010]; E. R. Engdahl unpublished data using methods from Engdahl et al. [2007]]. We propagate the original two-segment model 33 km NE along the strike of profile A-A from Figure 3.1 (Figure 3.4c). This eastern fault geometry fits the average location of the 2005 and 2009 relocated earthquakes shallower than 30 km depth, assuming the same average dips used in the original two-segment model. We also extend the backthrust to ∼30 km depth in order to continue to project to the megathrust interface.

Both the 2005 and 2009 slip models using this eastern fault have deeper, more focused slip patterns. They also both have increased magnitudes of slip and consequently higher total moment magnitudes of M_w 7.3 and M_w 7.1 for the 2005 and 2009 clusters, respectively. The eastern 2005 model does not fit the site PSKI within the 95% confidence ellipse. The southwestern motion at PSKI is too large due to the increased deep slip on the updated eastern fault geometry. The eastern 2009 model still fits the GPS data within the 95% confidence ellipses.

Overall, the two-segment model that follows the strike of the mapped FBT fault trace is the favored fault geometry. The eastern two-segment model does not fit the 2005 GPS data as well as the FBT model and the deeper slip location does not correlate with the 2005 tsunami account, which implies a shallow rupture.

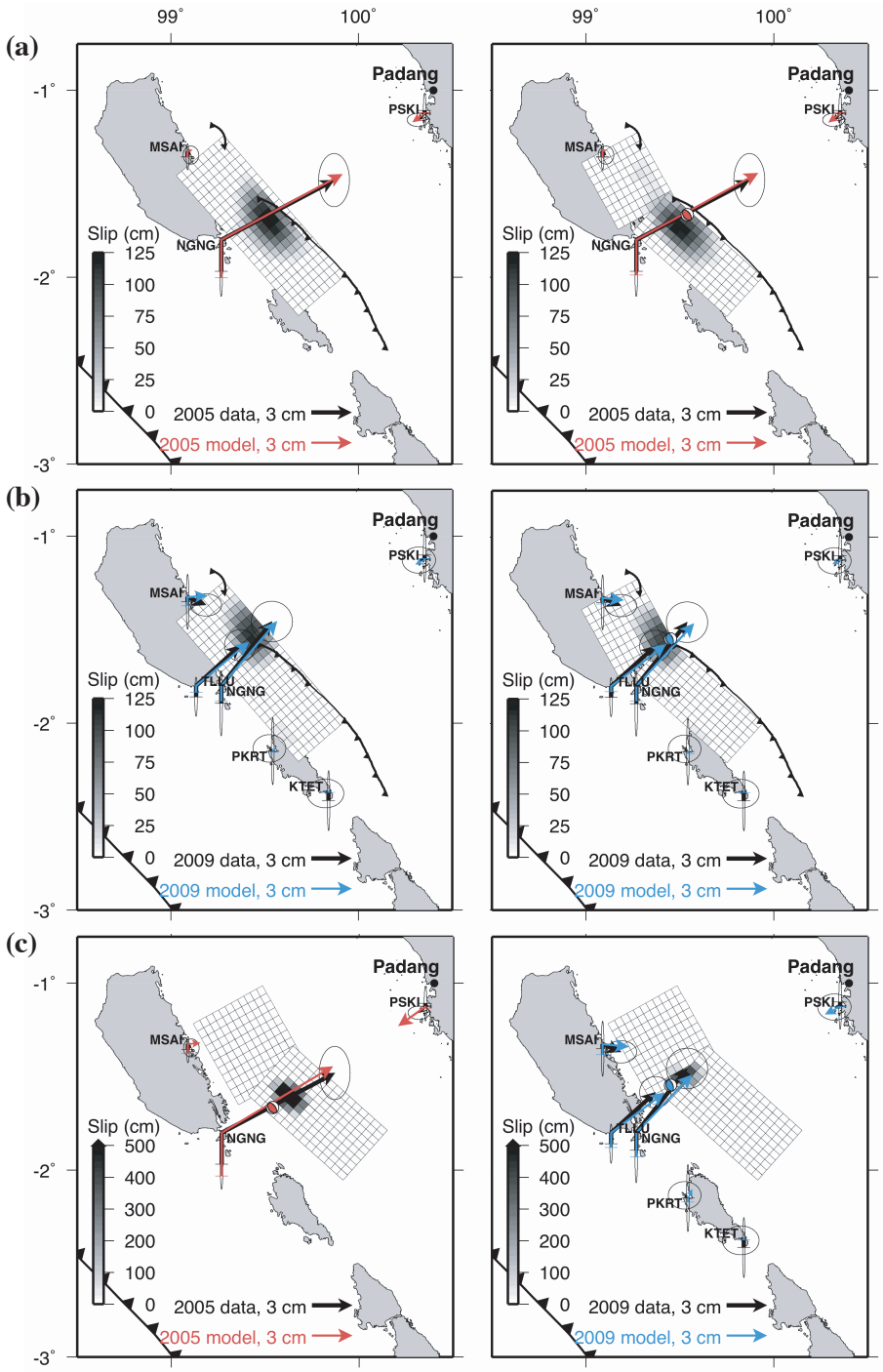

Figure 3.4: Average displacements (black arrows tipped with 95% confidence ellipses) compared with predictions (colored arrows) from the (a) 1-segment and 2-segment cumulative slip models for 2005 Cluster (b) 1-segment and 2-segment cumulative slip models for 2009 Cluster (c) the two-segment slip model shifted 33 km NE for the 2005 cluster and the 2009 cluster. Gray shading within the grids shows surface projection of the fault slip.

3.6 Megathrust-Backthrust Stress Interaction

To understand whether this recent resurgence of activity on the Mentawai backthrust could have been triggered by the past decade's series of megathrust earthquakes, we explore the stressing relation between the Sunda megathrust and the Mentawai backthrust. It is especially important to understand how the Sunda megathrust affects the backthrust system because it lies over the Siberut segment, the largest remaining portion of the megathrust without a modern great rupture. In general, megathrust ruptures relieve shear stress on the overlying section of the backthrust while increasing the shear stress on sections further along strike. Moreover, megathrust ruptures unclamp the shallow portion of the backthrust and further lock the deeper portion of the backthrust.

We model the coseismic deformation associated with the recent megathrust earthquakes of 2005 and 2007 in order to quantify the associated stress changes on the Mentawai backthrust system, in the vicinity of the 2005 and 2009 clusters. We use a CFS function given by $\Delta CFS = \Delta\tau + \mu'\Delta\sigma_n$, which defines ΔCFS as a sum of the change in shear stress τ and the change in normal stress (clamping is negative) σ_n multiplied by an effective coefficient of friction, $\mu' = 0.4$. For the input coseismic source models, we use previously derived slip distributions based on geodetic and seismological data [Konca et al., 2008, 2007]. We model the static stress changes at six different depths along the dipping FBT (Figure 3.5) using the methods described in Chapter 2.

Static Coulomb failure stress (CFS) change values at the 2005 cluster location resulting from the 2005 Nias earthquake are positive, but are likely too small to explain the renewed activity. Thus, the short time interval between the two events suggests a dynamic stressing process triggered the cluster activity.

The closer 2007 megathrust earthquakes stressed the section of the Mentawai fault between Siberut and Sipora more than the 2005 Nias earthquake. The largest 2007 aftershock, a M_w 7.9 event, produced the greatest stress changes in the cluster region out of all the recent megathrust earthquakes. It increased CFS on the deeper portion of the backthrust northwest of Sipora, and indeed steeply dipping M_w 6.5 and M_w 5.0 thrust ruptures occurred there three hours and 3 days following the megathrust earthquake (Figure 3.5). In addition, the 2007 aftershock created a significant stress shadow over the 2005 cluster region and mildly enhanced stress within the future 2009 cluster region. Thus we suggest that the 2007 aftershock triggered two 2007 backthrust earthquakes and encouraged the cluster activity to migrate further northwest in 2009.

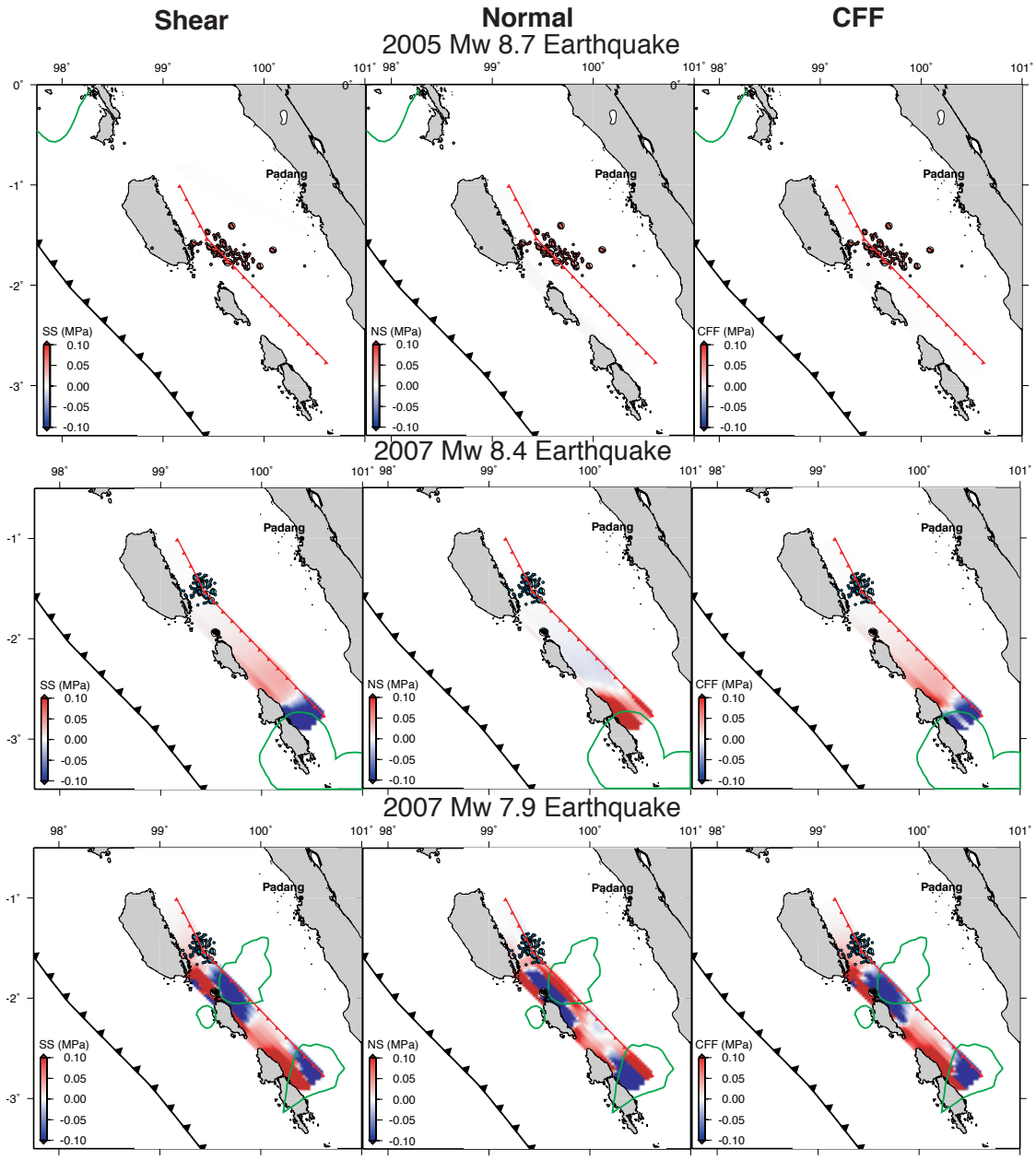

Figure 3.5: Modeled stress changes from the recent, nearby megathrust earthquakes resolved on the FBT (surface trace shown in red). The high slip contour lines from the modeled megathrust earthquakes are shown in green [Konca et al., 2008, 2007]. The CFS models assume $\mu' = 0.4$. The 2005 cluster events are plotted red, the two 2007 steep thrust events are black, and the 2009 cluster events are blue.

3.7 Discussion

We have shown that at least a portion of the Mentawai backthrust, above the Sunda megathrust is active. It produced two adjacent clusters of shallow, moderate earthquakes in 2005 and 2009, with the 2005 M_w 6.7 earthquake producing a moderate tsunami. These relatively small events raise several important scientific questions that also have humanitarian implications.

Is the Mentawai backthrust active along its entire 900-km length? If so, does it commonly rupture in short sections, as in 2005 and 2009, or is it capable of producing much larger earthquakes? Does it sometimes slip concurrently with the megathrust, analogous to a 200-km-long backthrust that is now suspected to have failed simultaneously with the Sunda megathrust in 2004, north of Simeulue [Chauhan et al., 2009; Plafker et al., 2006; Singh et al., 2011b]. All these questions point to one big question: Is the Mentawai backthrust another plausible source for very large, destructive earthquakes and tsunami along the coast of Sumatra?

Currently, the only evidence bearing on these questions is sparse paleogeodetic data from the coral reefs of the Mentawai Islands. Although the islands subsided very slightly during the shallow 2005 and 2009 ruptures, elastic dislocation modeling shows that large Mentawai backthrust events, with concurrent slip along deeper parts of the backthrust, would produce uplift of the islands (Figure 3.6a). Moreover, such ruptures should produce southwestward tilt of the islands, toward the Indian Ocean, in contrast to northeastward tilt during great megathrust events (see representative model for 1797 megathrust event in Figure 3.6d).

Most of the sudden uplift events recorded by island corals over the past 700 years exhibit landward tilt and are thus consistent with slip on the Sunda megathrust [Sieh et al., 2008]. However, during the late 17th century, the microatolls allow that Sipora and North Pagai could have tilted toward the Sunda trench [Sieh et al., 2008]. The uplifts recorded in the microatolls for the large ∼1685 uplift event range as high as 0.8 m. The lack of uplift recorded at a site on South Pagai limits the southern extent of this hypothetical backthrust rupture to about 130 km south of the 2005 backthrust rupture. We model the observed uplift pattern on the MBT, with 2.3 meters of uniform slip from the plate interface boundary up to the surface (Figure 3.6c). This hypothetical backthrust event would equal a moment magnitude M_w 7.9 event.

Another scenario to consider is a coincident megathrust-backthrust event. There is no evidence of significant slip on the Mentawai backthrust, either in the coral uplift pattern or in the coseismic GPS data, for 2007 M_w 8.4 rupture [Konca et al., 2008]. However, the vertical GPS data for the 2007 M_w 7.9 earthquake does show southwestward tilting of the Mentawai islands due to the unusual deeper location of the megathrust slip, east of the islands. We

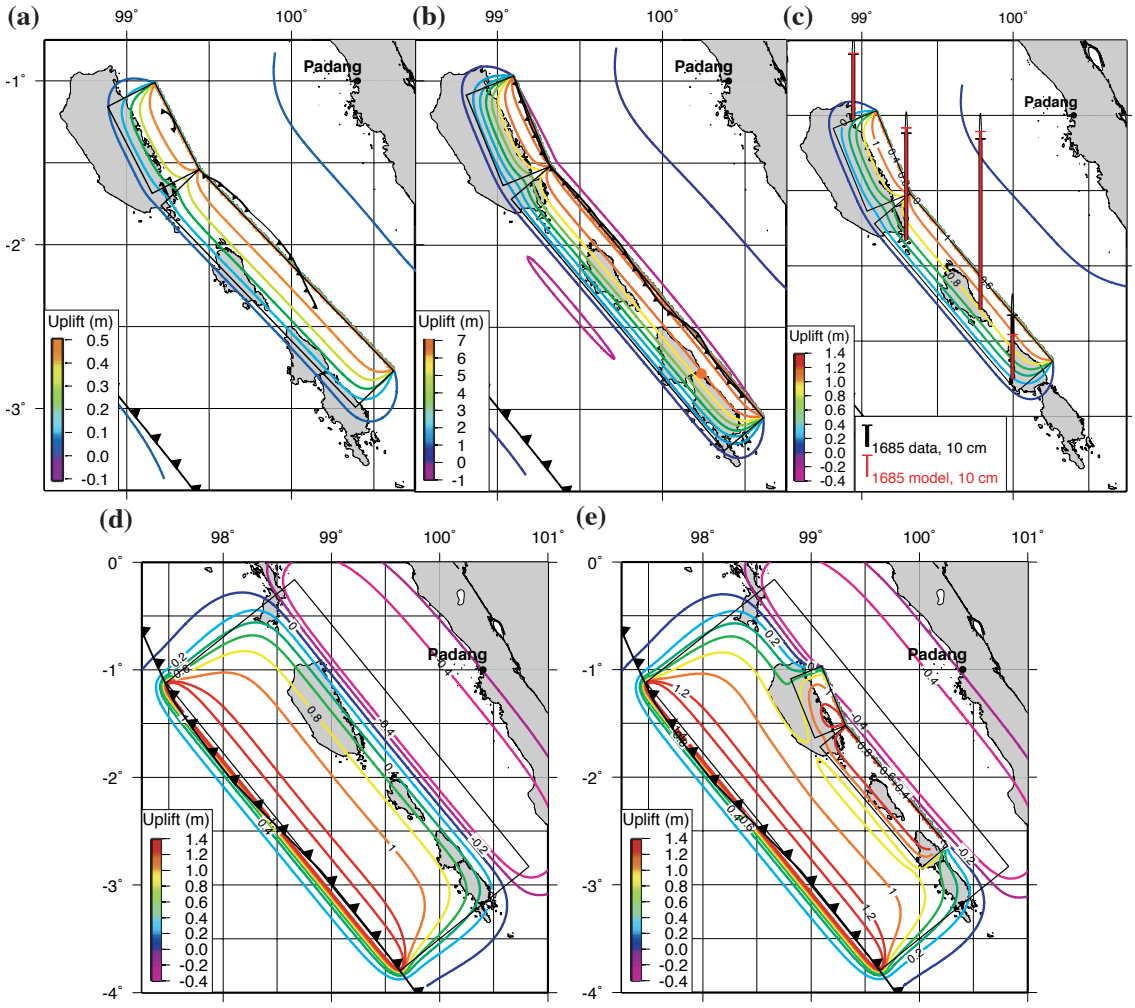

Figure 3.6: Vertical deformation models for historic uplift events. The surface projections of the modeled faults segments are outlined in black and the vertical deformation at the surface is shown by colored uplift contours. (a) FBT deformation model for hypothetical event that slips the entire width of the backthrust from the plate interface until the surface. (b) MBT deformation model for the event between ∼6,500-8,100 BP that caused 6-m of uplift off the northern tip of South Pagai (marked with an orange circle) [Zachariasen, 1998]. (c) MBT deformation model that fits the ∼1685 uplift event microatoll data from Sieh et al. [2008]. The microatoll uplift data is shown with black bars and 1-sigma uncertainties, the modeled uplift is shown with red bars. (d) Deformation model for a megathrust event that ruptures the 1797 segment (a simplified version of the 1797 fault model from Natawidjaja et al. [2006]). (e) Deformation model for a combined megathrust-backthrust event, in this case, the summed contributions from the 1797 and 1685 deformation models.

modeled the vertical deformation from a combined Mentawai segment megathrust event and the 1685 backthrust event (Figure 3.6e) and find that one observes southwestward tilting of the islands. Therefore it may be difficult to distinguish between an independent backthrust event, a combined megathrust-backthrust event, and a deep megathrust event using only vertical paleogeodetic data and one must be cautious when interpreting sparse vertical data.

The past few years of global seismicity have reminded us that large ruptures on faults can occur very infrequently. The damaging Wenchuan earthquake of 2008 has an approximately 3000 year recurrence interval and the unexpected 2011 Tohoku event has a recurrence interval >1000 years. One out of place coral microatoll sitting in the intertidal zone on the northern tip of South Pagai suggests that very large backthrust events may have recurrence intervals of several thousands of years. Mid-Holocene microatolls, ranging in age from about 4,500 to 6,000 years exist within the current intertidal zone at many locations around the Mentawai Islands [Natawidjaja et al., 2006; Zachariasen, 1998] and one would not expect to find older microatolls in the intertidal zone because sea level did not reach the current level until about 6,000 years ago. We speculate that the one microatoll sitting in the intertidal zone, which grew about 8,100 years ago [Zachariasen, 1998], was uplifted ∼6 meters before ∼6,500 BP to account for the change in sea level. This is scant evidence of a rare faulting event that ruptures the entire length of the MBT. With an average 15 m of slip, the backthrust may be capable of producing M_w 8.5+ events (Figure 3.6b).

3.8 Conclusions

The resurgence of earthquake activity on the Mentawai backthrust that we have documented here, including two M_w 6.7 earthquakes, suggests that more work is needed to fully characterize the faults rupture history and magnitude potential. An active backthrust also implies that we need to modify existing models of interplate strain accumulation to account for the buildup of upper plate strain in the forearc region. In addition, tsunami simulations for a range of backthrust earthquake magnitudes are needed to ascertain whether the hazard is locally limited between the east coast of the Mentawai Islands and the densely populated west coast of Sumatra, or if an ocean-wide scenario is possible.

Chapter 4

Source Model of the 2009 M_w 7.6 Padang Intraslab Earthquake and its Effect on the Sunda Megathrust

4.1 Abstract

We investigate the source of the M_w 7.6 Padang earthquake by inverting three-component GPS data and broadband regional seismic-displacement waveforms. The earthquake involved oblique-reverse slip either on an E-W, south-dipping plane, or on a N-S, west-dipping plane. Finite-fault inversions indicate that the rupture primarily propagated downdip and southwest from the hypocenter, with a scalar seismic moment between 3.4 and 3.7×10^{20} N m (M_w 7.62-7.65). Analysis of the seismic and geodetic data do not allow for unique identification of the causative focal plane. Aftershock patterns strongly suggest the E-W plane was the causative focal plane, but aligned geologic structures in the downgoing plate favor the N-S plane. In either case, this unusually large intraslab earthquake has moved closer to failure the deepest portion of the overlying megathrust, which last ruptured during a great earthquake more than two centuries ago and is late in its seismic cycle.

4.2 Introduction

The M_w 7.6 Padang earthquake of 30 September 2009 initiated ∼250 km east of the Sunda trench at ∼80 km depth. At this location the Hayes and Wald [2009] Sunda slab model places the megathrust at ∼69 km depth, thus, this event appears to have occurred within the downgoing oceanic plate. Large, intermediate depth, intraslab earthquakes, such as the 2001 M_w 6.8 Nisqually and 2001 M_w 7.7 El Salvador earthquakes, are often more devastating than comparable magnitude interplate earthquakes because they are located closer to the onshore population centers. They also tend to be normal fault events that can be explained by tension induced by bending of the slab or net slab pull [Vallée et al., 2003; Wada et al., 2010]. The source of the Padang earthquake is particularly worthy of study

for two reasons: the earthquake caused significant damage to the large coastal Sumatran city of Padang, and it was caused by unusual oblique-reverse rupture within the subducting oceanic plate beneath the decade's most seismically active megathrust [McCloskey et al., 2010]. Moreover, the earthquake occurred just below a large span of that megathrust that appears from paleoseismic evidence to be close to failure [Konca et al., 2008; Sieh et al., 2008].

The Sunda subduction zone arcs westward 6,000 km from northwestern Australia, past Java, Sumatra and Myanmar to the eastern axis of the Himalayas. Along the 2,000-km long segment off the west coast of Sumatra (Figure 4.1), subduction is highly oblique, with 45 to 60 mm/yr of convergence [Simons et al., 2007] partitioned almost completely into strike-slip motion on the Sumatran fault and dip-slip motion on the megathrust [Fitch, 1972; McCaffrey, 1991].

Convergence along the Sunda arc involves two subducting plates: southeast of Sumatra the Australian plate dives northward beneath Java, whereas north of Sumatra the Indian plate subducts beneath the Andaman Sea. The boundary between the two subducting plates is a region of diffuse deformation so broad that it spans nearly the entirety of Sumatra, from at least 5.5°S to 2.5°N [Delescluse and Chamot-Rooke, 2007]. Most of the relative motion between the two oceanic plates appears to be occurring along north-striking, left-lateral strike-slip faults [Deplus, 2001; Deplus et al., 1998], and some of these faults are being subducted. For example, one of these faults within the subducting slab may be associated with a persistent barrier to megathrust rupture at about 2.5°N [Meltzner et al., 2012]. Another, the Investigator Fracture Zone (Figure 4.1), appears to profoundly affect the character of subduction near the Equator [Fauzi et al., 1996; Natawidjaja et al., 2004]. Finally, a subducting left-lateral fault was one of the sources of the M_w 7.9 Enggano earthquake that initiated the recent episode of Sumatran megathrust seismicity in 2000 [Abercrombie et al., 2003]. Wharton Ridge, a fossil spreading center, is another prominent bathymetric feature subducting near the Equator (Figure 4.1). Magnetic anomaly data have shown that Wharton Ridge includes several east-west oriented fossil spreading segments [Deplus et al., 1998; Liu, 1983]. Earthquakes within the Sumatran slab may initiate on reactivated faults associated with theses subducted Indian-Australian plate boundary structures.

One of the challenges associated with the 2009 Padang earthquake is determining the rupture geometry. Based on the global centroid moment tensor (GCMT) focal mechanism solution (www.globalcmt.org), the fault plane strikes either east-west with right-lateral oblique-reverse slip or north-south with left-lateral oblique slip. Possible candidates for the rupture plane could be subducted transform faults, fractures, or fossil spreading ridges [Deplus et al., 1998; Liu, 1983] associated with the diffuse Indian and Australian plate boundary. The USGS did not resolve which of these nodal planes was the rupture from their fitting of teleseismic broadband P and SH waveforms and long-period surface waves (`http://earthquake.usgs.gov/earthquakes/eqinthenews/2009/us2009mebz/finite_fault.php`). We attempt to

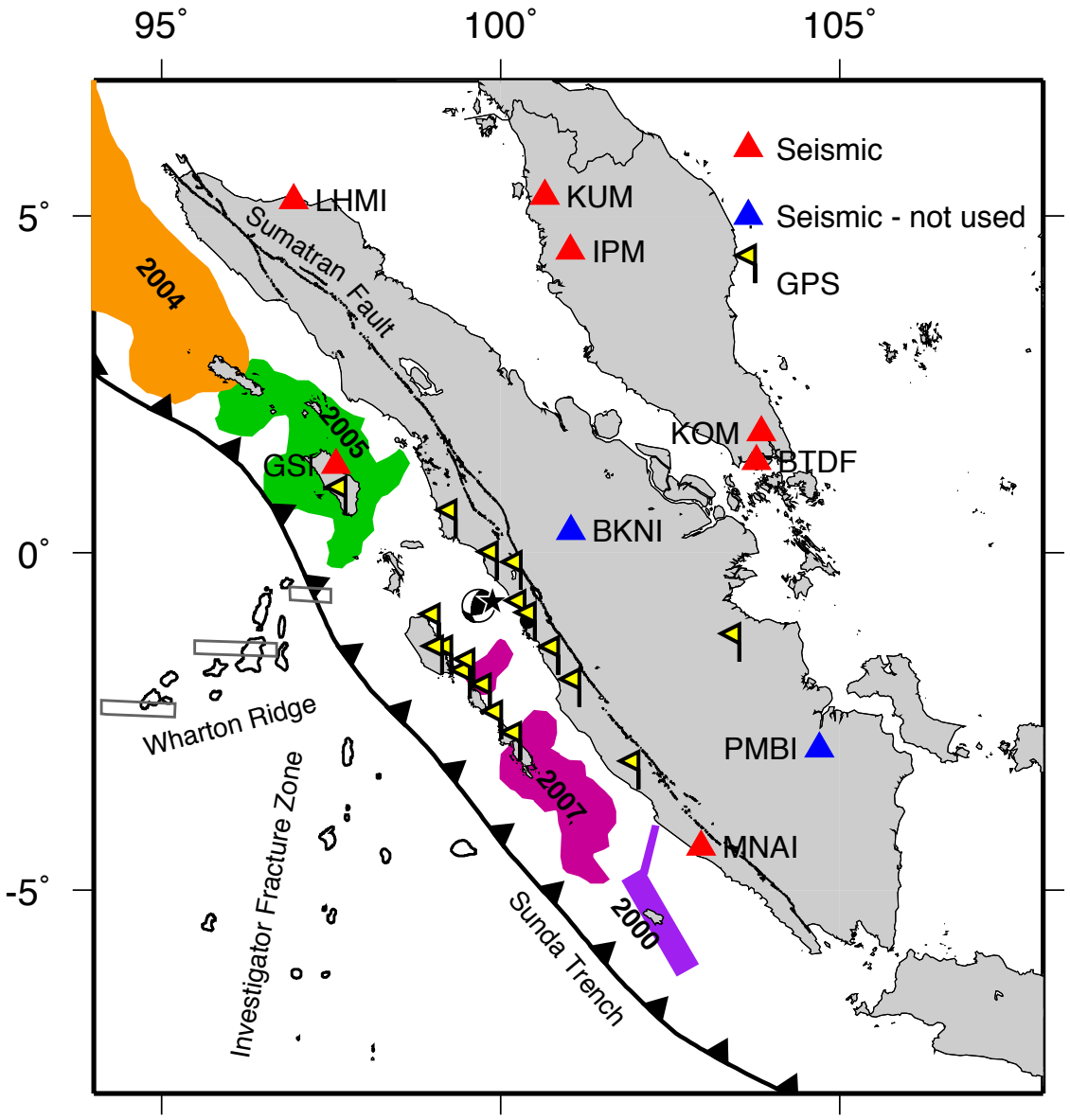

Figure 4.1: Context of the 30 September 2009 earthquake. Epicenter and focal mechanism are west of Padang. Great ruptures of 2000, 2004, 2005 and 2007 are in color, projected to the surface from the underlying megathrust [Abercrombie et al., 2003; Chlieh et al., 2007; Konca et al., 2008, 2007]. Red triangles signify stations with good seismic data that we use throughout the study, whereas blue triangles signify stations with corrupted seismic data. Yellow flags show the Sumatran GPS Array (SuGAr). The 4000 m bathymetry contours highlight the Investigator Fracture Zone and Wharton Ridge. The locations of east-west fossil spreading segments, deduced from magnetic anomalies [Deplus et al., 1998], are shown with gray rectangles.

resolve the fault plane by using regional broadband data, GPS data and aftershock locations.

Nearly all the Sumatran section of the Sunda megathrust has ruptured in the past 8 years. Thus far the sequence has included the 2004 M_w 9.2 Sumatra-Andaman earthquake [Chlieh et al., 2007; Shearer and Bürgmann, 2010], the 2005 M_w 8.7 Nias-Simeulue earthquake [Konca et al., 2007], the 2007 M_w 8.4 Bengkulu earthquake [Konca et al., 2008], and a myriad of lesser events, including the damaging 2010 M_w 7.8 tsunami earthquake [Hill et al., 2012]. One of the two large remaining unbroken sections of the Sumatran portion of the megathrust is a 350-km long section centered beneath Siberut Island, offshore of Padang [Chlieh et al., 2008] (Figure 4.1). The Siberut segment has had a complex stress evolution during the past 8 years, with megathrust ruptures to the northwest and southeast, two clusters of backthrust earthquakes in the upper plate above the section [in Chapter 2 and Wiseman and Bürgmann [2011]] and now a large, deep earthquake below the section. It is therefore especially important to understand the kinematics of the 2009 Padang earthquake to understand how it affects the stress levels on the Siberut segment of the megathrust and how it impacts seismic hazard in the region.

4.3 Data

4.3.1 Broadband Waveforms

Nine three-component broadband stations within 1000 km of the epicenter were operating at the time of the earthquake and have publicly available data (Figure 4.1). The five Indonesian stations, BKNI, GSI, LHMI, MNAI, and PMBI, are part of the GEOFON network and data from these stations were acquired through WebDC (`http://webdc.eu`). Data from BTDF of the Singapore National Network and IPM, KOM, and KUM from the Malaysian National Seismic Network were obtained from IRIS (`http://www.iris.edu`).

The 27 acquired velocity waveforms appear in Figure 4.2 with their instrument responses removed. Unfortunately, the largest amplitudes in the waveforms from the nearest seismic station, BKNI, are clipped. Therefore, we are not able to use the BKNI data in the seismic inversions. PMBI has suspect long-period motion, so we choose to exclude it from the inversions. Thus, there are seven stations with useable data that we integrate to displacement waveforms for the seismic inversions.

The data are first processed by removing the polezero instrument response and integrating to displacement. Both the displacement waveform data and the Green's functions were then bandpass filtered between 0.01 to 0.3 Hz. We use this bandpass because higher frequency components of the displacement waveforms are not resolvable using a 1-D velocity

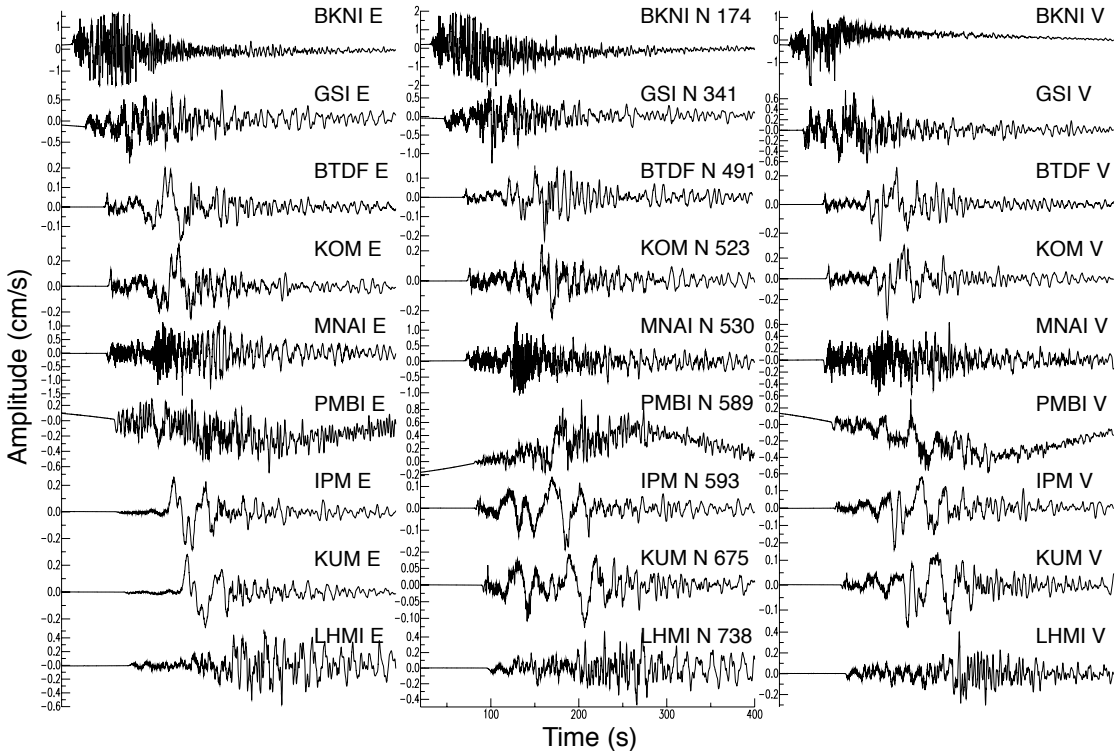

Figure 4.2: Observed velocity waveforms at all of the stations with publicly available data within 1000 km of the Padang epicenter. The epicentral distances (km) are labeled on the north components. The instrument responses have been removed from the data.

model. Lastly, we resample the data at 1.0 second. The maximum waveform amplitude for each component varies from about 0.4 to 1.4 cm.

4.3.2 Geodetic Data

In the inversions, we include 3-component data from 18 permanent GPS stations ranging in distance from 37 to 417 km from the epicenter (Figure 4.1). The GPS stations are part of the Sumatran GPS Array (SuGAr; `ftp://eos.ntu.edu.sg/SugarData/`) and ENS-INSU regional networks [Hermawan, 2010]. Unfortunately, the data from the nearby ENS-INSU campaign GPS stations were noisy and with too large uncertainties to be useful in the inversions. Therefore we do not include campaign GPS data in the study. The raw GPS data was processed using the GAMIT/GLOBK software package [Herring, 2005; King and Bock, 2005] to solve for daily station coordinates. Differencing of position time series 10 days before and

after the Padang earthquake yielded coseismic displacements at each site. We removed from the LNNG time-series a coseismic offset associated with a M_w 6.6 aftershock that occurred 15 hours after the Padang event on the Sumatran fault. That station, only 44 km from the epicenter of this earthquake, is the only station close enough to record a displacement from that event.

In general, the GPS sites along the western coast of the Sumatran mainland experienced coseismic subsidence and horizontal motion toward the earthquake's epicenter. The sites on the Mentawai islands, west of the epicenter, experienced uplift and horizontal motion away from the epicenter and toward the trench (Figure 4.3). The largest horizontal displacements, up to ∼5 cm, occurred at sites MSAI, TLLU, and NGNG, on Siberut Island. The largest vertical displacement, ∼3 cm of subsidence, occurred on the west coast of Sumatra at site SCCN. However, the vertical measurements have large uncertainties that are comparable to the amplitude of the signal at most stations.

4.4 Inversion Method

4.4.1 Model Geometry

We use the geodetic data to constrain the input model geometry for the finite fault inversions. The geometry inversion method uses a constrained, nonlinear optimization algorithm to solve for the best-fit, uniform-slip rectangular dislocation [Bürgmann et al., 1997] in an elastic half-space [Okada, 1985]. We used the GCMT nodal plane strike, dip and rake with fault dimensions based on Wells and Coppersmith [1994] scaling laws for the starting fault geometries. We loosely bounded the geometry inversion parameters: the strike and dip within 15° of the starting models, length within 50 km, width within 15 km, and location within 1° latitude and longitude. The optimal east-striking nodal plane (EWNP) fault geometry has a strike of 80° and dip of 57°, and the south-striking nodal plane (NSNP) has a strike of 190° and dip of 61°. Our geodetically constrained strike and dip values are within 6° of the GCMT moment tensor solution values for both nodal planes. The geodetic centroid for both nodal planes is located southeast of the GCMT centroid, ∼20 km south of the Engdahl relocated earthquake catalog (EHB; E. R. Engdahl unpublished data using method of Engdahl et al. [2007]) epicenter at an average of 78 km depth.

We adopt the optimal fault strike and dip parameters from the geometry inversion and solve for distributed slip with variable rake in the finite fault inversions. Our model fault plane extends 90 km along strike by 65 km downdip, divided into 5 × 5 km patches. For the finite fault inversions, We assume the EHB epicenter with a depth of 78 km for the hypocenter location. The hypocenter depth matches our geometry inversion centroid depth and the

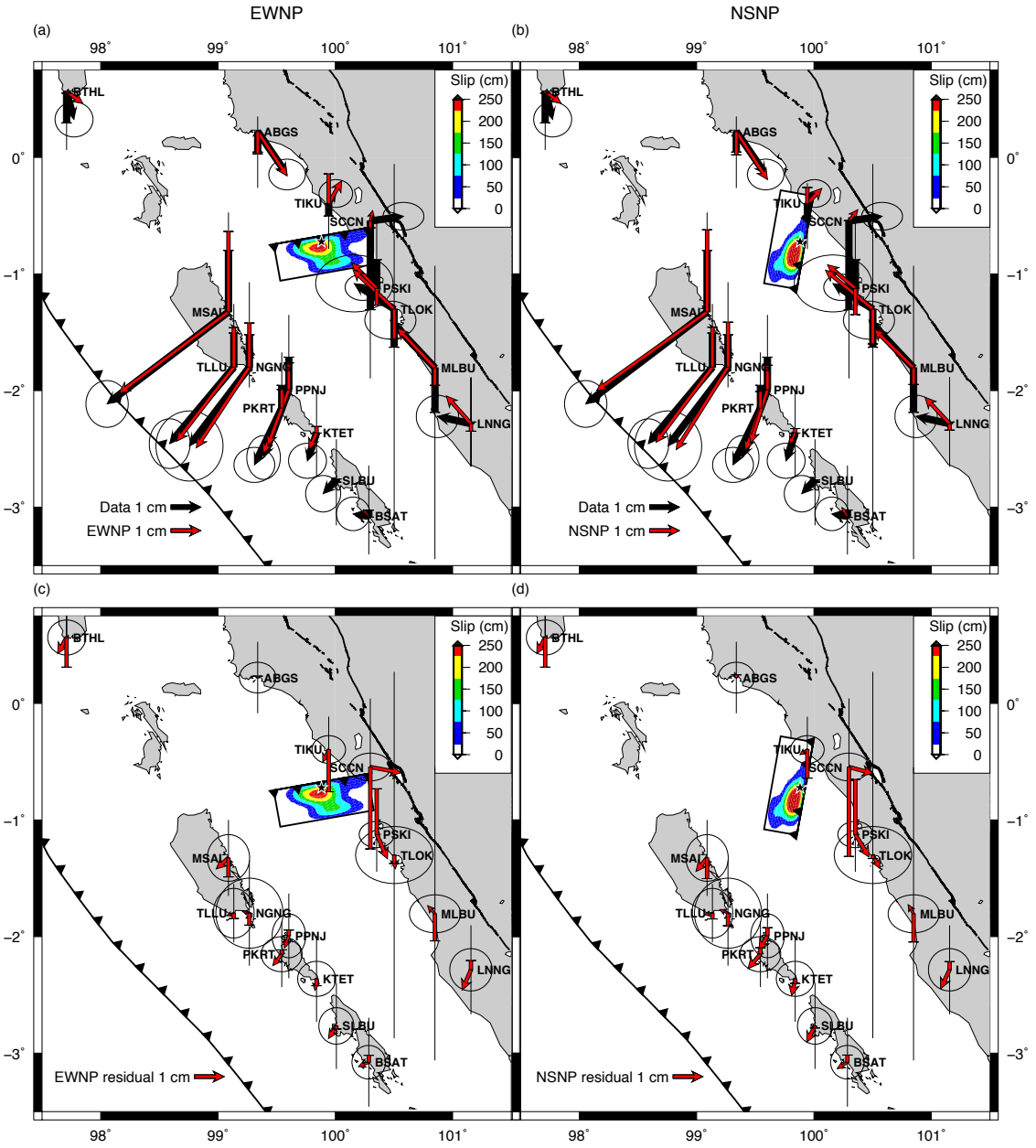

Figure 4.3: Comparison of GPS data and joint model displacement vectors for (a) the east-west nodal plane (EWNP) and (b) the north-south nodal plane (NSNP). Residuals between the joint model and GPS data are shown in (c) and (d). The corresponding distributed slip models are shown by color contours on the fault planes projected to the surface.

GCMT centroid depth. We did not use the EHB or National Earthquake Information Center (NEIC) catalog depth for the hypocenter because both catalogs fix the hypocenter depth. We place the hypocenter within the central position along strike and 10 km downdip from the upper edge of the two modeled faults (cross section view of fault planes shown in Figure 4.7). This hypocenter location prevents slip from propagating shallower than the megathrust interface. The fault plane dimensions are extended from the geometry inversion to include the preferred geodetic centroid location south of the hypocenter.

4.4.2 Green's Functions

The seismic Green's functions for the finite fault inversions are computed using a 1-D frequency-wavenumber integration method [Saikia, 1994]. We calculate Green's functions at 5-km distance intervals and at 4-km depth intervals. For the input earth model, we test two 1-D velocity models based on local earthquake travel-time tomography. The attenuation quality factors are from PREM [Dziewonski and Anderson, 1981] and the density structure is similar to PREM but with higher crustal densities appropriate for the Sumatra region [Pollitz et al., 2006b].

We first tested the minimum 1-D velocity model from Lange et al. [2010] (Table 4.1). The Lange et al. [2010] velocity model is inverted from local earthquake arrivals using a temporary deployment of land-stations and ocean bottom seismometers, as well as the GEOFON and BMKG permanent stations. The majority of the seismic stations span the ocean and Sumatran mainland between the latitudes of Nias and Siberut islands, just north of the Padang earthquake. The velocity model inversion is dominated by the large number of stations along the Sumatran Fault, with events located at crustal depths and in the Wadati Benioff zone, and is therefore a good model of Sumatran continental lithosphere velocity structure between 10 to 125 km depths.

Next we tested the minimum 1-D Vp model from Collings et al. [2012] with a range of Vp/Vs ratios from 1.8-1.9 (Table 4.2). The seismic stations for the Collings et al. [2012] study were deployed following the 2007 M_w 8.4 Bengkulu earthquake on the Mentawai islands and Sumatra mainland between $1^\circ - 4^\circ$S, just south of the Padang rupture. We find that a Vp/Vs ratio of 1.85 best fits the seismic data. The Vp velocities are higher in the Collings model than the Lange model, but the Vs velocities are lower. The Collings velocity structure has a few percent better variance reduction than the Lange velocity structure in the seismic inversions, and allows for less model smoothing. Therefore we will use the Collings model throughout the rest of the study.

The Green's functions for the geodetic modeling are constructed using the programs EDGRN/EDCMP [Wang et al., 2003], on a layered half-space with the preferred Collings model.

Table 4.1: The Lange earth model with velocity structure from Lange et al. [2010], densities from Pollitz et al. [2006b] and attenuation quality factors from PREM [Dziewonski and Anderson, 1981].

Layer Thickness (km)	Vp (km/s)	Vs (km/s)	Density (g/cm3)	Qp	Qs
3	5.27	3.20	2.5	57822	600
3	5.27	3.20	2.5	57822	600
3	5.27	3.20	2.5	57822	600
3	5.27	3.20	2.5	57822	600
3	5.27	3.20	2.5	57822	600
3	5.27	3.20	2.5	57822	600
3	5.27	3.20	2.5	57822	600
3	5.27	3.20	2.5	57822	600
3	5.27	3.20	2.5	57822	600
3	5.27	3.20	2.5	57822	600
3	5.27	3.20	2.5	57822	600
3	5.27	3.20	2.5	57822	600
3	5.27	3.20	2.5	57822	600
3	5.27	3.20	2.5	57822	600

Table 4.2: The Collings earth model with a Vp/Vs ratio of 1.85. The velocity structure is from Collings et al. [2012], the densities from Pollitz et al. [2006b] and attenuation quality factors are from PREM [Dziewonski and Anderson, 1981].

Layer Thickness (km)	Vp (km/s)	Vs (km/s)	Density (g/cm3)	Qp	Qs
3	5.27	3.20	2.5	57822	600
3	5.27	3.20	2.5	57822	600
3	5.27	3.20	2.5	57822	600
3	5.27	3.20	2.5	57822	600
3	5.27	3.20	2.5	57822	600
3	5.27	3.20	2.5	57822	600
3	5.27	3.20	2.5	57822	600
3	5.27	3.20	2.5	57822	600
3	5.27	3.20	2.5	57822	600
3	5.27	3.20	2.5	57822	600
3	5.27	3.20	2.5	57822	600
3	5.27	3.20	2.5	57822	600
3	5.27	3.20	2.5	57822	600
3	5.27	3.20	2.5	57822	600
3	5.27	3.20	2.5	57822	600
3	5.27	3.20	2.5	57822	600
3	5.27	3.20	2.5	57822	600
3	5.27	3.20	2.5	57822	600
3	5.27	3.20	2.5	57822	600
3	5.27	3.20	2.5	57822	600

4.4.3 Finite Fault Inversion Method

We use a least-squares inversion method that employs simultaneous smoothing and damping to invert for finite fault slip [Hartzell and Heaton, 1983; Kaverina et al., 2002]. The technique inverts for fault slip over a grid of point sources that are triggered by a passing rupture front. We assume a circular rupture front and test a range of rupture velocities between 2.5 km/s to 5.5 km/s (Figure 4.4b). For the rupture velocity sensitivity tests, we use a dislocation rise time of 2.9 seconds, based on the scaling relationship between rise time and moment magnitude from Somerville et al. [1999]. The modeled slip distribution shifts from high peak slip focused at the hypocenter to diffuse slip offset from the hypocenter when shifting from the lower to the higher range of the tested rupture velocities (Figure 4.5). The variance reduction only differs by 2% within the tested velocity range, peaking between 4.5-5.0 km/s. The small range of variance reductions does not warrant using super shear rupture velocities so we chose to use a lower rupture velocity of 4.0 km/s, equal to 0.9 times the shear wave velocity at the hypocenter, for the rest of the study.

Next we tested the sensitivity of the seismic models to rise time. We tested values between $2.9 - 10.0$ seconds (Figure 4.4a). Shorter rise times are not resolvable using the $0.01 - 0.3$ Hz bandpass. Variance reduction decreases with increasing rise time, and differs by 10% between 2.9 and 10 seconds. Therefore, we use 2.9 seconds throughout the rest of the study, based on both the Somerville et al. [1999] scaling relationship and the sensitivity test.

4.5 Inversion Results

4.5.1 Seismic Waveform Inversions

The initial finite fault inversion for both nodal plane geometries does a fairly good job of fitting the waveform amplitudes and polarities (Figure 4.6a), with variance reductions for EWNP and NSNP both equal to 63%. The peak slip region for EWNP is 15 km to the west and 10 km below the hypocenter (Figure 4.7a). For NSNP, the peak slip region is 15 km to the south but starts just below the hypocenter (Figure 4.7b). Both nodal planes have one peak slip region that tapers towards the model boundaries.

However, due to the use of a 1-D velocity model, there are artificial time shifts between the Green's functions and the observed displacement waveforms. Therefore, we shifted the timing of the observations, between 1-6 seconds, so that the S-wave arrival aligns with the synthetic S wave at each site. By shifting the observation times, the variance reductions for both EWNP and NSNP improved to 66% (Figure 4.7c,d). These time shifts account

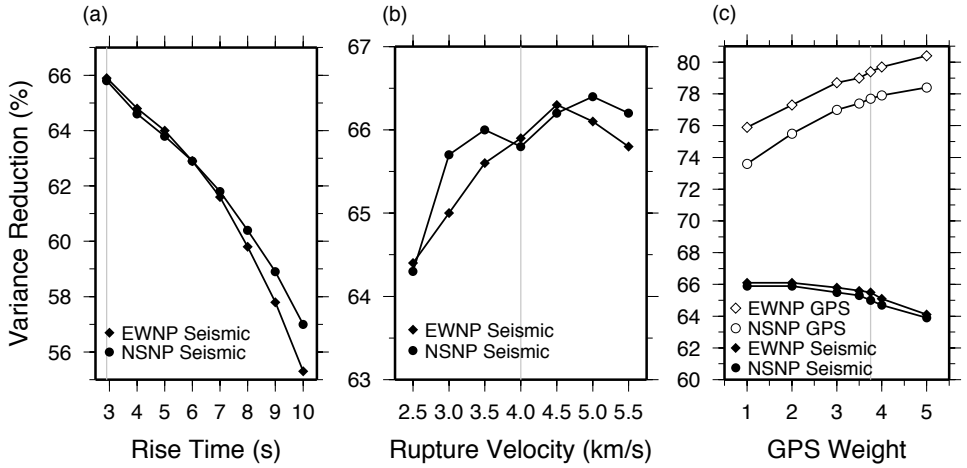

Figure 4.4: Seismic sensitivity tests. (a) Variance reduction versus rise time. (b) Variance reduction versus rupture velocity. (c) Weight of the GPS data with respect to the seismic data (weight of 1) versus model fit. The preferred values are marked with gray lines.

for unmodeled heterogeneity in the actual velocity structure due to the use of a single 1-D velocity model for computing Green's functions.

There are no significant differences in waveform fit between the two nodal planes (Figure 4.6b). They both fit all of the main waveform features except for the last high amplitude phase on the north component of stations BTDF and KOM. These stations are located close together, in Singapore and southern Malaysia, and the poor-fitting north component may be due to strong horizontal anisotropy along this azimuth, which is approximately perpendicular to the strike of the subducting slab.

The high-slip region for both nodal planes moves closer to the hypocenter after time shifting the data. In addition, the slip distributions become more compact, with fewer fault patches requiring slip (Figure 4.7). The total seismic moment for both nodal planes varies by only $\sim 3 \times 10^{18}$ N m, with EWNP moment equal to 3.79×10^{20} N m (M_w 7.65) and NSNP equal to 3.76×10^{20} N m (M_w 7.65). Although we allowed variable rake in the inversions, the rakes are very consistent at all of the fault patches with slip greater than 50 cm. For EWNP, the rake ranges from 133°-155° for the patches with at least 50 cm of slip, and the slip-weighted average rake for all fault patches is 134°. For NSNP, the rake ranges from 30°-51° for patches with at least 50 cm of slip and the slip-weighted average rake is 44°.

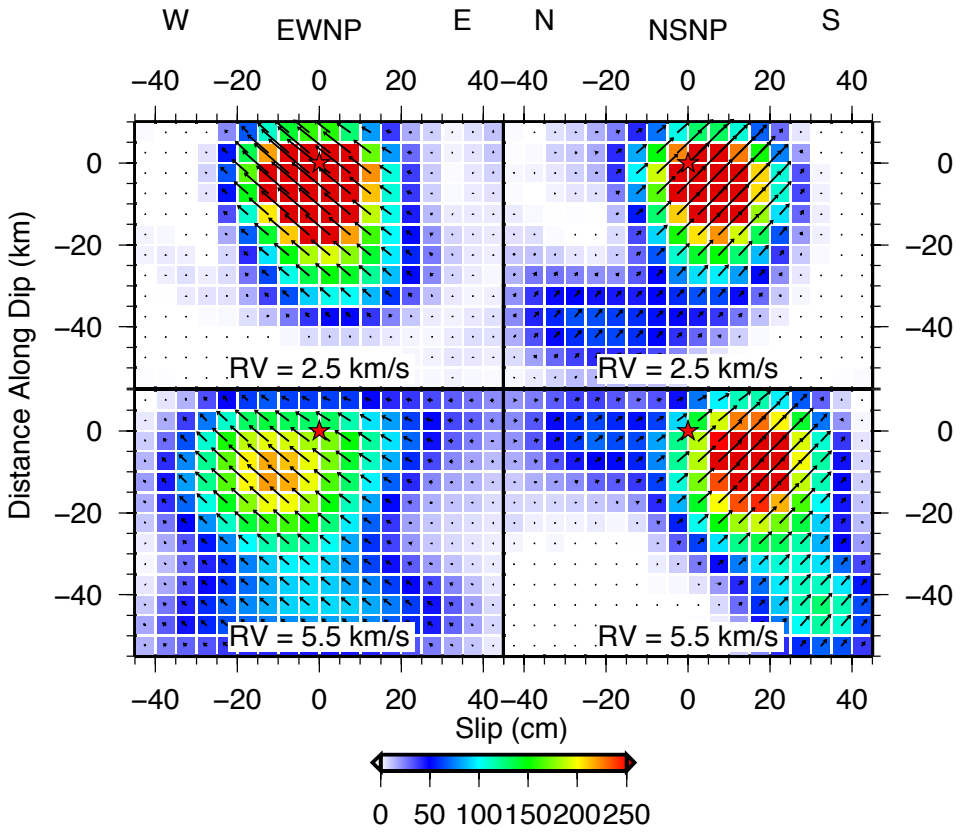

Figure 4.5: Slip distributions for the Collings finite fault models illustrating the effect of variable rupture velocity. Slower rupture velocity places higher peak slip near the hypocenter and focuses the slip distribution.

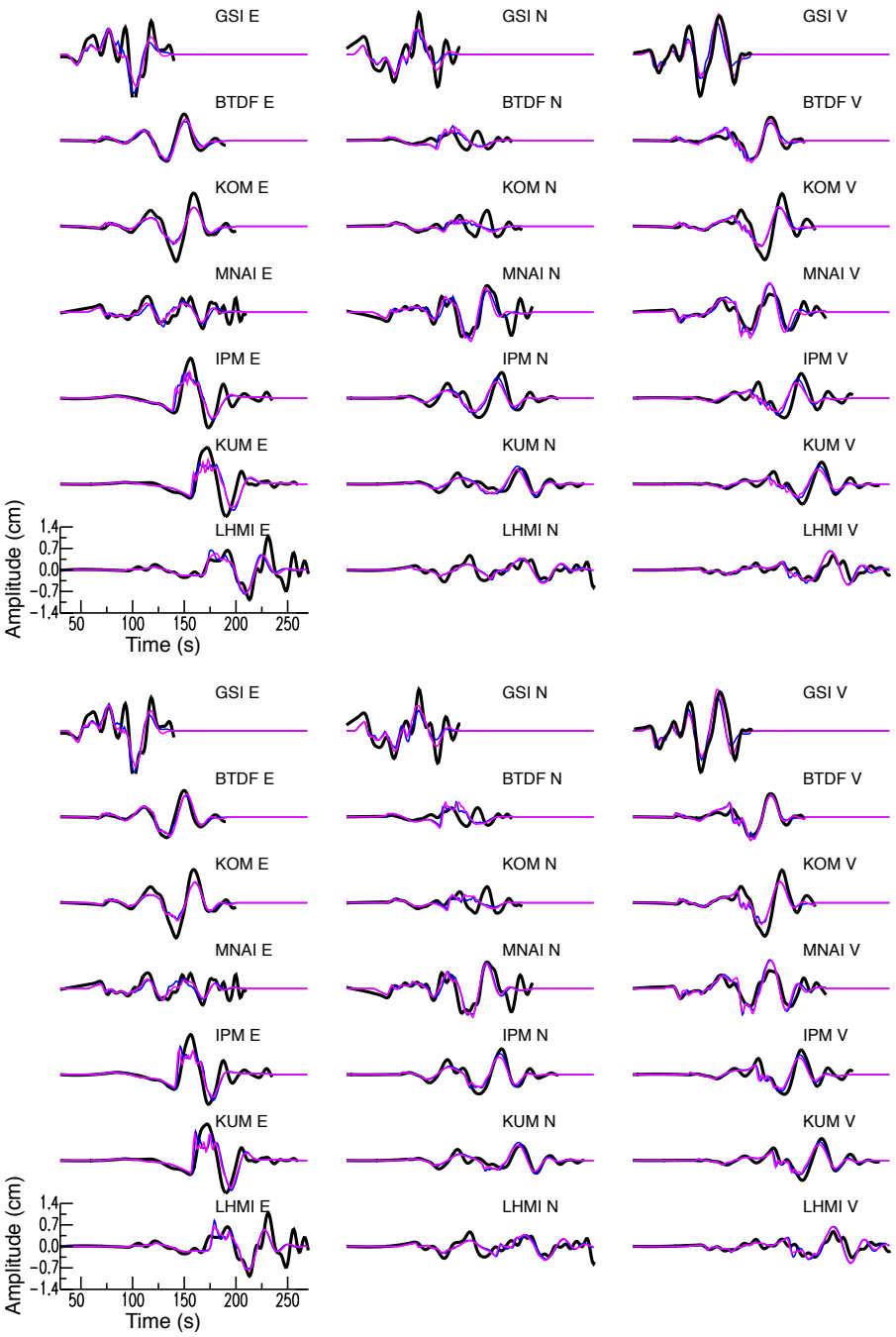

Figure 4.6: Comparison of displacement data and synthetics for the seismic finite fault models using the Collings earth model. (a) Collings earth model (Table 4.2) with total seismic variance reductions of 63% for EWNP and 63% for NSNP and (b) Collings earth model with variable time shifts (preferred) with total seismic variance reduction improving to 66% for EWNP and 66% for NSNP. The data is plotted in black, EWNP synthetics in blue, and NSNP synthetics in magenta. The models use the same smoothing coefficient of 1×10^{-6}.

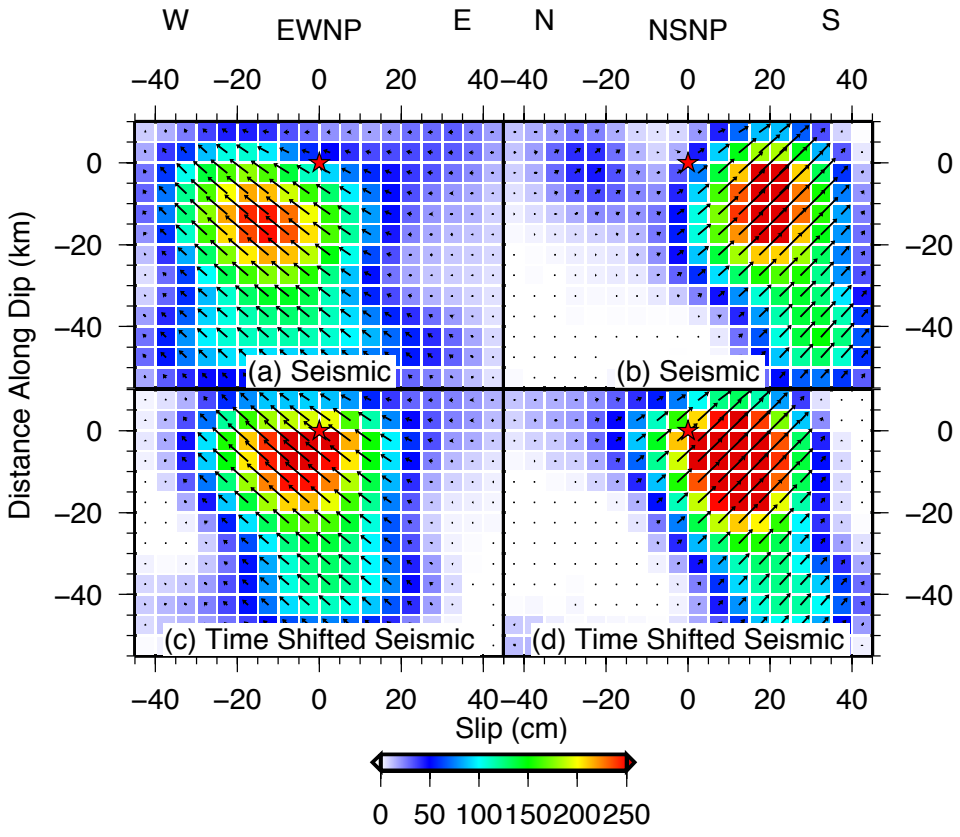

Figure 4.7: Comparison of slip distributions for seismic finite fault inversions. (a,b) without time shifts, and (c,d) including variable station time shifts (preferred). The peak slip regions for the time-shifted models are closer to the hypocenter than for the un-shifted models. The variance reductions also improve from 63% to 66% for both EWNP and NSNP.

4.5.2 Geodetic Inversions

In the GPS-only inversions, there are greater differences between the two modeled fault geometries than when using the seismic data (Figure 4.8). The inverted slip distribution for EWNP is more sensitive to the smoothing coefficient than the slip distribution for NSNP. As you increase the weight put on the Laplacian smoothing constraint for EWNP, three high-slip asperities on the eastern corners and top western corner of the fault plane focus to a large, central slip distribution (Figure 4.9). The preferred GPS EWNP model has a broader slip distribution, with lower peak slip than the GPS NSNP model or either seismic model (Figure 4.8a,b). Peak slip is ∼20 km deeper in the GPS EWNP inversion than in the seismic inversion. Slip distribution along NSNP is very stable over a wide range of smoothing coefficients. Its slip is tightly focused, with a peak value of ∼320 cm, ∼130 cm higher than for EWNP. NSNP has a scalar seismic moment of 3.19×10^{20} N m (M_w 7.60) and EWNP has a total moment of 3.76×10^{20} N m (M_w 7.65).

The total variance reduction for EWNP is 80% and for NSNP is 78%. The EWNP model fits all of the observed displacements within their 95% confidence ellipse except for the three nearest stations on the west coast of Sumatra (TIKU, SCCN, and PSKI) and BTHL on the southern tip of Nias (Figure 4.10). The NSNP model fits all of the sites except SCCN, PSKI, BTHL and MSAI. A single fault plane with relatively smooth slip distribution, at the depth range of the subducting slab, cannot fit the complicated displacement field observed at the sites near Padang.

4.5.3 Joint Inversions

Next we combine the seismic waveform and GPS data to better constrain the inversions. There are data points every second for the seismic displacement data, with data time span ranging from 110 seconds to 240 seconds for the seven 3-component stations. This totals 3960 seismic data points compared to 54 GPS data points for the 18 3-component stations. After normalizing for the difference in observation points, we optimized the data weights in order to get the smallest decrease in variance reduction when going from the individual to joint inversions. Figure 4.4c shows how the seismic and geodetic model fits vary with increasing GPS data weight from 1.0 to 5.0 (with respect to seismic weight of 1.0). Using a GPS weight of 3.75 minimizes the decrease in variance reduction when going from the individual to joint inversions.

When using the GPS data weight of 3.75 and the same smoothing coefficient as with the independent seismic inversions, the seismic variance reduction stays at 66% and the GPS variance reduction drops 1% to 79% for the joint EWNP inversion. The seismic variance reduction also drops 1% to 65% for the NSNP joint inversion and the GPS variance reduction

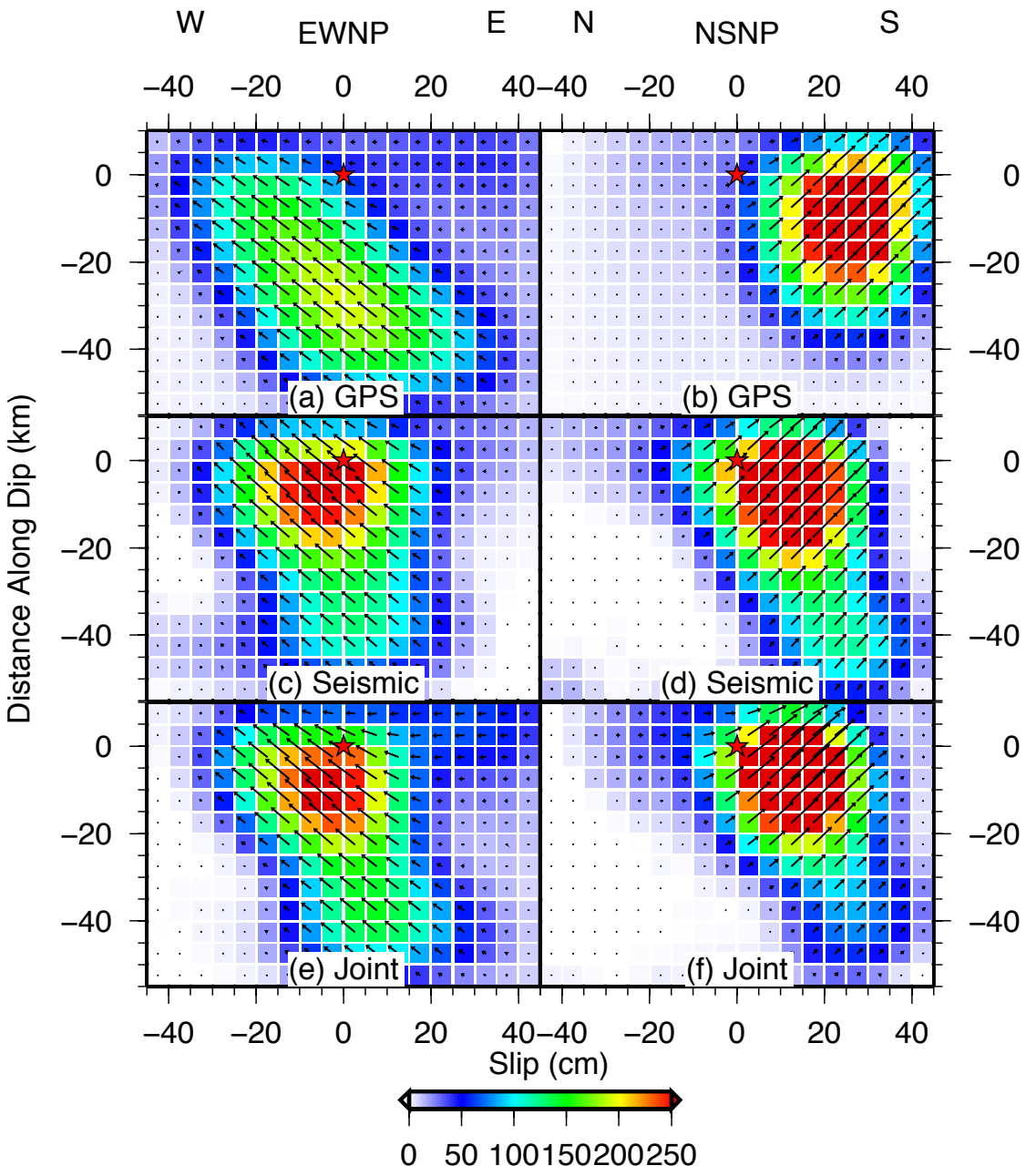

Figure 4.8: Slip distributions for the preferred finite-fault models, using the Collings velocity structure and variable station time shifts. (a) EWNP GPS-only inversion, (b) NSNP GPS-only inversion, (c) EWNP seismic-only inversion, (d) NSNP seismic-only inversion, (e) EWNP joint inversion, (f) NSNP joint inversion. The red star is the EHB hypocenter. The arrows signify the variable rake orientations scaled by slip.

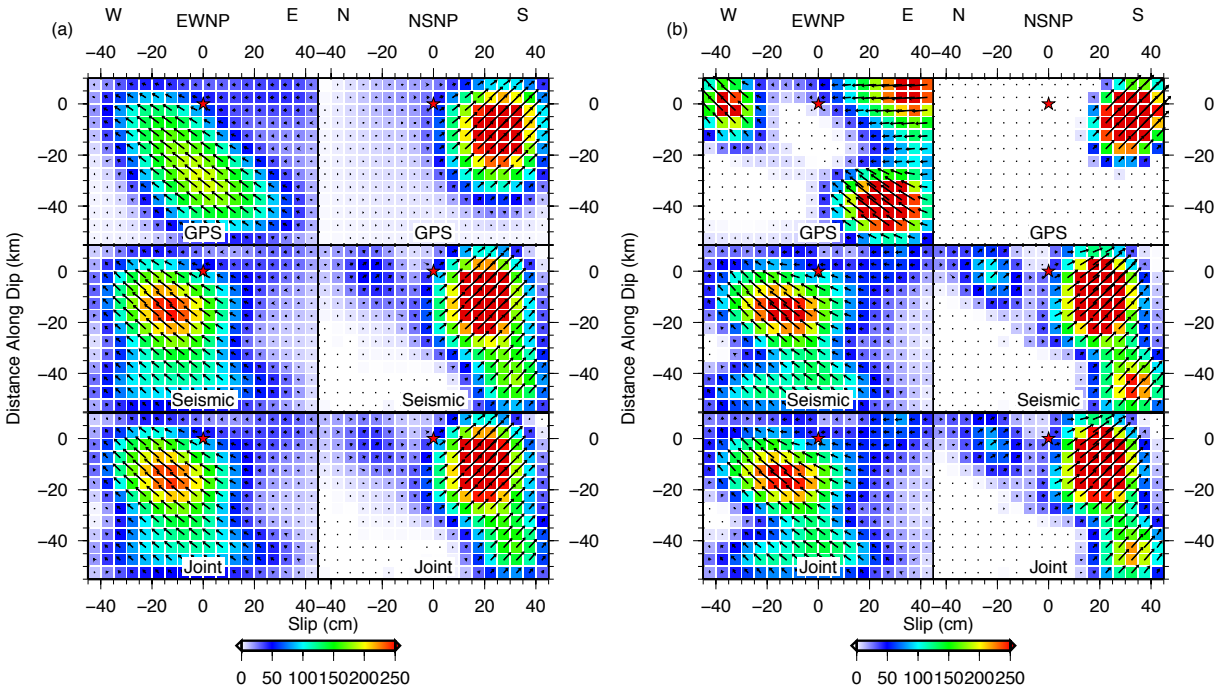

Figure 4.9: Slip distributions for the Collings finite fault models illustrating the effect of variable smoothing coefficients. (a) 5×10^{-9} smoothing coefficient for the GPS models and 1×10^{-6} smoothing coefficient for seismic and joint models (with equally weighted GPS and seismic data). (b) 1×10^{-9} smoothing coefficient for the GPS models and 5×10^{-7} smoothing coefficient for seismic and joint models (with equally weighted GPS and seismic data). The EWNP slip distribution is very sensitive to smoothing coefficient for the GPS models (both for Collings and Lange models), but the seismic slip distribution is less sensitive when using the Collings model and can have less imposed smoothing.

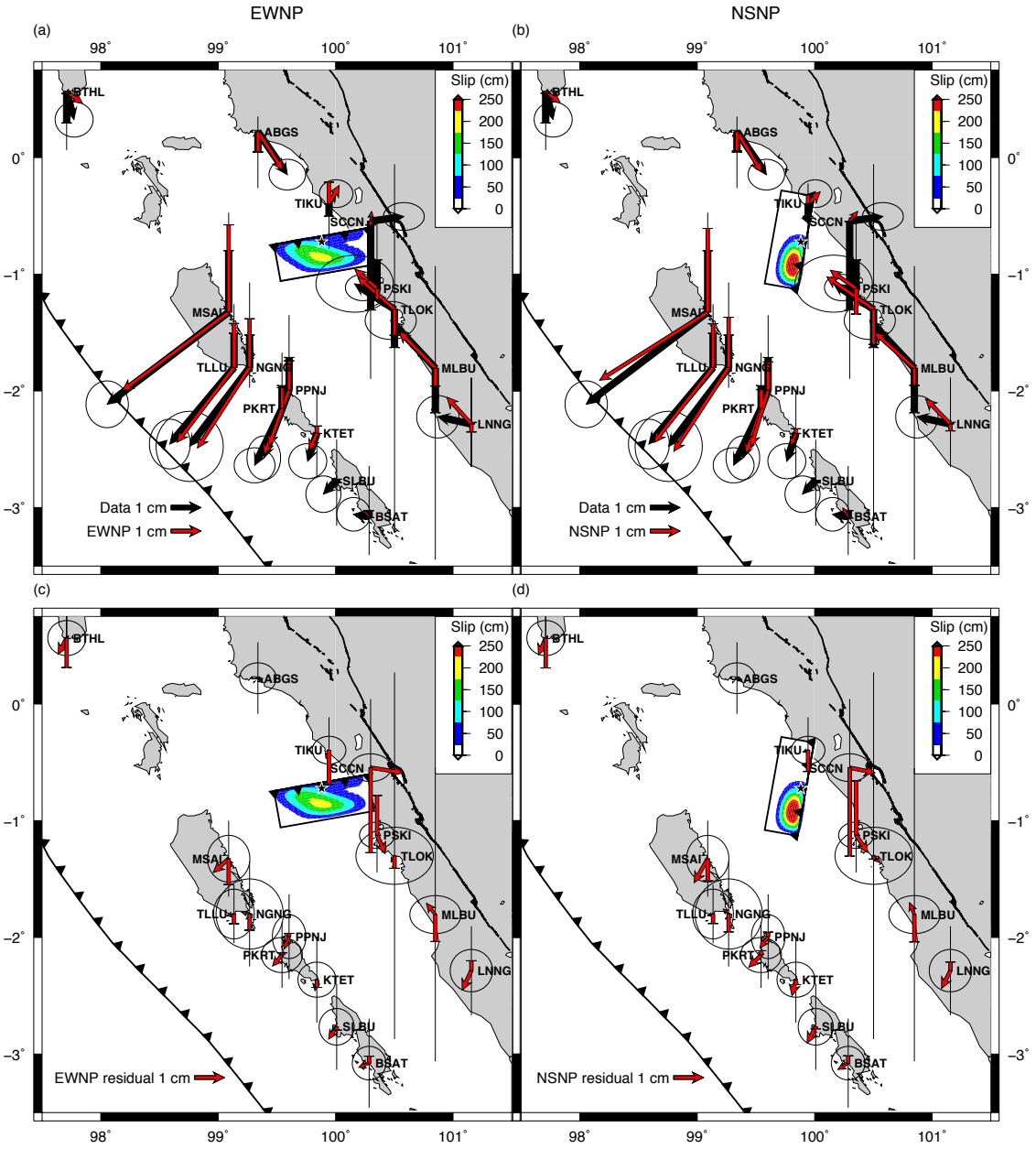

Figure 4.10: Comparison of GPS data and GPS-only model displacement vectors for the EWNP (a) and the NSNP (b). Residuals between the GPS-only model and GPS data are shown in (c) and (d). The corresponding distributed slip models are shown by color contours on the fault planes projected to the surface.

continues to be 78%. There are no notable differences between the waveforms synthetics for the individual and joint inversions (Figure 4.6a and Figure 4.11). The very similar independent and joint variance reductions show that the two datasets are consistent.

The EWNP joint slip distribution is more similar to the individual seismic model than to the GPS model (Figure 4.8a,c,e). The high-slip region stays the same and the lower-slip patches taper more towards the eastern edge of the fault in accordance with the GPS model. The scalar seismic moment for the joint inversion is 3.74×10^{20} N m (M_w 7.65), consistent with the individual moments. The same four GPS stations: BTHL, TIKU, SCCN, and PSKI are not fit within uncertainties in the joint model (Figure 4.3a,c).

The NSNP joint slip distribution is a balance of the two independent slip distributions. The high-slip region starts just south of the hypocenter, like the seismic model, but there's less deep slip like the GPS model (Figure 4.8b,d,f). The scalar seismic moment for the joint inversion is 3.42×10^{20} N m (M_w 7.62), in between the two individual moments. The joint model fits the GPS station MSAI better and is now within the uncertainties. However, BTHL, SCCN, and PSKI still do not fit within the uncertainties (Figure 4.3b,d).

For comparison, we calculate the best point source model searching over a range of source duration. The highest variance reduction is achieved using a duration of 15 seconds. The point source model is comparable to a finite source with a 60 km source dimension, which is similar to the dimension of the joint finite fault models. The point source model fits the GPS data nearly as well as the finite models, with total GPS data variance reduction of 68% (Figure 4.12). However, the seismic variance reduction is greatly reduced to 10% (Figure 4.13). The finite fault models improve the fit to the seismic data by accounting for the spatial variation in radiation pattern across the fault due to the variable slip and to a lesser extent variable rake.

4.6 Aftershocks

In Figure 4.14, we have plotted one month of aftershocks following the Padang earthquake in both map view and depth section. Events are taken from the EHB catalog, the NEIC catalog, and the International Data Center (IDC) catalog (NEIC and IDC data retrieved from the International Seismological Centre On-line Bulletin). There are no aftershocks large enough to have GCMT focal mechanisms within the first month. We have chosen to include multiple catalogs to balance the location accuracy with the number of events. The EHB catalog has the highest location accuracy, but also the fewest number of events, with only 4 aftershocks greater than mb 4.4. The NEIC catalog includes 8 aftershocks greater than mb 4.2. The IDC catalog has the least certain locations, but includes events with magnitudes

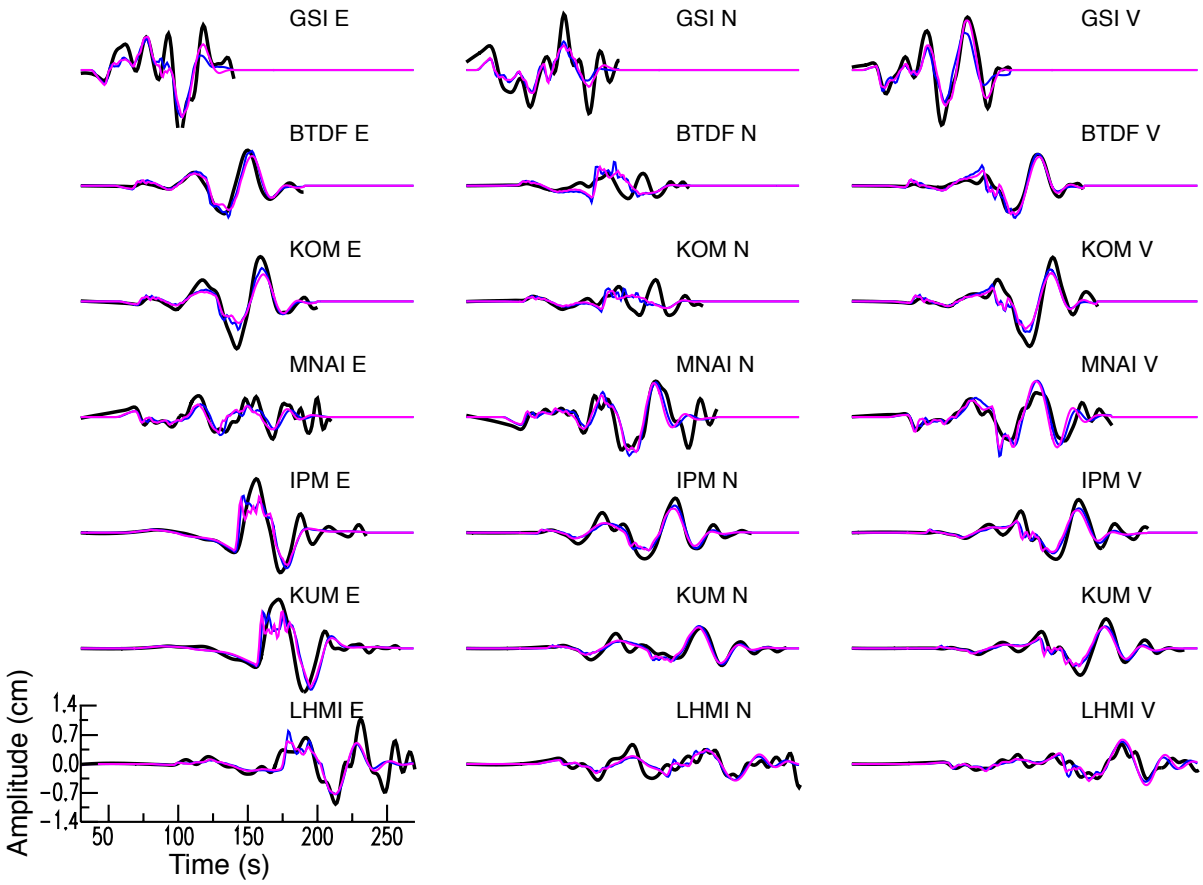

Figure 4.11: Displacement data and synthetics for the preferred joint finite fault models using Collings velocity structure with station time shifts (cross-sections of slip distributions are shown in Figure 4.8e,f). The data is plotted in black, EWNP synthetics in blue, and NSNP synthetics in magenta.

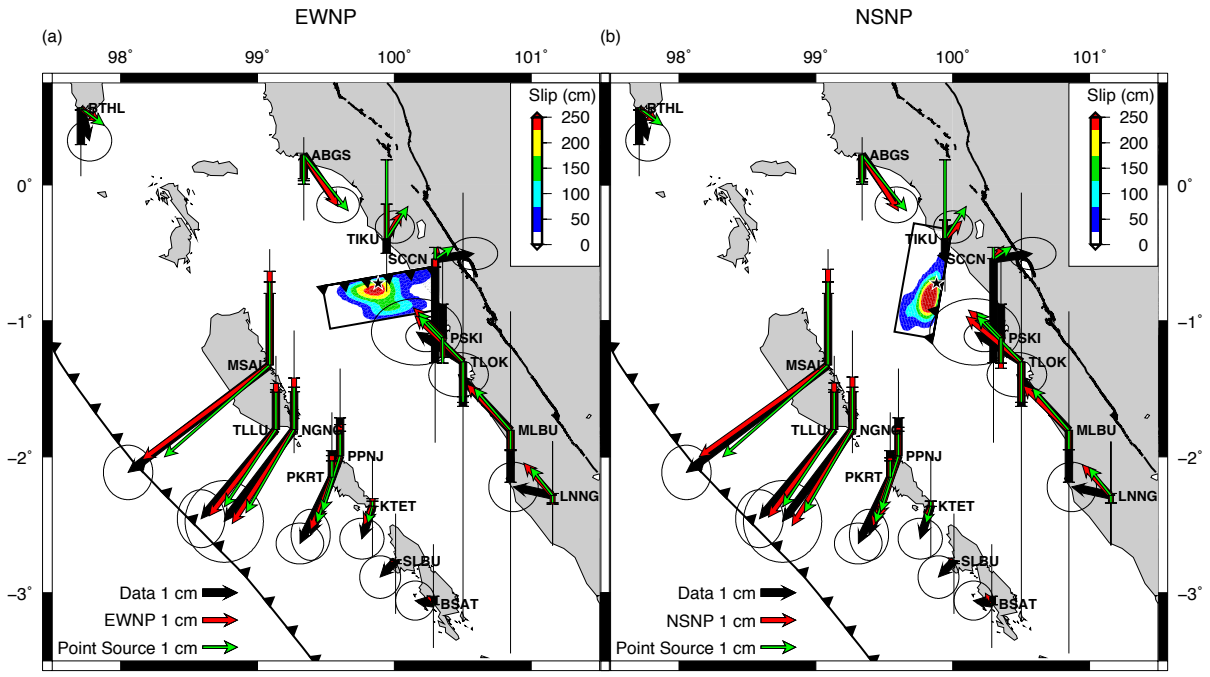

Figure 4.12: Comparison of joint finite fault model and point source model displacement vectors for the EWNP (a) and the NSNP (b). The GPS data variance reduction decreases from 79% (EWNP) and 78% (NSNP) to 68% for the point source model.

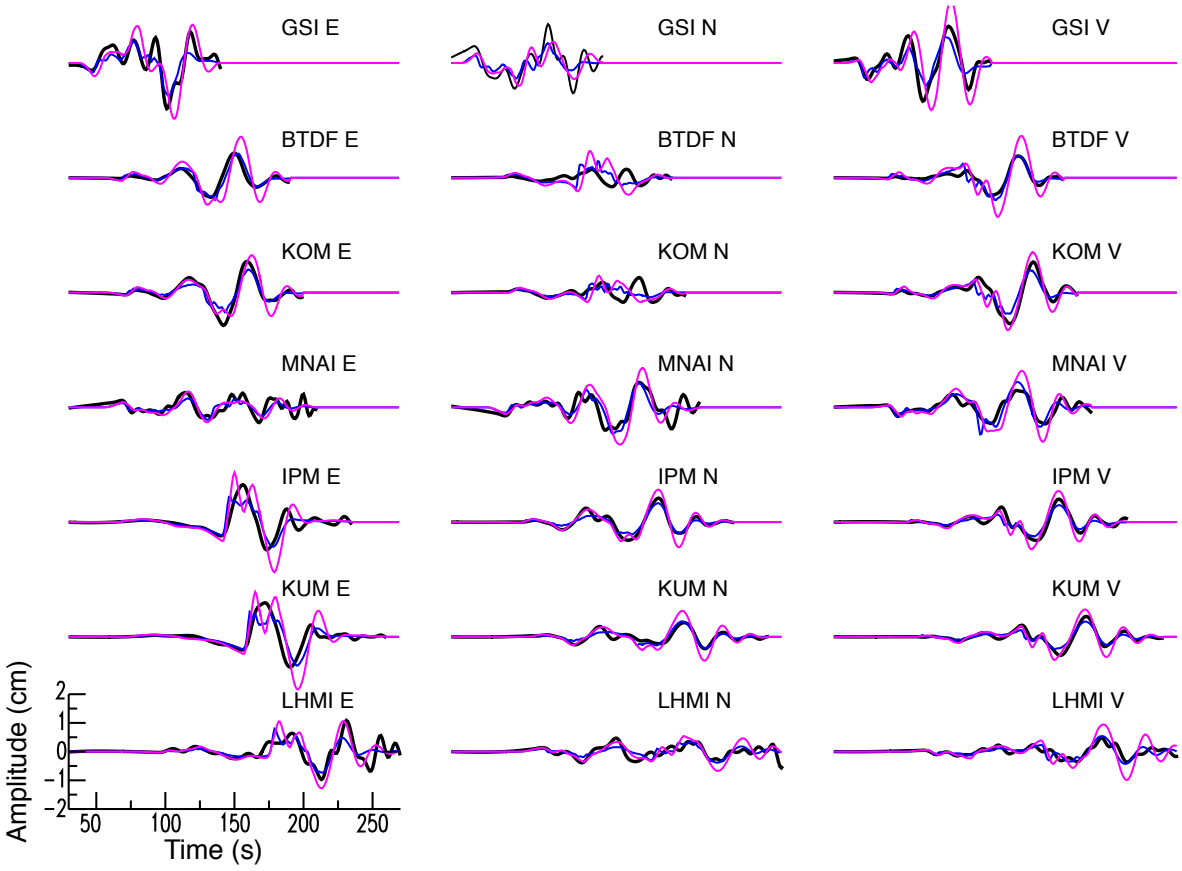

Figure 4.13: Comparison of synthetics for the preferred joint finite fault model (EWNP) and a point source model. The data is plotted in black, EWNP synthetics in blue, and point source synthetics in magenta. The total seismic variance reduction decreases from 66% to 10% when switching from the finite fault to point source model

down to mb 3.0, including 8 magnitude 4 events and 36 magnitude 3 events. We have plotted all of the events from the three catalogs on the map view figures, and only magnitude 4+ events on the depth section to exclude the large depth uncertainties associated with the magnitude 3 aftershocks. The map view figures highlight the preferential alignment of the aftershock epicenters with the strike of the EWNP. The depth sections emphasize the agreement between the larger magnitude aftershock locations and the EWNP high slip region ($>$ 150 cm slip) between 74-97 km depth.

4.7 Stress Interactions Within the Subduction Zone

4.7.1 Induced Stresses in the Slab

Intraslab seismic activity has increased north of Padang, offshore of Sumatra, during the years following the 2004 Sumatra-Andaman earthquake. We plot focal mechanisms from intraslab events before and after the 2004 megathrust earthquake in Figure 4.15, selecting events from the GCMT catalog that are at least 10 km below the Hayes and Wald [2009] Sumatra slab interface. Additionally, we identify and remove potentially mislocated interface events by removing mechanisms with an approximately trench parallel nodal plane, dip $< 35°$, and rake between $60 - 120°$. Prior to the 2004 earthquake, a majority of the intraslab activity occurred offshore of southern Sumatra, following the 2000 Enggano earthquake (Figure 4.15a). The 2000 earthquake initiated in the slab and triggered a second subevent on the plate interface [Abercrombie et al., 2003]. There was an especially energetic aftershock sequence following the 2000 earthquake, including both interface and intraslab events, which elevated seismicity levels above the background rate for a period lasting at least four years [in Chapter 2 and Wiseman and Bürgmann [2011]].

Following the 2004 earthquake, intraslab activity increased beneath the 2004 and 2005 rupture zones (Figure 4.15b). Intraslab activity also increased south of the 2005 Nias-Simeulue rupture, in the region east of Siberut. There were six intraslab events in this region below the unreleased Siberut section leading up to the 2009 Padang earthquake, between 2005 and 2008, in comparison to only 4 events between 1976 (the start of the catalog) and 2004.

Static stress changes from the nearby 2005 and 2007 megathrust events enhanced the Coulomb Failure stress (CFS) in portions of the slab below the Siberut segment. We calculate the CFS changes in the slab from the recent megathrust earthquakes, and two nearby backthrust earthquake clusters [in Chapter 3 and Wiseman et al. [2011]], using the preferred Collings elastic structure and the EDGRN/EDCMP programs [Wang et al., 2003]. ΔCFF is defined as the change in shear stress (positive in direction of fault slip) plus the

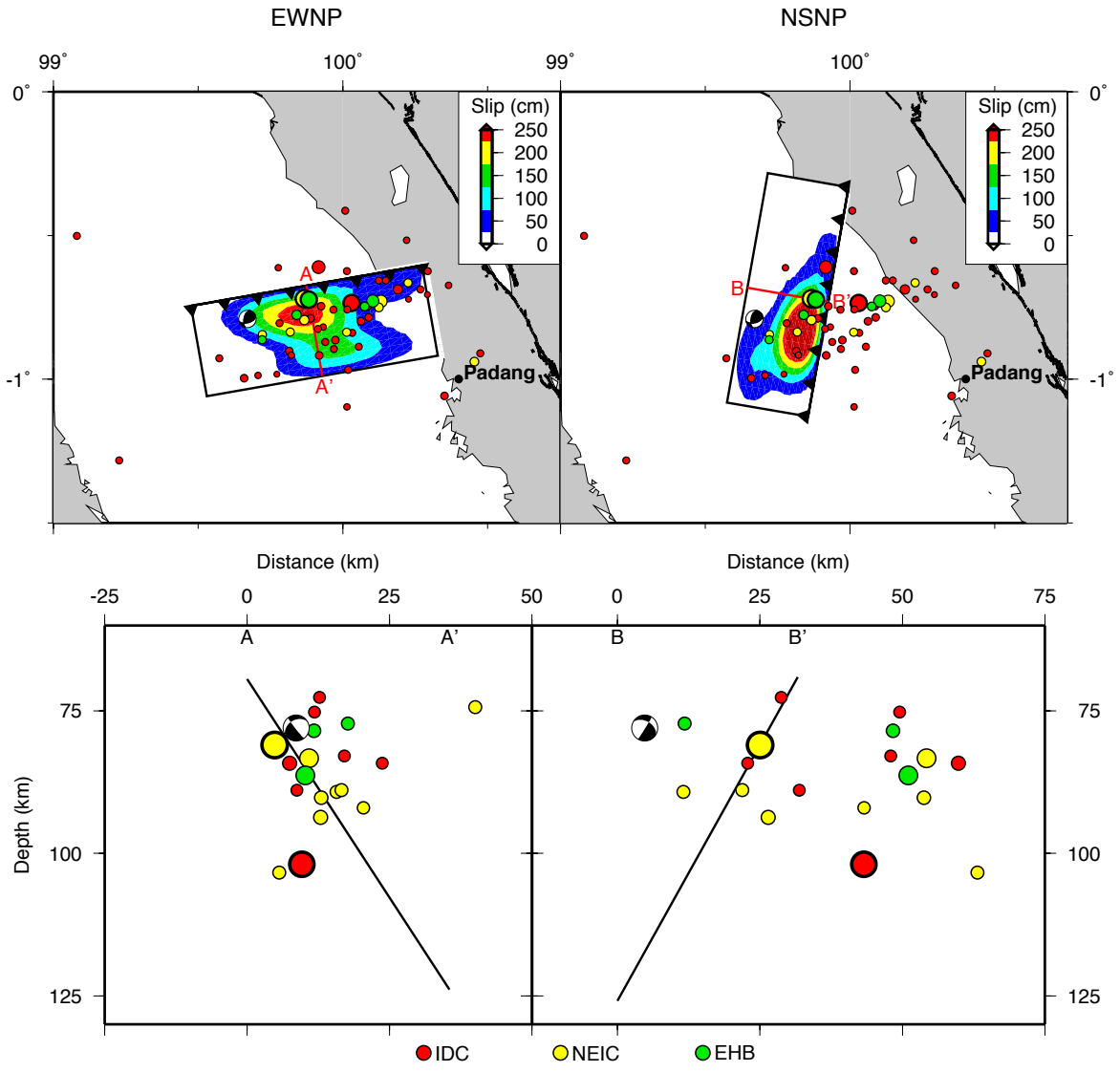

Figure 4.14: One month of aftershock activity following the 2009 mainshock. Aftershocks from three different seismic catalogs are shown: EHB (green), NEIC (blue), and IDC (red). The distributed slip models are shown by color contours on the fault planes projected to the surface. The cross sections restrict the EHB catalog to only those events with accepted depths, and limit the IDC catalog to mb $\geq$4.0 events.

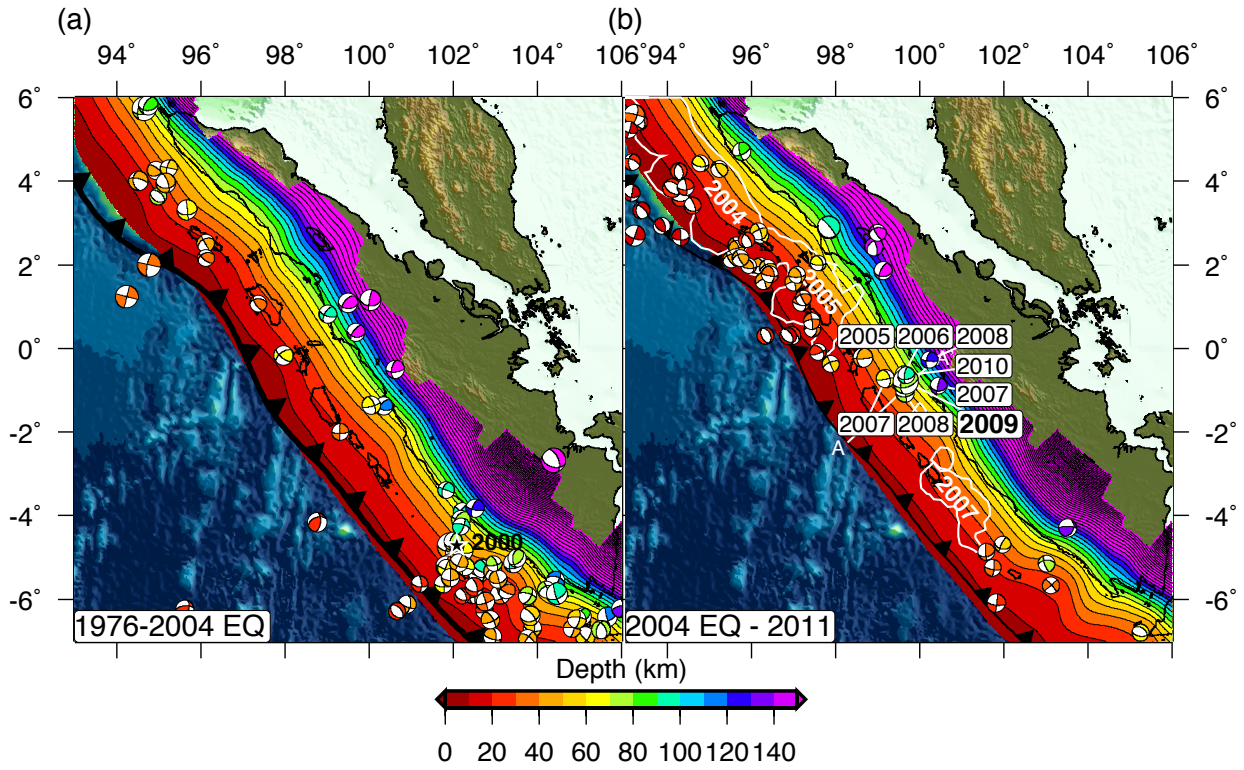

Figure 4.15: Intraslab focal mechanisms colored according to hypocentral depth, beneath the Sunda megathrust, which is also color-coded according to depth [Hayes and Wald, 2009]. (a) 1976 until 2004 M_w 9.2 Sumatra-Andaman earthquake. The location of the 2000 M 7.9 Enggano earthquake is shown with black star. (b) After the 2004 earthquake until May 2011. The rupture zones for the three great earthquakes of 2004, 2005 and 2007 are outlined in white. The years are listed for the events near the 2009 earthquake. All plotted centroids are at least 10 km below the megathrust interface.

Table 4.3: CFS Changes (kPa) at the 2009 Padang earthquake hypocenter due to recent large earthquakes

Fault Geometry	2004 Sumatra-Andaman	2005 Nias-Simeulue	2005 backthrust	2007 M_w 8.4 Bengkulu	2007 M_w 7.9 Bengkulu	2009 backthrust
EWNP	< -1	-1	3	< 1	15	2
NSNP	-1	-3	1	-5	22	1

effective coefficient of friction times the normal stress (unclamping is positive). Toda et al. [2011] found that 6 of the 7 largest, remote, off-megathrust Tohoku aftershocks experienced $\Delta CFF \geq 30$ kPa from the mainshock. Stein [1999] concludes that 10 kPa is the minimum ΔCFS correlated with changes in seismicity rates. We assume an effective coefficient of friction $\mu' = 0.4$, and resolve the stress changes on a profile that extends from the trench to the western coast of Sumatra, through the 2009 hypocenter ($A - A'$ in Figure 4.15b). Out of all the recent megathrust and backthrust earthquakes, the 2007 M_w 7.9 Bengkulu aftershock produced the largest positive CFS increase at the 2009 hypocenter, equal to 15 kPa. The 2007 earthquake produced a broad positive lobe encompassing the 2009 hypocenter, when resolved on the EWNP fault geometry, which also promoted two smaller intraslab events in 2007 and 2008 (Figure 4.16). The other megathrust and backthrust events, even the 2009 backthrust cluster that started just 45 days before the Padang earthquake, produced < 5 kPa at the 2009 hypocenter (Table 4.3).

4.7.2 Induced Stresses on the Megathrust

We next model the stress changes on the megathrust due to the 2009 Padang earthquake to ascertain whether the section of the Sumatra megathrust between the 2005 and 2007 rupture zones, which last ruptured in the great Mentawai earthquake of 1797, was relieved or enhanced. We calculate the shear, normal and CFS change at depth along the Hayes and Wald [2009] slab interface. The slab interface steepens from 3° at 7.5 km depth to 45° at 115 km depth, and we assume a 90° rake and average strike for each depth interval ranging from 314° to 317°. Figure 4.17a shows the CFS change on the megathrust due to slip on the EWNP, assuming an effective friction coefficient $\mu' = 0.4$ (stress changes due to slip on the NSNP are shown in Figure 4.17b). We model a similar stress pattern as the McCloskey et al. [2010] study, with strong stress relaxation over the rupture plane, with surrounding lobes of moderate loading. The stress shadow is large on the megathrust directly over the hypocenter, and peaks at over -1 MPa, a significant proportion of typical earthquake stress drops. The stress shadow continues ∼85 km southwest towards Siberut at over -10 kPa.

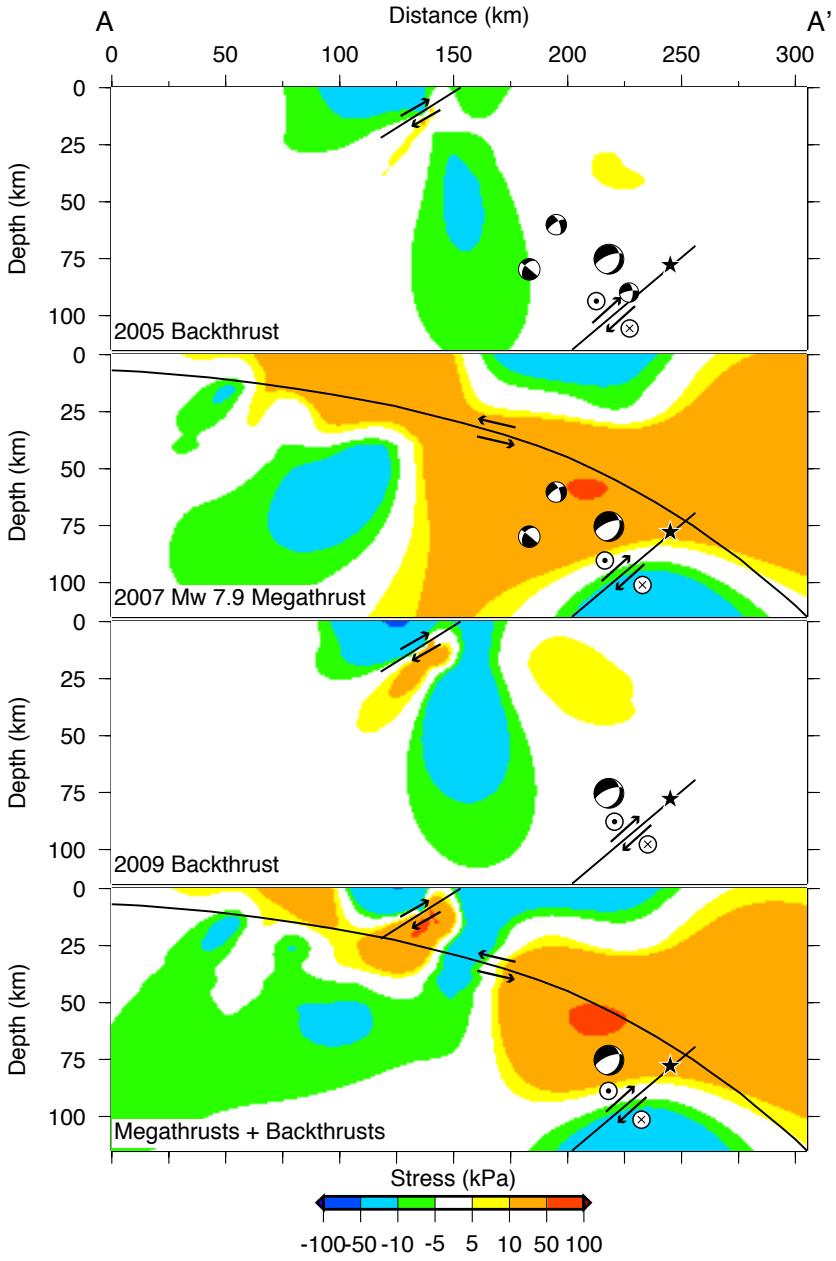

Figure 4.16: Stress changes resolved on the EWNP fault geometry resulting from resulting from (a) the 2005 backthrust cluster [Wiseman et al., 2011], (b) the 2007 M_w 7.9 Bengkulu aftershock [Konca et al., 2008], (c) the 2009 backthrust cluster [Wiseman et al., 2011], and (d) all the recent backthrust and megathrust events (including 2004, 2005, and 2007 megathrust earthquakes). The cross-section is perpendicular to the trench and extends through the 2009 hypocenter (profile $A - A'$ shown on Figure 4.15b). Intraslab earthquake focal mechanisms following each potential triggering event, up to and including the 2009 Padang earthquake, overlay the cross-section. Note the non-linear stress scale.

CFS is enhanced by over 1 MPa directly north of the fault plane. The interface continues to be loaded to the northwest by at least 10 kPa to 40 km depth and south of the rupture plane by at least 10 kPa to 45 km depth. The stress cross-sections show unclamping of the megathrust further updip from the 2009 hypocenter in the seismogenic zone near Siberut, but shear stress and CFS are reduced in this region, as we prevent the intraslab fault from slipping through the megathrust interface.

4.8 Discussion

Our joint analysis of geodetic and seismic waveform data confirms that the Padang earthquake was not caused by rupture of the Sunda megathrust. It initiated in the subducting slab at ∼80 km depth, near the plate interface, and ruptured primarily downdip and to the southwest. The joint modeling does not favor either the N-S or the E-W nodal plane as the source of the earthquake – variance reductions for the two nodal planes are equivalent. Moreover, the synthetic waveforms for each nodal plane are very similar in amplitude, frequency content, and polarities. The NSNP has very slightly lower GPS displacement residuals in the joint inversion (one fewer near-field site falls outside the errors), but this is not a compelling reason to favor the N-S nodal plane. This is a similar situation to the 2001 Nisqually intraslab earthquake models, where inversion of both seismic and geodetic data could not resolve the fault plane ambiguity [Ichinose et al., 2004].

Reinforcing the ambiguity are two other pieces of information. The east-west alignment of aftershocks, and their depth range, favors the east-west rupture, but geological context favors the north-south rupture. The N10°E orientation of NSNP aligns well with the N03°E fabric of fracture zones on the subducting seafloor. NSNP is just east of the most pronounced of these fractures – the Investigator Fracture Zone (Figure 4.1). Fauzi et al. [1996] showed that the subducted portion of the Investigator Fracture Zone near Toba had high levels of seismicity. Several of the other N-S striking structures are active on the seafloor west of the Sunda trench [Deplus et al., 1998]. Moreover, at least one is active within the subducting slab: Left-lateral rupture of a subducted N-S fracture zone initiated the M_w 7.9 Enggano Island earthquake of June 2000 [Abercrombie et al., 2003]. Thus it is quite plausible that the 2009 Padang earthquake was the result of rupture on a north-striking, left-lateral oceanic fracture zone. This hypothesis is supported by the dip of the NSNP. If an oceanic fracture zone has been subducted within the oceanic lithosphere, its dip should be rotated from verticality by an amount associated with the dip of the overlying megathrust. Using the stereonet program OSXStereonet (`http://homepage.mac.com/nfcd/work/programs.html`), We have determined the orientation of the north-striking fractures once they've been subducted to the location of the 2009 earthquake. Above the hypocenter of the 2009 earthquake, the dip of the megathrust is about 32° to the northeast [Hayes and Wald, 2009], and considering the

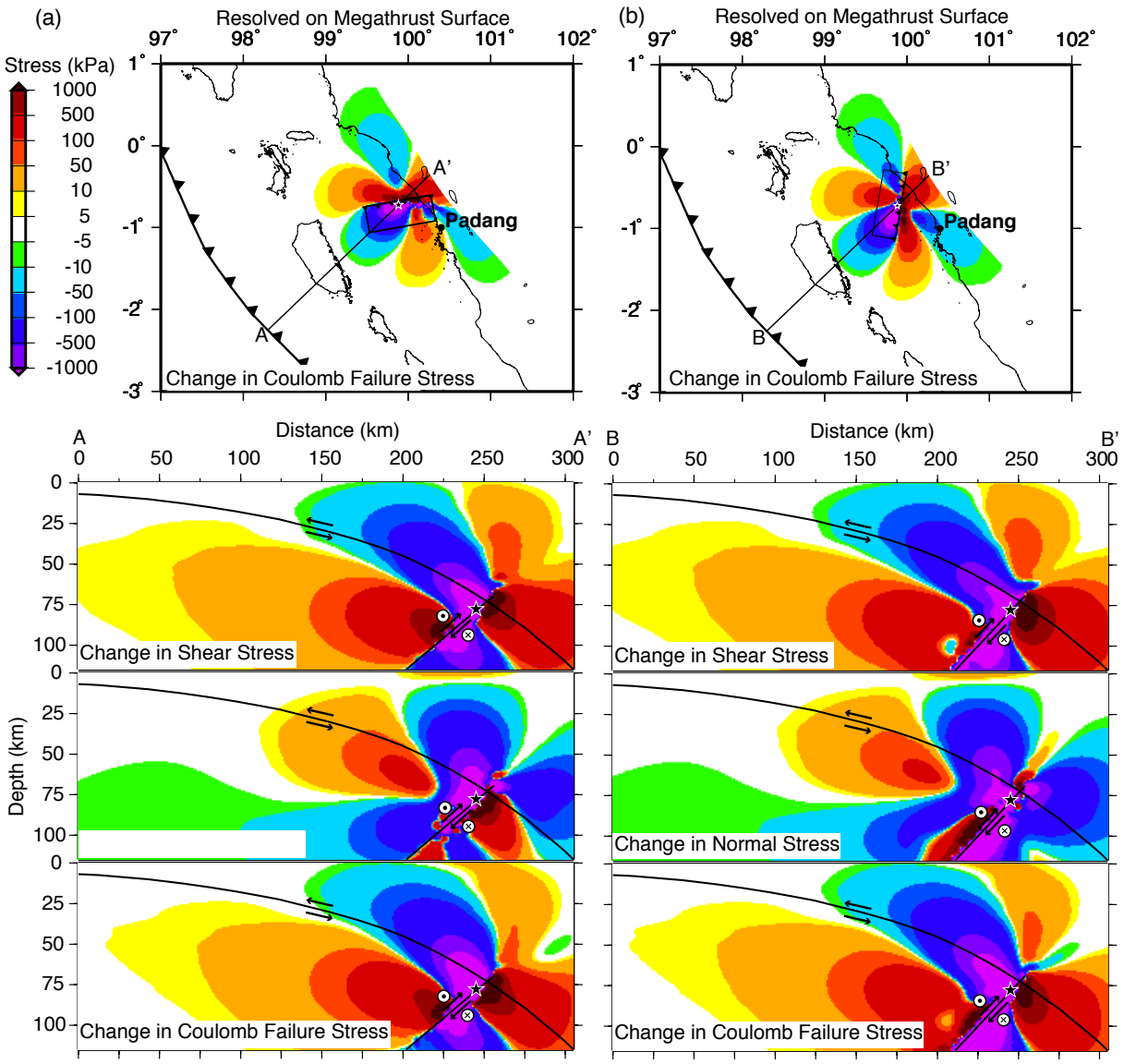

Figure 4.17: Stress changes resulting from slip on the (a) EWNP and (b) NSNP, resolved on the megathrust. The map shows CFS change on the megathrust assuming $\mu' = 0.4$. The cross-sections are perpendicular to the trench and extend through the 2009 hypocenter and show shear stress change, normal stress change, and CFS change. Note the non-linear stress scale.

47° angle between the strike of the megathrust and the N03°E strike of the fracture zones on the ocean floor, the rupture plane beneath the megathrust should strike N08°E and dip 69° west. This is very close to the N10°E strike and 61°W dip of the optimal NSNP.

An alternative hypothesis favoring the EWNP is that the earthquake was caused by rupture of a subducted normal fault associated with the Wharton Ridge fossil spreading centers (gray rectangles on Figure 4.1, from [Deplus et al., 1998]). The fossil spreading centers west of the Sunda trench, are orientated 14° southeast of the EWNP. Assuming that the normal faults initially dip 60°, the subducted fault would strike N71°E with a 40° dip. The optimal EWNP strikes N80°E and dips 57°, thus the reoriented normal faults are not as close of a match to the EWNP as the vertical fractures are to the NSNP.

We mentioned above that the 2009 Padang earthquake is similar to the M_w 7.9 2000 Enggano earthquake, offshore of southern Sumatra. One intriguing aspect of the 2000 earthquake is that it involved two subevents. Abercrombie et al. [2003] concluded from analysis of teleseismic body waves and aftershock mechanisms that the earthquake initiated as a north-south oriented, left-lateral rupture of the downgoing Australian plate but concluded with rupture of an overlying patch of the megathrust. The Padang aftershock sequence is much less energetic than the 2000 sequence and there is no differentiated class of shallower, megathrust aftershocks in the NEIC, IDC or GCMT catalogs to suggest there may have been a subevent on the megathrust. In addition, there are no detectable postseismic transients in the geodetic data following the 2009 earthquake, and therefore no observable triggered aseismic slip on the megathrust. This lack of postseismic afterslip on the megathrust suggests that the interface is still strongly coupled deeper than 55 km, where there was > 0.1 MPa stress increase north of the rupture plane.

The Siberut section of the Sunda megathrust has had a complex stress evolution over the past 8 years. The 2004 and 2005 megathrust earthquakes enhanced CFS above 10 kPa until the southern end of the Batu Islands (Figure 4.18a). The two backthrust clusters in 2005 and 2009 decreased CFS on the shallow portion of the megathrust, surrounding Siberut, but increased CFS on the deeper section (Figure 4.18b). The 2007 Bengkulu earthquakes greatly enhanced CFS on the section of the megathrust that didn't rupture between the M_w 8.4 and M_w 7.9 earthquakes, and also remained above 10 kPa between central Siberut and western Sumatra (Figure 4.18c). When adding the contribution of the 2009 Padang earthquake to the stress field, the Siberut segment has experienced > 10 kPa coseismic CFS change over a majority of the segment over the past 8 years (Figure 4.18d). Chlieh et al. [2008] inverts geodetic data to determine interseismic coupling along the megathrust and determines that the megathrust is poorly coupled beneath the Batu Islands, which can explain the southern boundary of the 2005 Nias-Simeulue earthquake. However, the megathrust appears to be strongly coupled beneath Siberut, Sipora and Pagai Islands until at least 50 km depth. In addition, more slip deficit has accumulated near Siberut since 1797 than the maximum co-

seismic slip estimates for the 1797 event [Chlieh et al., 2008; Konca et al., 2008]. Therefore the Siberut segment, which paleoseismic data suggest is overdue for another great earthquake, and has been pushed closer to failure from all directions during the past 8 years, appears to have the highest seismic hazard in the region.

4.9 Conclusions

Our seismic waveform and geodetic analysis shows that the Padang earthquake initiated in the subducting slab and extended downdip of the hypocenter to the southwest, although the analysis can not determine which nodal plane was the rupture surface. The aftershock catalogs align better with the strike of the east-west plane, which may be the most conclusive evidence available. Both nodal planes align with prominent bathymetric features: the north-south plane with the strike-slip faults near the Investigator Fracture Zone, and to a lesser degree, the east-west plane with Wharton Ridge and associated normal faults. The Padang earthquake is the second largest intraslab earthquake in the Sunda subduction zone recorded in the GCMT catalog, behind the 2000 Enggano earthquake. Intraslab activity increased below the Siberut segment of the megathrust during the years following the 2004 Sumatra-Andaman earthquake, with eight events producing oblique focal mechanisms between 2005-2010. The 2009 Padang earthquake has variably stressed the deepest portion of the coupled megathrust, encouraging rupture northwest and south of the 2009 fault plane and discouraging rupture directly over and to the southwest of the fault plane. This Siberut section of the megathrust last participated in a major rupture either in 1797 or about a century earlier and appears from paleoseismic evidence to be poised for another great rupture. The 2009 earthquake may encourage the next Sumatran megathrust event to initiate in the northern portion of the historic 1797 rupture, south of the 2005 Nias rupture and just north of Siberut.

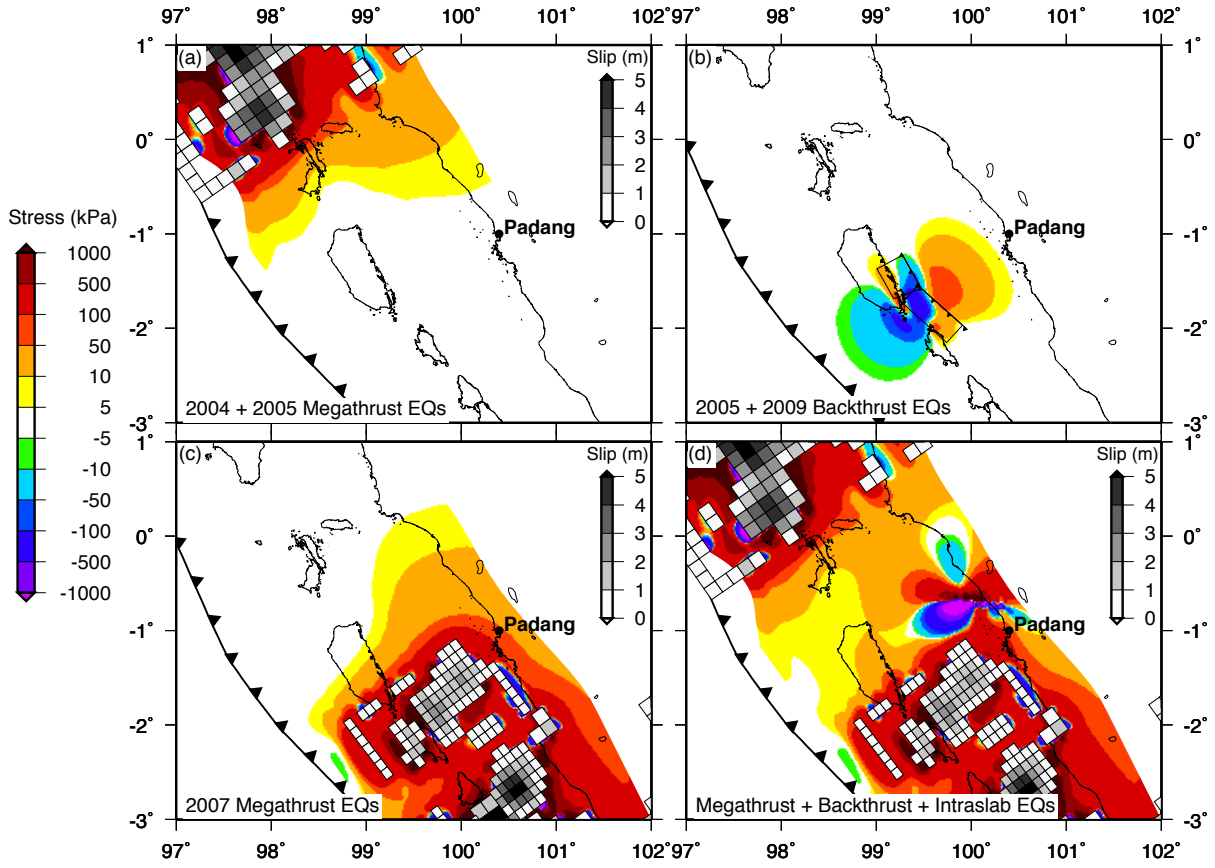

Figure 4.18: Stress changes resolved on the megathrust resulting from (a) the combined 2004 M_w 9.2 [Chlieh et al., 2007] and 2005 M_w 8.7 [Konca et al., 2007] megathrust earthquakes, (b) the combined 2005 and 2009 M_w 6.7 backthrust earthquakes [Wiseman et al., 2011], (c) the combined 2007 M_w 8.4 and M_w 7.9 earthquakes (Konca et al. 2008), and (d) all of the events in a-c and the 2009 M_w 7.6 intraslab earthquake. The map shows CFS change on the megathrust assuming $\mu' = 0.4$. The slip models for the megathrust events overly the stress changes, signifying the portions of the megathrust with large coseismic stress drop. Note the non-linear stress scale.

Chapter 5

Stress Triggering of the Great Indian Ocean Strike-slip Earthquakes in a Diffuse Plate Boundary Zone

5.1 Abstract

On April 11, 2012, two great magnitude 8+ earthquakes occurred within a two-hour period off the west coast of northern Sumatra, Indonesia, in the broadly distributed India-Australia plate boundary zone. The magnitude 8.6 mainshock holds the distinction of being both the largest instrumentally recorded strike-slip earthquake and the largest earthquake away from a recognized plate boundary fault. The mainshock involved sequential ruptures of multiple fault planes oriented nearly perpendicular to each other. The adjacent 2004 megathrust earthquake statically loaded the northern Wharton Basin oceanic lithosphere on both of the 2012 mainshock fault plane orientations, and greatly enhanced the rate of earthquake activity in the region for a year. Viscoelastic relaxation of the asthenosphere following the 2004 and 2005 megathrust earthquakes continued to positively stress the offshore region, correlating with the locations of later strike-slip earthquakes, including two magnitude 7+ and the 2012 magnitude 8+ earthquakes.

5.2 Introduction

Plate tectonic theory assumes that the lithosphere is strong and rigid and that seismicity is mostly restricted to narrow plate boundaries. However, in the equatorial region of the Indian Ocean, the location of the M_w 8.6 and M_w 8.2 strike-slip earthquakes on April 11, 2012, the lithosphere is actively deforming in a broad zone between the rigid Indian and Australian plates (green shaded region in Figure 5.1). Seismic and geodetic data suggest that the deformation style changes from north-south shortening west of the Ninety East Ridge [Delescluse and Chamot-Rooke, 2007; Deplus, 2001] to left-lateral shear in the Wharton Basin east of the Ninety East Ridge [Delescluse and Chamot-Rooke, 2007; Deplus, 2001;

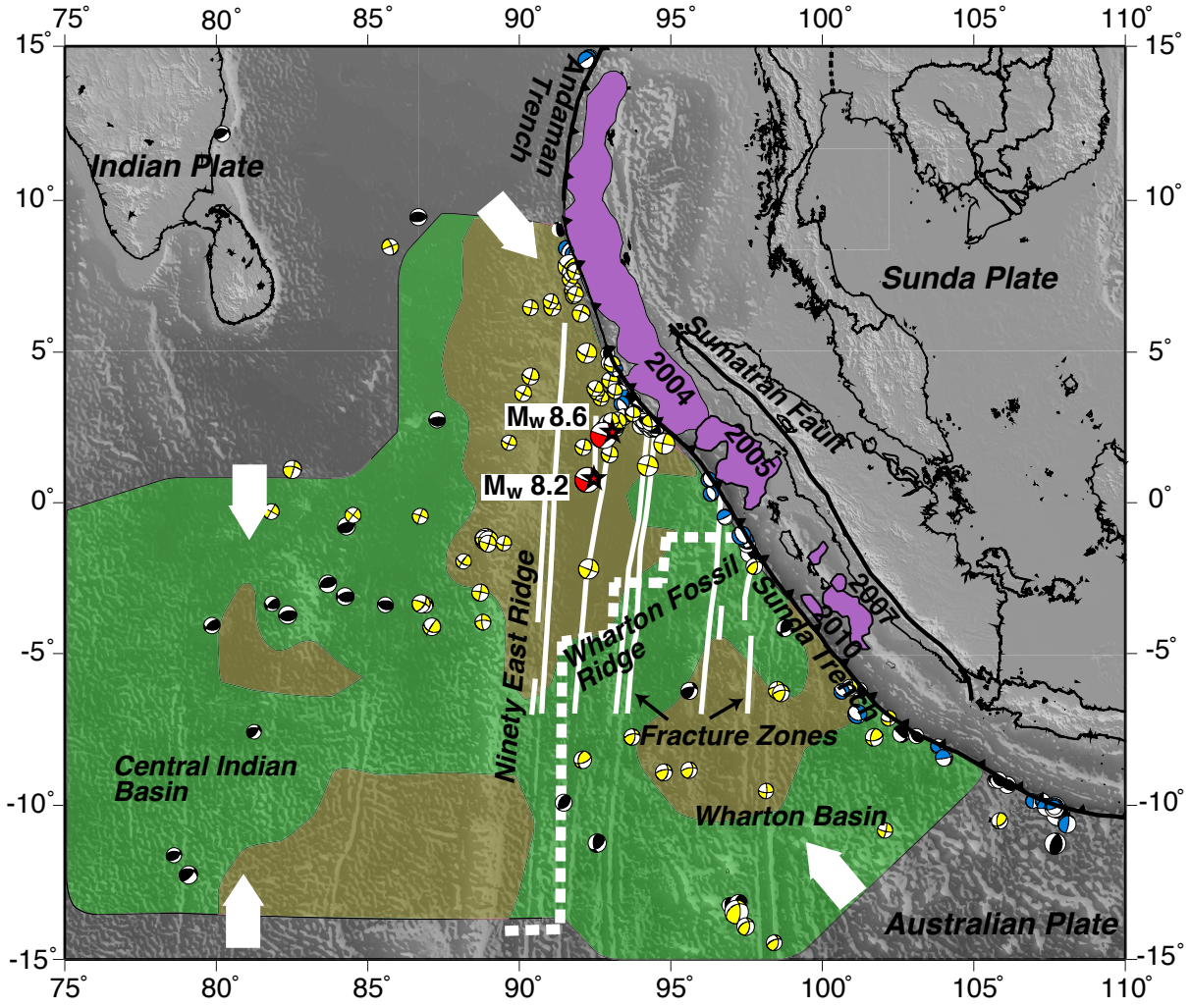

Figure 5.1: Tectonic overview of the India-Australia Plate. The diffuse boundary between the Indian and Australian plates is shaded green [Delescluse and Chamot-Rooke, 2007] and overlays the bathymetry. The overlapping regions with anomalously high lithospheric temperatures are shaded brown [Shapiro et al., 2008]. Fractures and ridges within Wharton Basin are from Shapiro et al. [2008]; Singh et al. [2011a]. All of the focal mechanisms for earthquakes in the India-Australia plate west of the Andaman-Sunda-Java Trench from 1976 until the 2012 mainshock (Global CMT catalog) are shown; strike-slip events are colored yellow, reverse events are colored black, and normal events are colored blue. The white arrows illustrate the orientations of maximum compression in the Central Indian Basin and Wharton Basin. Rupture patches for recent megathrust earthquakes are colored purple [Chlieh et al., 2007; Hill et al., 2012; Konca et al., 2008, 2007].

Deplus et al., 1998] (Figure 5.1). Much of the diffuse boundary zone has an anomalously warm mantle, with temperatures above 800°C at 50 km depth (brown shaded regions in Figure 5.1) [Shapiro et al., 2008]. In addition, the oceanic lithosphere is at its thinnest point out of the entire Andaman-Sunda-Java trench system as it approaches northern Sumatra [Shapiro et al., 2008]. The highest seismic strain-rates in the Indian Ocean are located in the northern Wharton Basin, where the thermally young, thin oceanic lithosphere is shearing along a network of NNE-SSW oriented fracture zones. These fractures are remnants from a fossil spreading ridge system and have accommodated at least 100 km of shear since the beginning of intraplate deformation eight million years ago [Delescluse and Chamot-Rooke, 2007]. A deep seismic reflection profile ∼100 km north of the mainshock epicenter has imaged shallow offset sediments near these NNE-SSW structures, indicating that these fractures are still actively shearing [Singh et al., 2011a]. Sager et al. [2010] has observed roughly E-W oriented canyons and troughs along the northern Ninety East Ridge using gravity gradient data, indicative of past spreading accommodated by normal faulting. Seismic profiles along the Ninety East Ridge demonstrate that the faults were active when the ridge formed, and some of the faults penetrate the entire sediment column, evidence of active faulting.

5.3 Seismicity in the Northern Wharton Basin

The style of seismicity in the northern Wharton Basin, between the Ninety East Ridge and the Sunda Trench, is dominated by strike-slip mechanisms, which accommodate the ongoing left-lateral shear in the diffuse plate boundary zone. The yellow beach balls in Figure 5.1 (`www.globalcmt.org`) depict the focal mechanisms for all of the strike-slip earthquakes in the incoming Indian and Australian plates, west of the Andaman-Sunda-Java Trench, from the start of the Global CMT catalog in 1976 until the April 2012 earthquakes. The mechanisms are very similar to the focal mechanisms for the two April, 2012 earthquakes (shown in red), and are consistent with either left-lateral strike-slip motion on the NNE-SSW oriented fractures, or right-lateral motion on WNW-ESE oriented planes.

The 2004 M_w 9.2 Sumatra-Andaman megathrust earthquake [Shearer and Bürgmann, 2010] fundamentally changed the stress state in the surrounding lithosphere and seismicity rates have been enhanced throughout Southeast Asia in the years following the great earthquake (in Chapter 2 and Wiseman and Bürgmann [2011]). The megathrust plate-interface has been especially active south of the 2004 rupture, including a M_w 8.7 earthquake in 2005 that was stress triggered by the 2004 earthquake [McCloskey et al., 2005; Nalbant et al., 2005] and a M_w 8.4 earthquake in 2007. There has also been enhanced seismicity throughout the rest of the subduction zone: in the overriding Sunda plate (in Chapter 3 and Wiseman et al. [2011]), in the Andaman back-arc region [Cattin et al., 2009; Sevilgen et al., 2012], in the downgoing slab - including the 2009 M_w 7.6 Padang earthquake (in Chapter 4 and Wiseman

et al. [2012], McCloskey et al. [2010]), and in the incoming Indian and Australian plates (Figure 5.2).

The seismicity rate in the northern Wharton Basin increased dramatically following the 2004 earthquake. Figure 5.2 shows the cumulative number of magnitude greater than 4.5 earthquakes, the magnitude of completeness for the time period 1980-2012 (ISC and NEIC catalogs). The increased seismicity rate following the 2004 earthquake decays back to the background level within a year, but spikes again in 2010 and early 2012 following magnitude 7+ strike-slip earthquakes.

5.4 The April 11 2012 Ruptures

The 2012 mainshock initiated at 20 km depth and the aftershock pattern (gray circles in Figure 5.3a, USGS NEIC catalog), along with several preliminary back-projection rupture propagation models [Meng et al., 2012; Satriano et al., 2012; Yue et al., 2012] suggests complex rupture on multiple fault planes. It appears that the mainshock started with bilateral propagation away from the hypocenter on an WNW-ESE oriented plane (red fault segment in Figure 5.3a) and then bilaterally ruptured a NNE-SSW oriented plane to the west of the hypocenter (yellow segment labeled 2). It ended with slip on two additional WNW-ESE oriented segments to the south, near the eventual magnitude 8.2 aftershock (yellow segments labeled 3 and 4) [Meng et al., 2012]. The second rupture segment is consistent with left-lateral faulting on one of the roughly N-S oriented fractures within the Wharton Basin. The fourth rupture segment appears to have reactivated one of the roughly E-W oriented faults along the Ninety East Ridge [Sager et al., 2010], and the first and third fault segments suggest similar structural features extend into the Wharton Basin.

Yue et al. [2012] resolved the spatial distribution of slip on the multiple fault segments using finite fault inversions, with geometry constrained by back-projections of short- and long-period seismic energy. They found that the largest moment release was on the initial WNW-ESE segment, with a peak slip of $\sim$37 m [Yue et al., 2012]. The first three segments also contained between $\sim$5-20 m of deep slip, below the hypocenter, extending to the fault plane boundaries at 50 km depth. This helps to explain the 40 km centroid depth (Global CMT and USGS CMT), the best point source location for the rupture, which was 20 km deeper than the hypocenter - where the earthquake initiated. McGuire and Beroza [2012] argue that the deeper slip would require a failure mode other than typical frictional failure, and suggest highly localized zones of viscous failure in the upper oceanic mantle.

The 2012 mainshock was able to grow to such a large magnitude because it was able to continue rupturing beyond the initial WNW-ESE fault plane, on multiple nearby faults

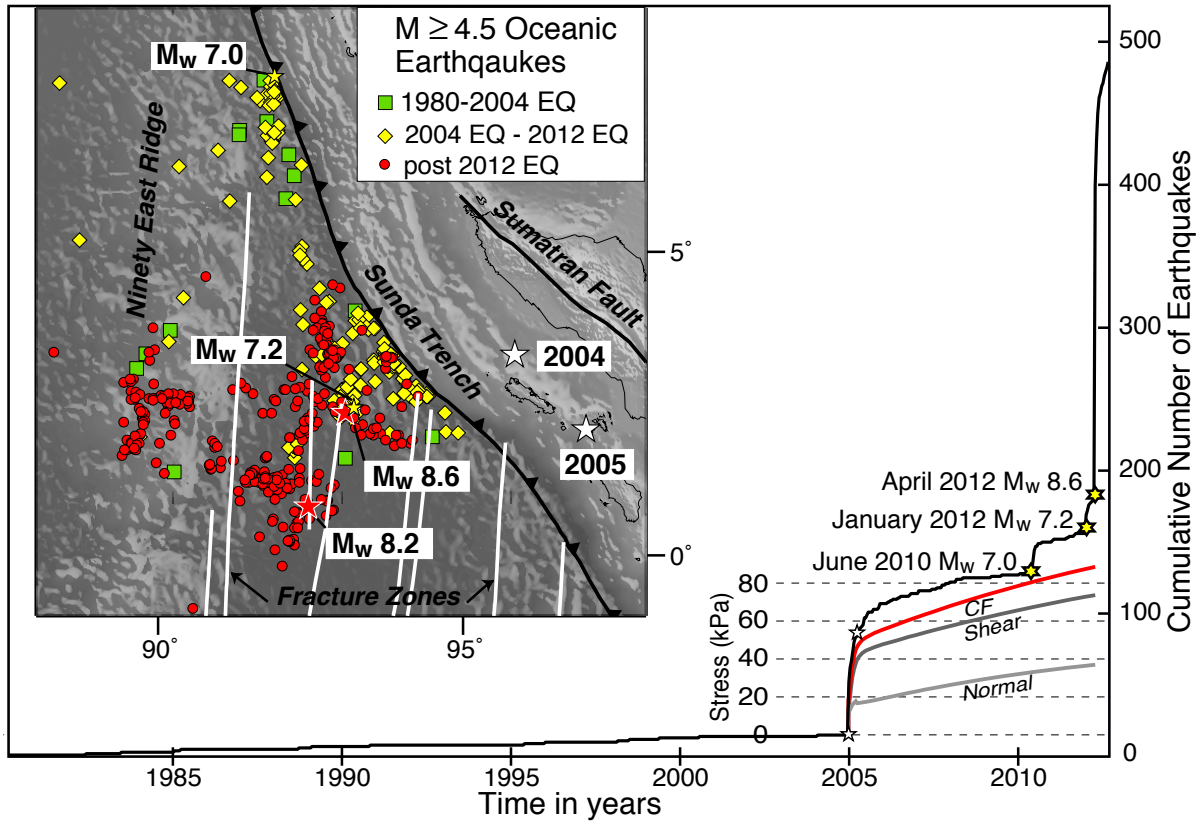

Figure 5.2: Northern Wharton Basin seismicity. The cumulative number of magnitude greater than 4.5 earthquakes (ISC and NEIC catalogs) in the northern Wharton Basin, west of the Sunda Trench, from 1980 until September 10, 2012 is plotted in black. The yellow stars mark large earthquakes within the catalog region that initiated seismicity rate increases, and the 2004 and 2005 megathrust earthquakes (not in the region) are marked with white stars. The epicentral locations of the events are shown in the map inset. The cumulative coseismic and postseismic stress changes from the 2004 and 2005 earthquakes [Chlieh et al., 2007; Konca et al., 2007], resolved on the initial WNW-ESE fault plane orientation at the 2012 hypocenter are plotted in red and gray (see Figure 5.12 for longer stress time series)

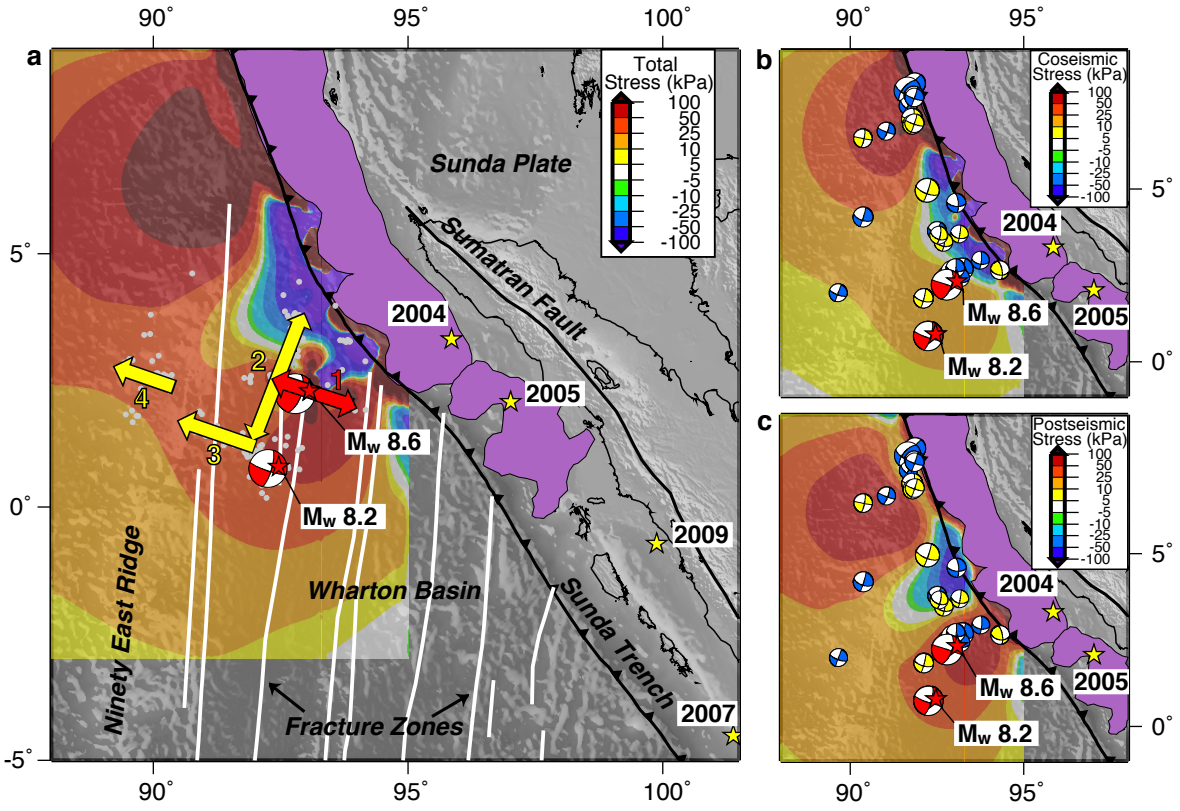

Figure 5.3: Recent stress changes in the Indian Ocean. (a) Total stresses induced by the 2004 [Chlieh et al., 2007], 2005 [Konca et al., 2007], and January M_w 7.2 [`http://earthquake.usgs.gov/earthquakes/eqinthenews/2012/usc0007ir5/finite_fault.php`] earthquakes, resolved at the 20 km hypocentral depth of the mainshock on the orientation of the initial WNW-ESE (red) fault plane [Meng et al., 2012]. Gray circles mark the first 12 days of the aftershock sequence (NEIC catalog). (b) Coseismic stresses induced by the 2004 and 2005 earthquakes. The yellow focal mechanisms highlight the strike-slip earthquakes during the first year following the 2004 earthquake and the blue focal mechanisms depict the remaining events before the 2012 mainshock (Global CMT catalog). (c) Cumulative postseismic stresses induced by the 2004 and 2005 earthquakes at the time of the 2012 mainshock.

in the weak, heavily fractured northern Wharton Basin. This complex rupture scenario is similar to the second largest Wharton Basin earthquake, a M_w 7.9 earthquake in June 2000, which started as left-lateral strike-slip motion on a N-S plane and ended as oblique motion on an E-W plane [Abercrombie et al., 2003]. Several of the focal mechanisms for the first month of 2012 aftershocks show oblique-to-reverse motion, indicating that the M_w 8.6 earthquake may have included an oblique sub-event as well (Figure 5.4). Although the orientation of maximum compression in the Wharton Basin would accommodate NE-SW oriented reverse faulting, reverse mechanisms are not common, likely because it is easier to reactivate the pre-existing faults and fracture zones.

5.5 Stress Changes Induced by the Megathrust Earthquakes

We have calculated the stresses induced by the 2004 and 2005 megathrust earthquakes at the hypocenter of the M_w 8.6 earthquake in order to determine if the 2012 earthquakes were triggered events. We modeled the static, coseismic stress perturbations from the two nearby megathrust ruptures, using source models determined from the inversion of geodetic data [Chlieh et al., 2007] and the joint inversion of seismic and geodetic data [Konca et al., 2007]. The elastic coseismic deformation is calculated in a layered half-space using the EDGRN/EDCMP [Wang et al., 2003] programs and a 1-D velocity structure representing the Sumatran forearc [Collings et al., 2012]. The deformation calculations are used as input to model the Coulomb failure stress (CFS) changes on the orientation of the oceanic strike-slip earthquakes. ΔCFS is defined as the change in shear stress (positive in direction of fault slip) plus the effective coefficient of friction times the normal stress (unclamping is positive). We assume an effective coefficient of friction $\mu' = 0.4$, and determine the CFS changes on constant depth sections in the 2012 epicentral region. We resolve the stress changes on both of the nodal plane orientations associated with the 2012 mainshock.

The 2004 earthquake contributed most of the stress changes at the 2012 hypocenter and further to the north spanning the zone of enhanced strike-slip activity (Figure 5.3b,c). The combined coseismic stress perturbation from the 2004 and 2005 earthquakes was $\sim$18 kPa at the hypocenter (Figure 5.3b), with similar values when resolving stress on either the WNW-ESW or NNE-SSW fault plane orientation (Figure 5.5).

The positive stress lobe near the hypocenter is a robust feature. We compare our preferred coseismic stress model, based on the smoothed, higher resolution Chlieh et al. [2007] and Konca et al. [2007] megathrust source models that consider both seismic and geodetic data sets, with the less discretized, geodetically based Banerjee et al. [2007] source mod-

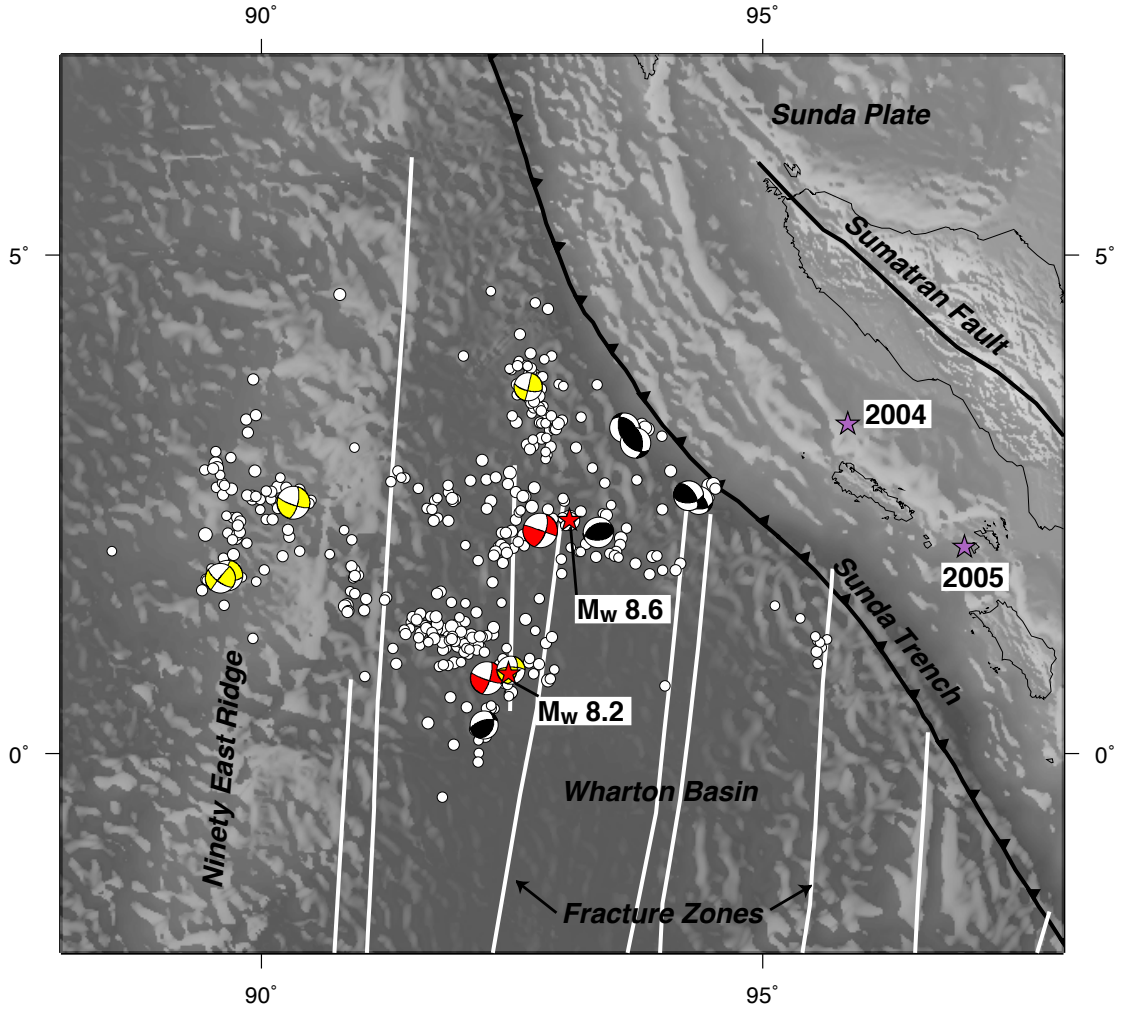

Figure 5.4: One month of seismic activity following the 2012 mainshock. The epicenters for the first month of the seismic activity in the Wharton Basin following the 2012 mainshock are marked with white circles (USGS NEIC catalog). The red-and-white beach balls depict the focal mechanisms for the two 2012 magnitude 8+ earthquakes. The yellow focal mechanisms represent the strike-slip earthquakes during the first month following the 8+ earthquakes and the black focal mechanisms represent the oblique-to-reverse earthquakes during the same period (`www.globalcmt.org`). The NW striking reverse mechanisms near the trench are likely intraplate events associated with the bending incoming slab. The fracture zones are from Singh et al. [2011a].

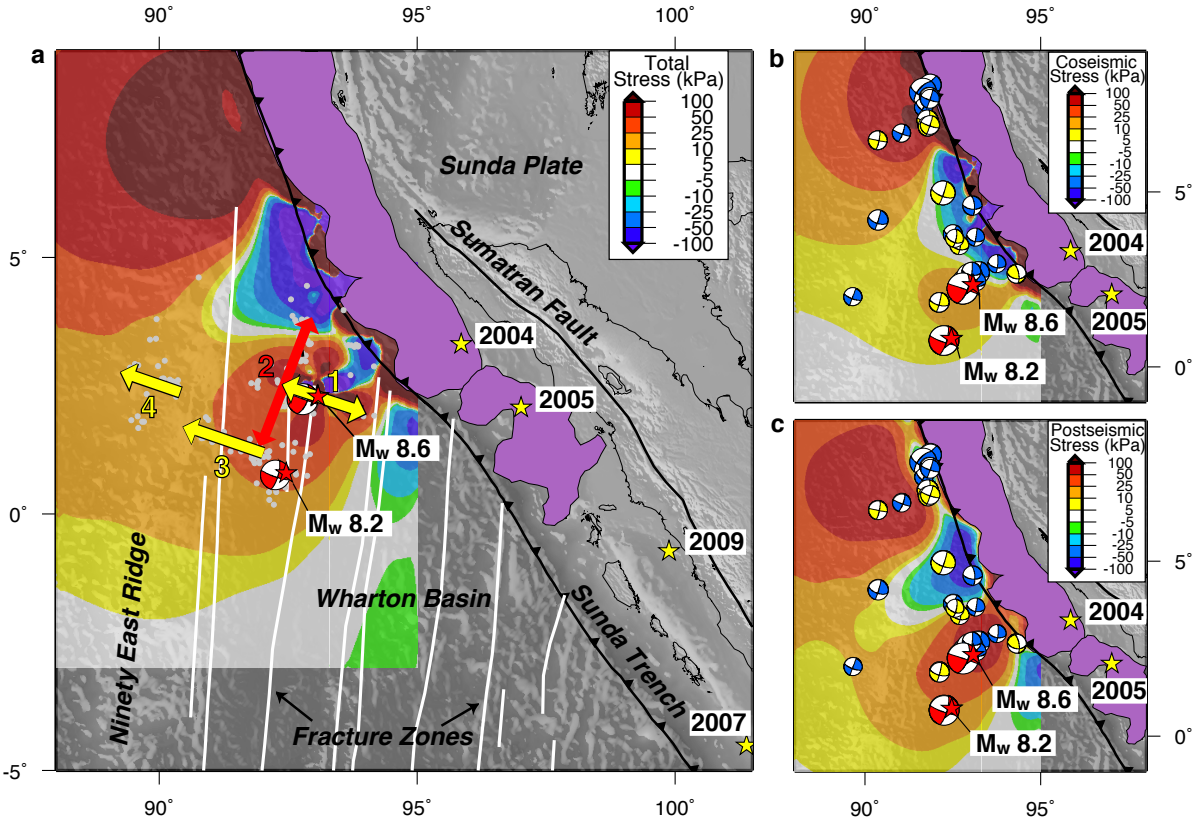

Figure 5.5: Recent stress changes in the Indian Ocean resolved on the NNE-SSW plane. The focal mechanisms, aftershocks, and geologic structures are the same as in Figure 5.3. (a) Total stresses induced by the 2004 [Chlieh et al., 2007], 2005 [Konca et al., 2007], and January M_w 7.2 [`http://earthquake.usgs.gov/earthquakes/eqinthenews/2012/usc0007ir5/finite_fault.php`] earthquakes, resolved at the 20 km hypocentral depth of the mainshock on the orientation of the initial NNE-SSW (red) fault plane [Meng et al., 2012]. (b) Coseismic stresses induced by the 2004 and 2005 earthquakes. (c) Cumulative postseismic stresses induced by the 2004 and 2005 earthquakes at the time of the 2012 mainshock.

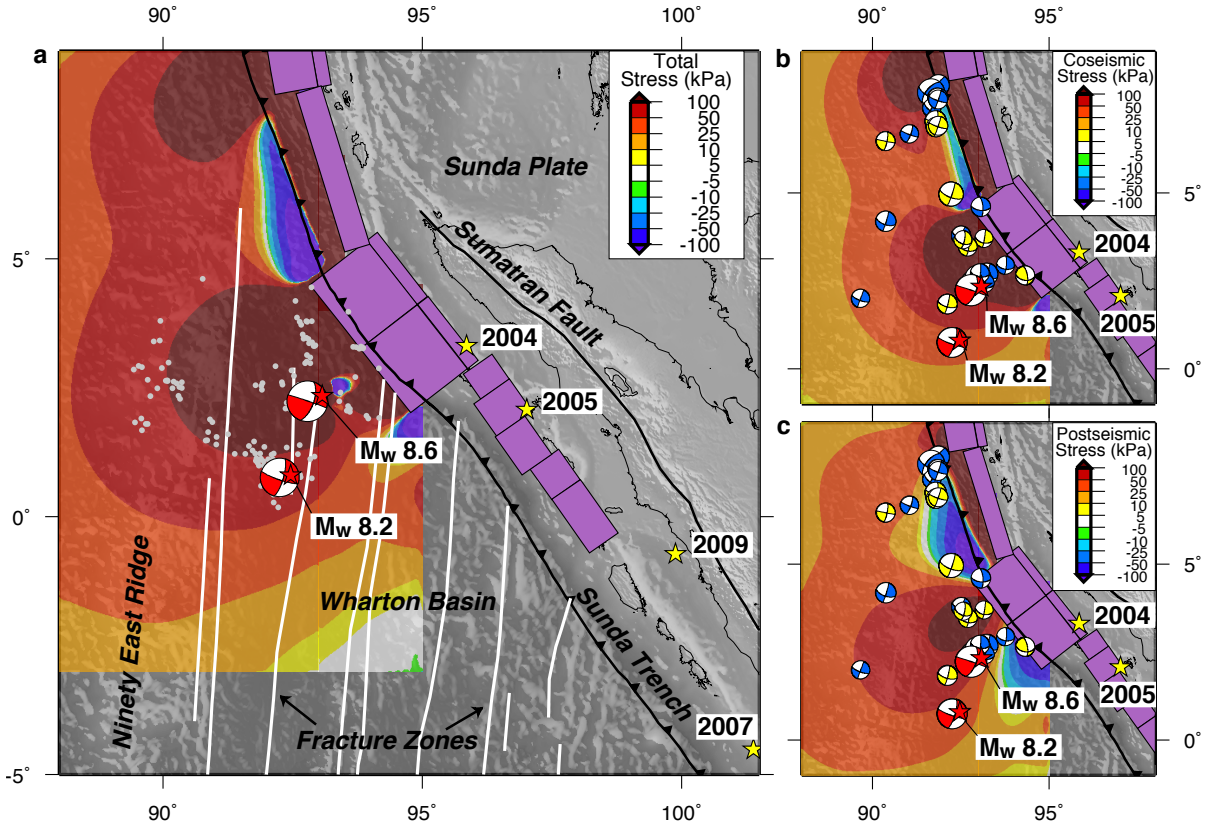

Figure 5.6: Recent stress changes in the Indian Ocean using alternate megathrust slip models resolved on the WNW-ESE plane. Coulomb failure stresses are calculated using alternate coseismic slip models for the 2004 and 2005 earthquakes after Banerjee et al. [2007]. The focal mechanisms, aftershocks, and geologic structures are the same as in Figure 5.3. (a) Total stresses induced by the 2004 and 2005 megathrust earthquakes (purple regions) plus the 2012 foreshock resolved at the 20 km hypocentral depth of the M_w 8.6 earthquake on the orientation of the WNW-ESE fault plane (red fault plane). (b) Coseismic stresses induced by the 2004 and 2005 earthquakes. (c) Cumulative postseismic stresses induced by the 2004 and 2005 earthquakes at the time of the 2012 mainshock.

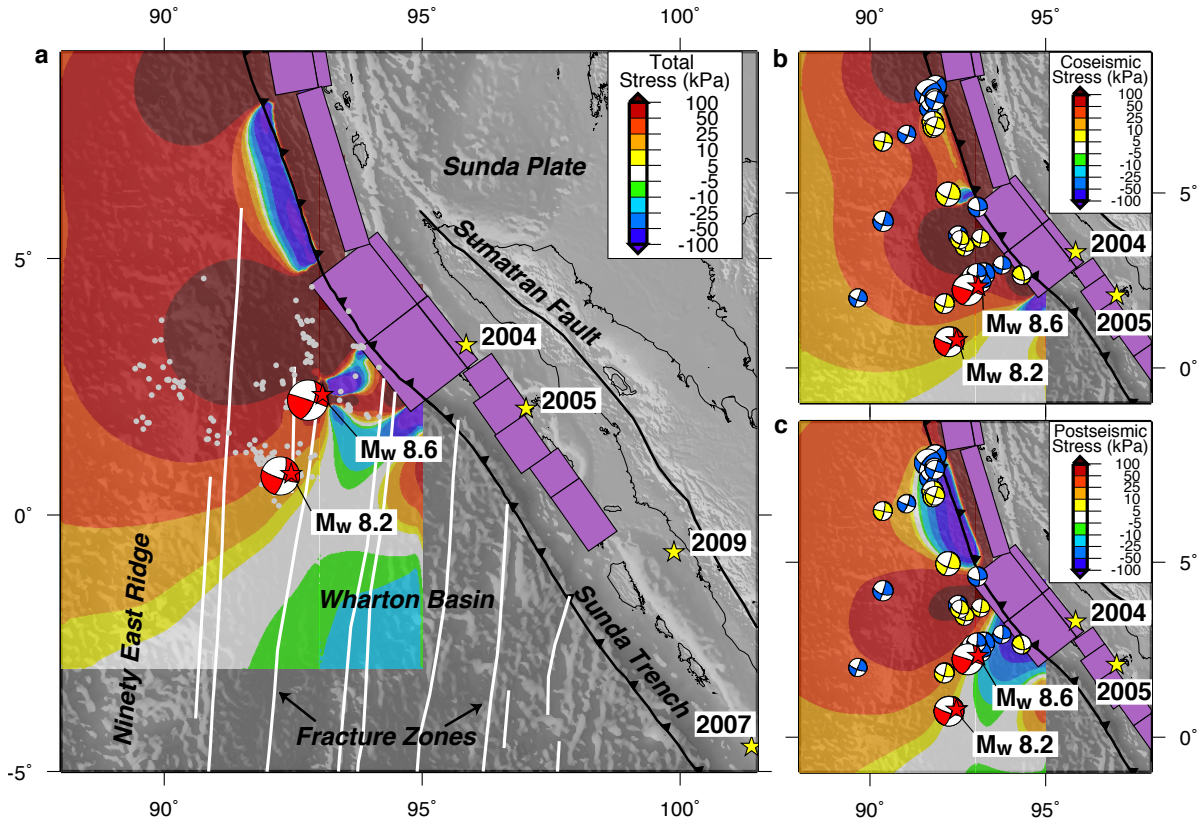

Figure 5.7: Recent stress changes in the Indian Ocean using alternate megathrust slip models resolved on the NNE-SSW plane. Coulomb failure stresses are calculated using alternate coseismic slip models for the 2004 and 2005 earthquakes after Banerjee et al. [2007]. The focal mechanisms, aftershocks, and geologic structures are the same as in Figure 5.3. (a) Total stresses induced by the 2004 and 2005 megathrust earthquakes (purple regions) plus the 2012 foreshock resolved at the 20 km hypocentral depth of the M_w 8.6 earthquake on the orientation of the NNE-SSW fault plane (red fault plane). (b) Coseismic stresses induced by the 2004 and 2005 earthquakes. (c) Cumulative postseismic stresses induced by the 2004 and 2005 earthquakes at the tim of the 2012 mainshock.

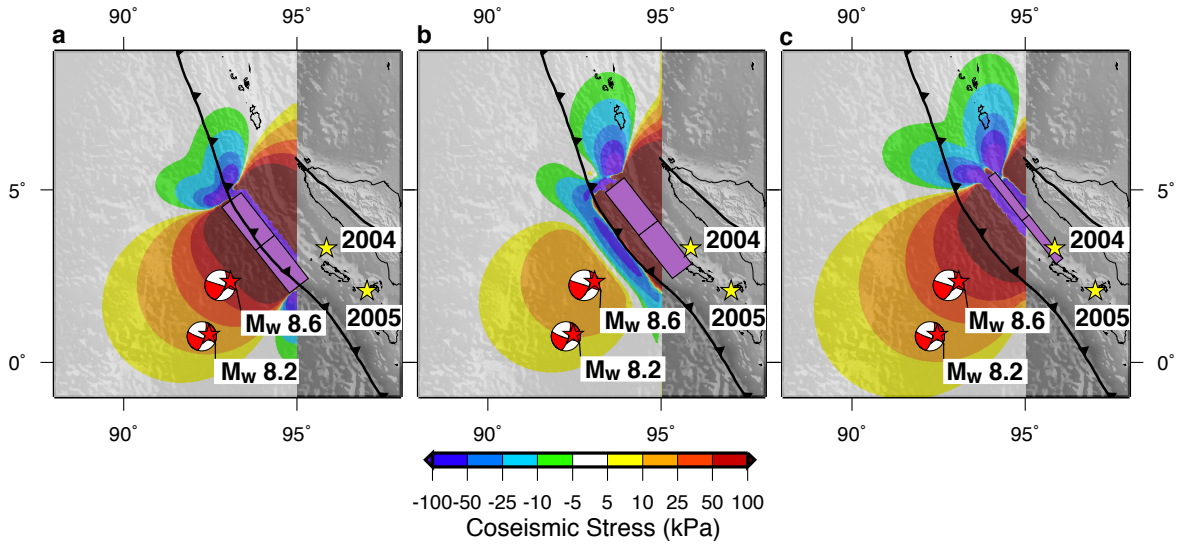

Figure 5.8: The effects of source depth. Stress changes resulting from a uniform 10 m of slip at various source depths (purple regions), using the fault geometry from Banerjee et al. [2007] and resolved on the WNW-ESE plane at 20 km depth. (a) 0-15 km depth, (b) 15-30 km depth, and at 30-50 depth.

els, and the 2012 hypocenter is still positively stressed on both fault orientations (Figures 5.6,5.7). The stress change at the 2012 hypocenter is most sensitive to the amount of slip, and the depth range of slip (Figures 5.8, 5.9), on the southern portion of the 2004 rupture. More shallow slip on the southern portion of the 2004 rupture, as in the Banerjee et al. [2007] model, increases the positive stress change at the 2012 hypocenter and decreases the negative stress region near the trench (Figures 5.6, 5.7, 5.8, 5.9). Lay et al. [2011a,b] have observed that Coulomb stress values in the region near the trench are very sensitive to the amount of shallow slip during the 2011 Tohoku megathrust earthquake. Unfortunately, the geodetic data are more limited for the 2004 Sumatran-Andaman earthquake, and it is not possible to uniquely resolve the amount of shallow slip on the southern segment. There were several strike-slip earthquakes in this sensitive region during the years following the 2004 earthquake that were either positively or negatively stressed depending on the coseismic source model. We also test a range of receiver fault depths from 10 - 40 km and find that the coseismic stress change increases with depth at the epicenter (Figures 5.10, 5.11), and especially in the region northeast of the hypocenter where Yue et al. [2012] model deep slip on both the WNW-ESE and NNE-SSW planes.

We also calculate the time-dependent stress perturbations resulting from postseismic relaxation of the upper mantle following the megathrust events. For the viscoelastic relaxation

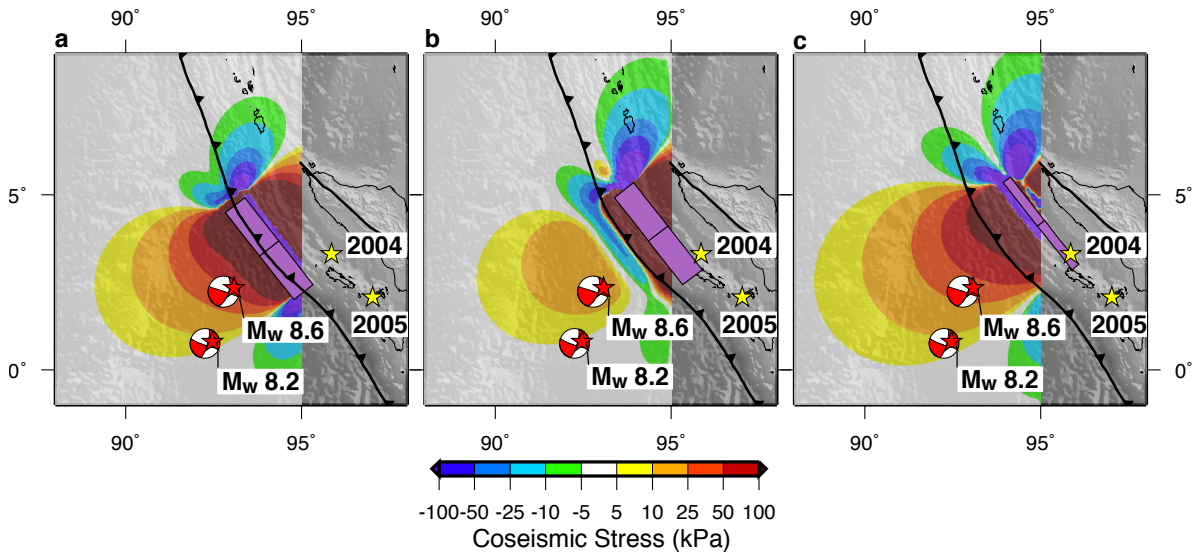

Figure 5.9: The effects of source depth resolved on the NNE-SSW plane. Stress changes resulting from a uniform 10 m of slip at various source depths (purple regions), using the fault geometry from Banerjee et al. [2007] and resolved on the NNE-SSW plane at 20 km depth. (a) 0-15 km depth, (b) 15-30 km depth, and at 30-50 depth.

models, We employ Panet et al. [2010] 1-D rheology model that fits the first ∼3 years of horizontal far-field GPS time-series, and gravity variations recorded by the GRACE satellite, following the 2004 earthquake. This model includes a bi-viscous asthenosphere with an initial short-term viscosity of 4×10^{17} Pa s and a long-term viscosity of 8×10^{18} Pa s.

By April 2012, the postseismic stress perturbation from the megathrust earthquakes was ∼4 times larger than the induced coseismic stresses at the 2012 hypocenter, highlighting the importance of postseismic deformation for triggering earthquakes away from the coseismic rupture plane (see stress time series in Figure 5.2 and Figure 5.3c). These additional stress perturbations can explain the continued strike-slip activity during the years following the 2004 earthquake (blue focal mechanisms in Figure 5.3b,c). This includes events NE of the 2012 hypocenter that experienced negative coseismic stress changes but positive postseismic stress perturbations, and the June 2010 and January 2012 M 7+ events.

The postseismic deformation and associated stress perturbations are likely larger in the northern Wharton Basin than in the surrounding Indian Ocean due to the thinner and warmer lithosphere in this region [Shapiro et al., 2008]. A locally thinner lithosphere in the vicinity of the 2012 earthquakes would allow larger stress transmissions from the closer, flowing asthenosphere, and the warmer mantle would increase the pace of viscous relaxation,

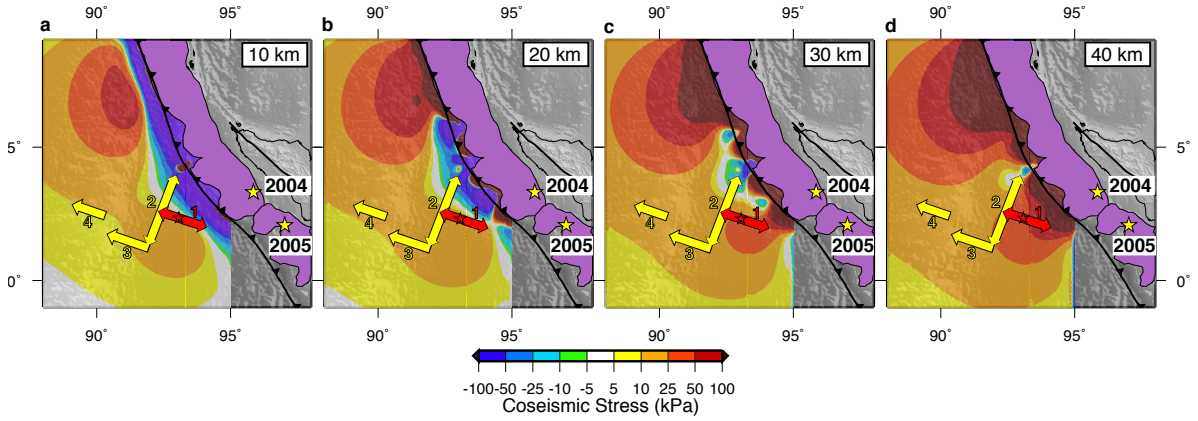

Figure 5.10: The effects of receiver depth resolved on the WNW-ESE plane. Coseismic stress changes resulting from the 2004 [Chlieh et al., 2007] and 2005 [Konca et al., 2007] earthquakes resolved on the WNW-ESE (red) fault plane [Meng et al., 2012] at various receiver depths. (A) 10 km depth, (B) 20 km depth (NEIC mainshock hypocenter depth), (C) 30 km depth, and (D) 40 km depth (centroid depth)

inducing larger stress perturbations by the time of the 2012 earthquake. In addition, a M_w 7.2 earthquake, ∼25 km NE of the mainshock in January 2012, involved right-lateral slip on an E-W oriented fault [`http://earthquake.usgs.gov/earthquakes/eqinthenews/2012/usc0007ir5/finite_fault.php`] and added a final push before the April events.

5.6 Discussion and Conclusions

The high strain rates within the Wharton Basin enable strike-slip earthquakes over a wide portion of the plate interior, and the stresses imparted to the oceanic lithosphere by the 2004 earthquake induced a spike in the rate of these strike-slip earthquakes. Although megathrust ruptures in other tectonic settings would produce similar enhanced stresses along the orientation of the 2012 earthquake, in most cases there would not be enough accumulated strain in the oceanic plate, or pre-existing geologic structures, to enable such a large-magnitude triggered earthquake. For example, there were no triggered strike-slip earthquakes in the interior of the Pacific plate, east of the trench, during the 14 months following 2011 Tohoku earthquake (based on Global CMT catalog). The broad shear zone associated with the diffuse India-Australia plate boundary primed the northern Wharton Basin for strike-slip faulting and the megathrust earthquakes provided the triggering mechanism. The 2012 magnitude 8+ events were the latest in this collection of post-2004 strike-slip earthquakes and the additional stress imparted to the lithosphere from the postseismic deformation can

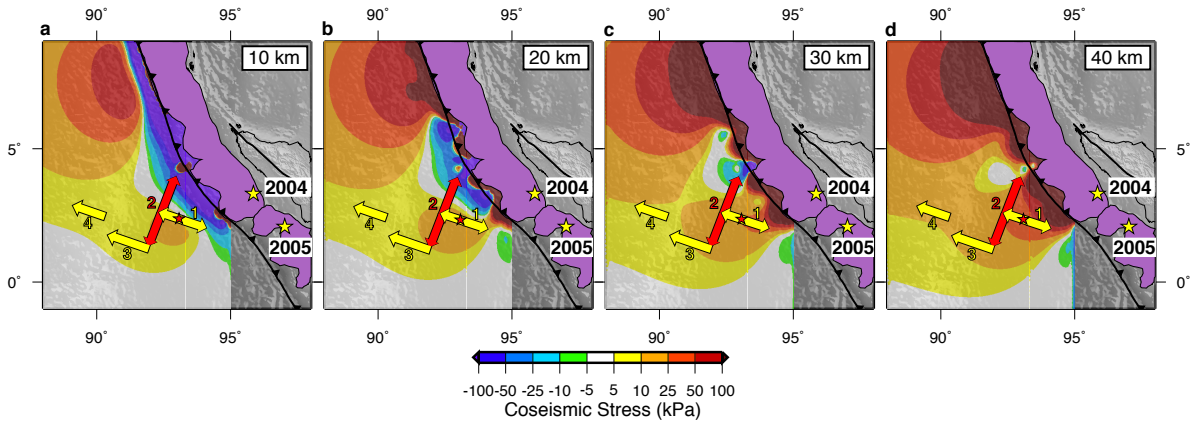

Figure 5.11: The effects of receiver depth resolved on the NNE-SSW plane. Coseismic stress changes resulting from the 2004 [Chlieh et al., 2007] and 2005 [Konca et al., 2007] earthquakes resolved on the NNE-SSW (red) fault plane [Meng et al., 2012] at various receiver depths. (A) 10 km depth, (B) 20 km depth (NEIC mainshock hypocenter depth), (C) 30 km depth, and (D) 40 km depth (centroid depth)

explain the time delay between the 2004 and 2012 earthquakes.

An independent study by Delescluse et al. [2012] also investigates the connection between the 2004 and 2005 megathrust earthquakes and the April 2012 oceanic earthquakes. They use different megathrust source models and simpler modeling approaches - homogeneous elastic half-space for the coseismic stress calculations and 2-D finite-element model with uniform imposed slip for the postseismic stress calculations - but come to similar conclusions. This emphasizes the robustness of the main results that the megathrust earthquakes enhanced seismicity in the northern Wharton Basin, both through static coseismic stress perturbations and through evolving postseismic stress transients.

The 2012 mainshock was so large because it was able to rupture multiple weak spots within the oceanic lithosphere, including four separate fault planes. The annual moment rate for the entire Wharton Basin, that actively deforms down to 20°S, is $\sim 3.5 \times 10^{19}$ Nm/yr [Delescluse and Chamot-Rooke, 2007], and these two magnitude 8+ strike-slip earthquakes released ~270 years of accumulated seismic moment. The northern portion of Wharton Basin is the most rapidly straining region in the diffuse India-Australia boundary zone, accommodating roughly 1 cm/yr of N-S left-lateral shear over the past eight million years, so this region should have shorter earthquake repeat times of order of 500-1000 years, than the rest of the region. Over the past millennia, the megathrust earthquake periodicity for the southern end of the 2004 rupture has been roughly 400-600 years [Meltzner et al., 2010],

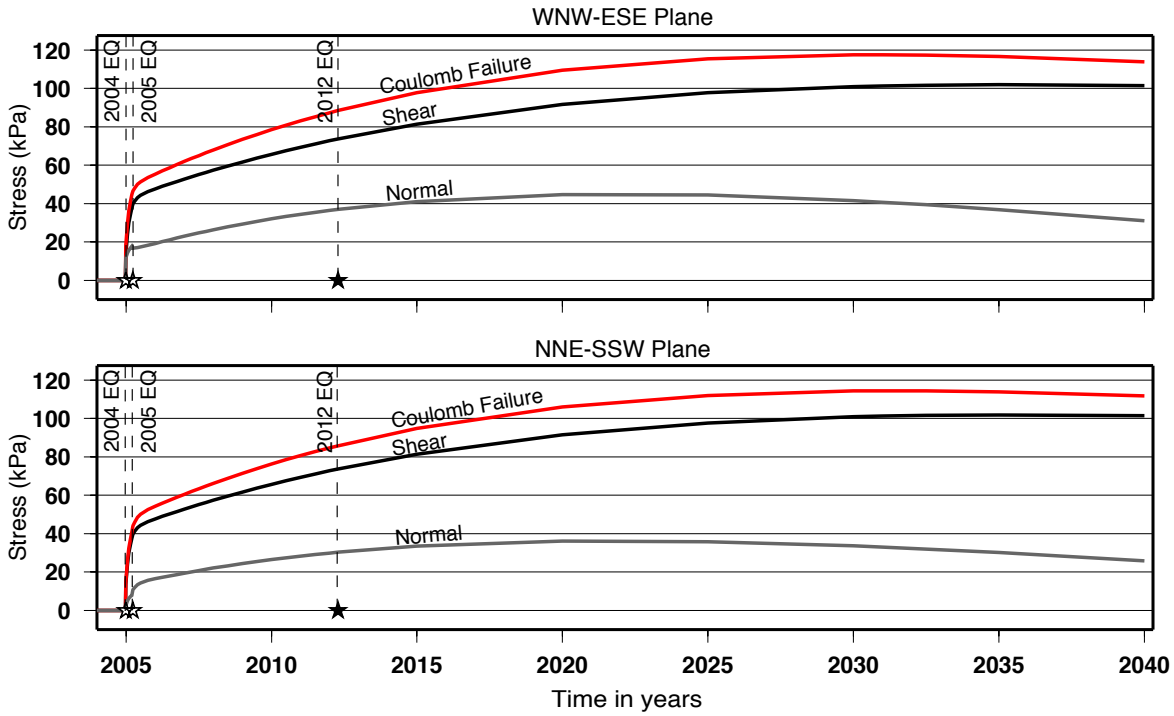

Figure 5.12: Stress time series. Cumulative coseismic and postseismic stress changes from the 2004 and 2005 earthquakes calculated at the 2012 hypocenter. The stresses are resolved on the WNW-ESE plane in the top panel and on the NNE-SSW plane in the bottom panel.

therefore great oceanic strike-slip earthquakes in the northern Wharton Basin may coincide with the Sunda megathrust earthquakes every 1-2 cycles. This quasi-phase locking between the megathrust and strike-slip faulting in the northern Wharton Basin is speculative, but could be similar to the fault synchronization observed by Scholz [2010] in the Iceland seismic zone, Central Nevada seismic belt, and the Eastern California shear zone. Although these 2012 earthquakes did not cause much damage or casualties, they highlight the risk that very large earthquakes can occur away from major plate boundaries, and that unexpected events can be triggered well after great megathrust earthquakes.

Chapter 6

Viscoelastic Relaxation in a Heterogenous Earth from Transient Deformation in Southeast Asia Following the 2004 Sumatra-Andaman Earthquake

6.1 Abstract

Investigations of postseismic deformation are often plagued by ambiguities between fundamental deformation processes that can be expected to contribute to the deformation field at different times and distances from the rupture, including viscous flow, localized afterslip and poroelastic rebound. Previous analysis of the 2004 Sumatra-Andaman earthquake have primarily focused on either the near-field or the far-field postseismic deformation field, and explained the motion with afterslip, poroelastic rebound, viscoelastic relaxation, or a combination of multiple mechanisms. In this study, we explore the influence of 3-D heterogeneity on viscoelastic relaxation models, in an attempt to simultaneously fit both the far-field and the near-field postseismic deformation with one mechanism. For our geodetic data, we've collated both horizontal and vertical GPS observations, that span the first five years of postseismic deformation, from the Andaman and Sumatran Islands, mainland Sumatra, Thailand, the Malay Peninsula, the Indian Ocean, and India. In our postseismic models, we include not only the 2004 M_w 9.2 megathrust earthquake, but contributions from the 2005 M_w 8.7 Nias and 2007 M_w 8.4 Bengkulu earthquakes. Our investigation of 3-D viscoelastic relaxation models indicates that it is a of first order importance to include a stronger oceanic mantle to fit the postseismic deformation observations following the succession of megathrust earthquakes.

6.2 Introduction

Crustal deformation following megathrust earthquakes provides insight into the rheology of the mantle. The 2004 earthquake, and subsequent 2005 and 2007 events, produced large stress increases in the crust surrounding the ruptures, and in the mantle downdip from the rupture zones. Transient deformation ensues when the ductile mantle begins to relax these coseismic stress changes. Over decadal time-scales, deep-seated transient postseismic relaxation can produce crustal deformation exceeding that from the earthquake itself in the intermediate-to-far field range. Without significant 3-D heterogeneity in the lithosphere and upper mantle, one would expect to observe the surface moving towards the downdip end of the coseismic rupture plane. Subsidence should be localized to the zone above the rupture bottom, surrounded by a broad regional uplift. The deformation magnitude is dependent on the earthquake source, mantle rheology, and the thickness of the elastic lithosphere. However, we expect the lithosphere and upper mantle in Southeast Asia to have significant 3-D heterogeneity based on geological and seismological considerations. Oceanic lithosphere thickness is dependent on the age of the oceanic crust, which varies by $\sim$ 70 Ma along the Andaman-Sunda-Java Trench [Müller et al., 1997], but in general oceanic lithosphere is thinner than the continental lithosphere of the Sunda Plate. The Andaman Sea is an active back-arc basin [Curray, 2005], and low seismic velocities in this region imply a locally warmer, weaker mantle [Shapiro et al., 2008]. Thus, we test a variety of earth structures, using a finite element model approach, ranging from a simple 1-D layered model to a 3-D model that includes an elastic subducting slab and a low-viscosity back-arc spreading center, to determine the effects on crustal deformation in the near-to-far field range.

6.3 Geodetic Observations

We have collated a combination of continuous and campaign GPS data from throughout Southeast Asia spanning the first five years following the 2004 Sumatra-Andaman earthquake. The geodetic data comes from several GPS networks: the Andaman and Nicobar Postseismic Network (ANPN), Badan Koordinasi Survei dan Pemetaan Nasional (BAKOSURTANAL), the International GPS Service (IGS), the Malaysia Active GPS System (MASS), the Royal Thai Survey Department (RTSD), and the Sumatran GPS Array (SuGAr) (sites shown in Figure 6.1). The GPS positions are calculated in the ITRF 2005 reference frame and continuous interseismic velocities due to the plate motion between the subducting Indo-Australian Plate and the overriding Sunda Plate have been removed from the time series. The removed interseismic velocities are either motions recorded at the individual sites before the 2004 earthquake, or inferred from the Apel [2011] block model.

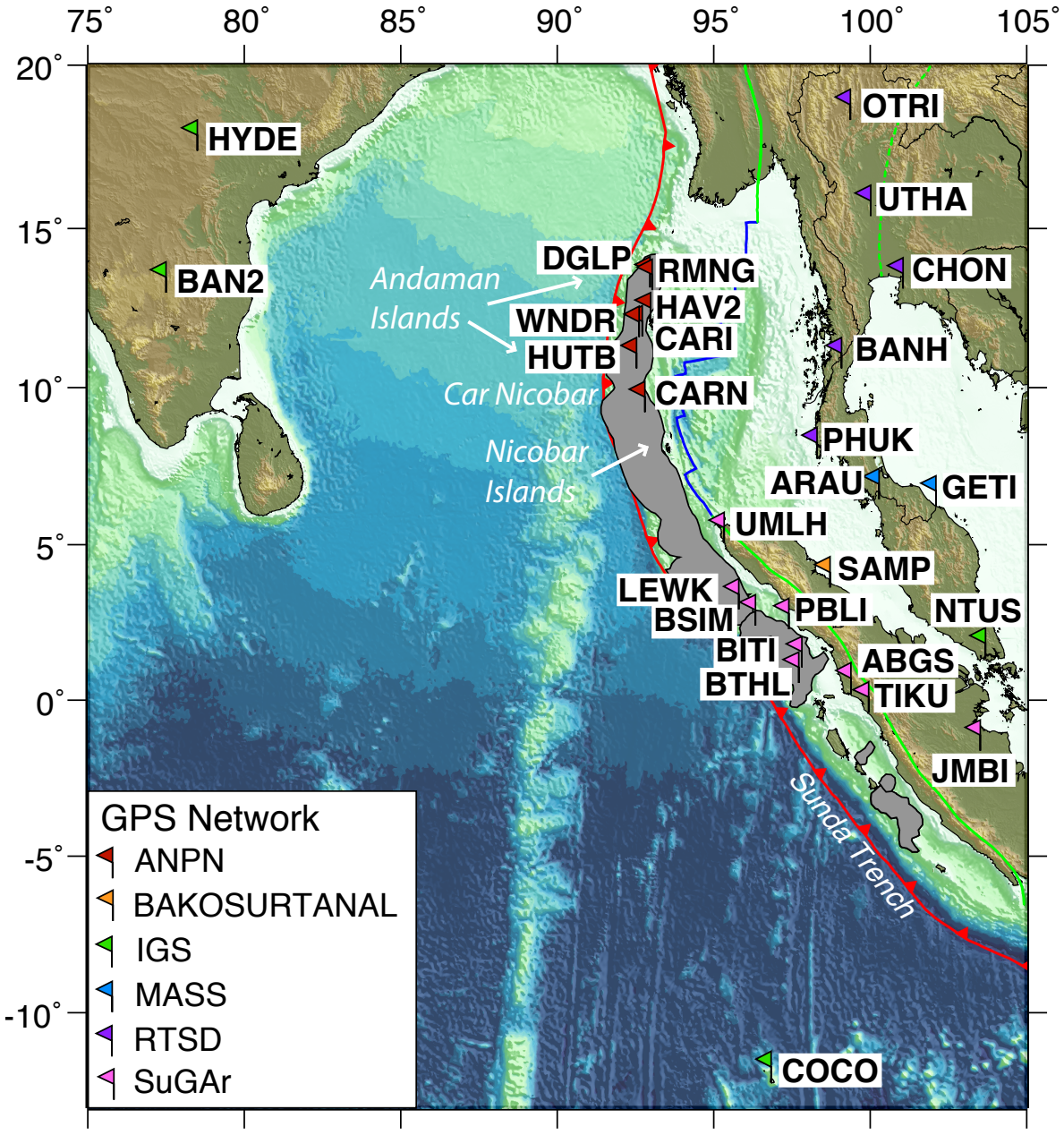

Figure 6.1: Overview map showing the megathrust earthquakes included in the viscoelastic modeling, shaded gray, and all the GPS stations used in the study

6.3.1 Near-field Observations

The 2004 earthquake produced between ∼1.4-4.7 m of southwestward horizontal displacement at the Andaman Islands sites, located directly above the rupture zone. The vertical displacement ranged from 0.9 m of subsidence to 0.9 m of uplift (shown in Figure 6.12a, data from Banerjee et al. [2007]). The earliest postseismic observations start 15-40 days after the earthquake. During the first five years, the cumulative horizontal displacements were ∼0.4-0.6 m oriented approximately westward, and between 0.2-0.3 m of uplift (representative sites shown in Figure 6.13, data from Paul et al. [2012]). The postseismic deformation rapidly decayed for the first year and then the trend became more linear (see time series in Figure 6.2, 6.17).

The 2004 earthquake produced up to ∼5.7 m of southwestward horizontal displacement at the islands offshore of northern Sumatra, near the southern termination of the rupture, and up to 2.1 m of uplift (shown in Figure 6.12a, data from Subarya et al. [2006]). Three months later, the Nias earthquake ruptured the segment of the Sunda megathrust just south of the 2004 rupture and produced up to ∼ 4.5 m of southwestward horizontal motion and 2.9 m of uplift (Figure 6.12b, data from Konca et al. [2007]). Rapidly decaying postseismic deformation was also observed following the Nias earthquake, and Hsu et al. [2006] model the first 11 months of deformation as aseismic afterslip located both updip and downdip of the rupture, with geodetic moment equivalent to M_w 8.2. Figure 6.3 shows the time series for the island sites starting one year after the 2005 earthquake, when the rapidly decaying motion has decreased. During the next four years,the sites continue to move towards the trench on the order of centimeters per year. The orientation and magnitude of vertical deformation varies greatly among the sites and may help to differentiate postseismic models.

6.3.2 Intermediate-field Observations

The sites on the northernmost tip of Sumatra experienced between ∼1.7-3.7 m of southwestward horizontal coseismic displacement, with ∼0.1-0.6 m of subsidence (shown in Figure 6.12a, data from Subarya et al. [2006]). These sites only moved a few centimeters during the 2005 earthquake. SAMP, on the eastern coast of northern Sumatra, experienced 10-20 cm of trenchward motion during both the 2004 and 2005 earthquakes, with only ∼1 cm of vertical displacement. These sites continued to deform between ∼0.3-1.1 m trenchward during the first five years following the 2004 earthquake (representative sites shown in Figure 6.13, data from SOPAC and Paramesh Banerjee [personal communication, 2012]). The cites on the western coast of central Sumatra moved <1 cm during the 2004 earthquake, but had coseismic displacements on the order of centimeters for both the 2005 and 2007 earthquakes. JMBI on the eastern coast displaced centimeters during the 2007 earthquake, but <1 cm during the 2004 and 2005 earthquakes. These central Sumatran cites had transient horizon-

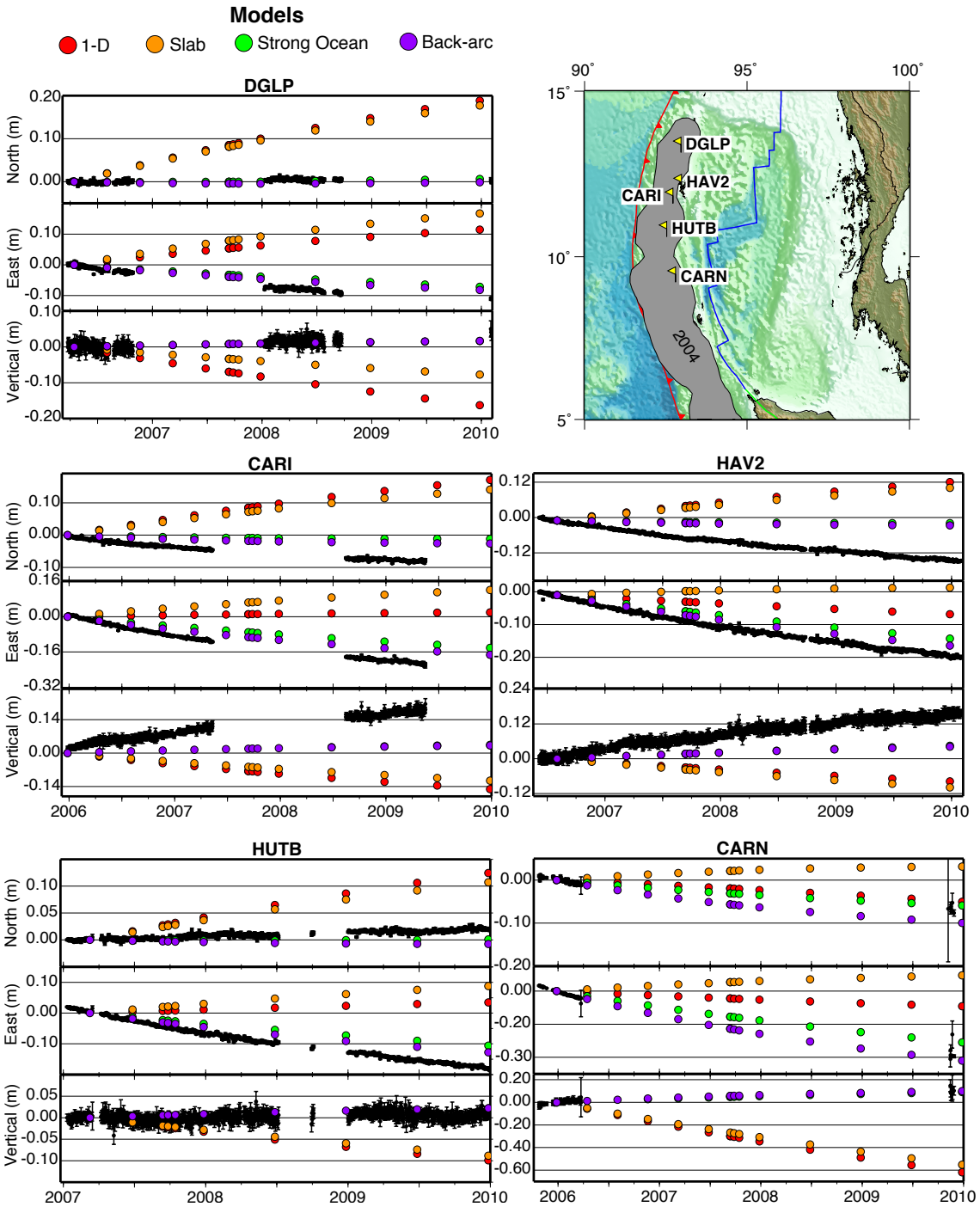

Figure 6.2: Andaman Islands time series (ANPN GPS network data, processed by Paul et al. [2012]) compared with viscoelastic models, starting 1 year after the 2004 Sumatra-Andaman earthquake (or when data is available), after the rapidly decaying transient motions.

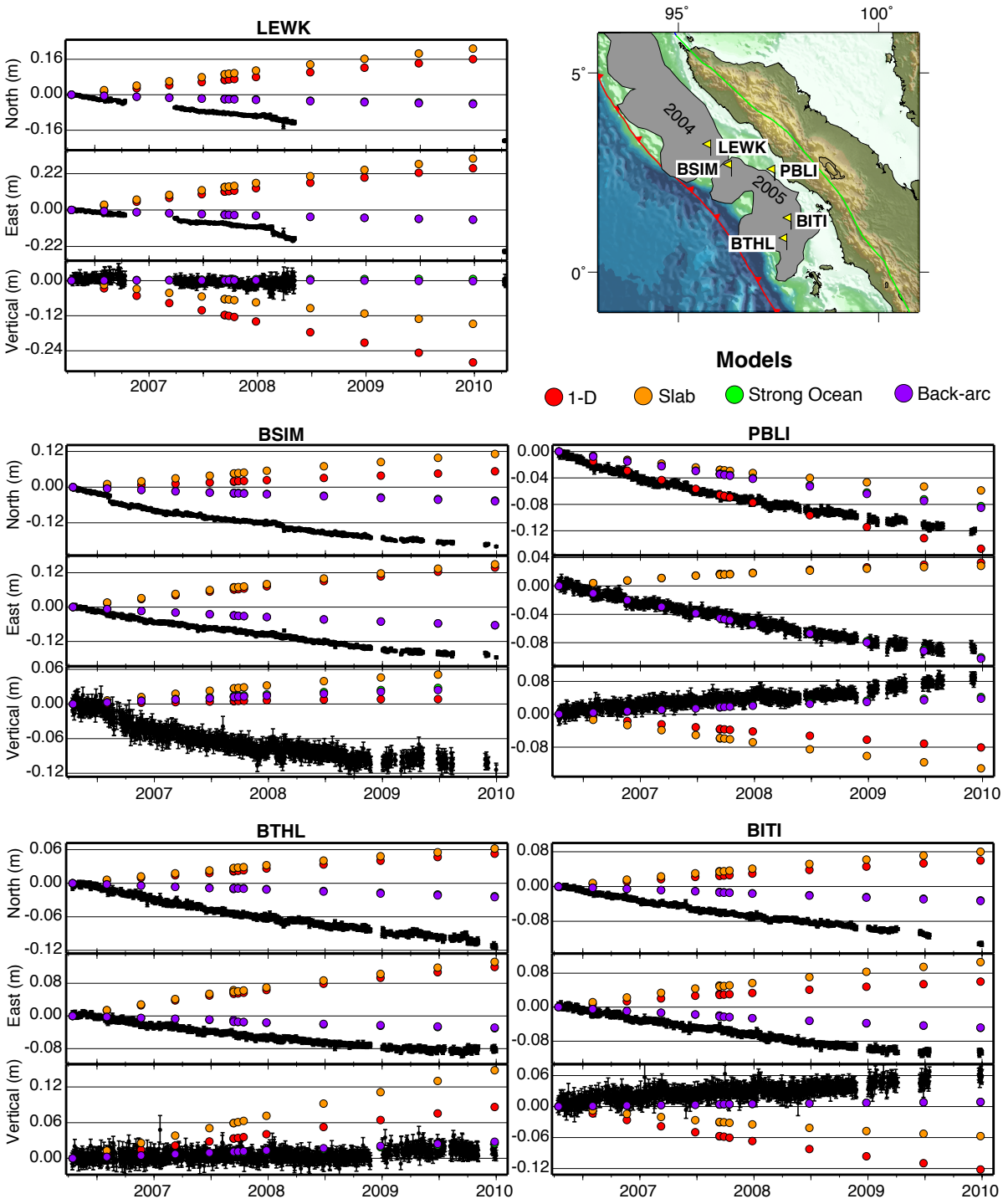

Figure 6.3: Sumatran Islands time series (SuGAr GPS network data, processed by Paramesh Banerjee [personal communication, 2012]) compared with viscoelastic models, starting 1 year after the 2005 Nias earthquake, after the rapidly decaying transient motions.

tal motion on the order of centimeters during the first 5 years following the 2004 earthquake, with no vertical deformation (time series starting one year after the Nias earthquake are shown in Figure 6.4).

6.3.3 Far-field observations

There was a wide range of 2004 horizontal displacements observed in Thailand and the Malay Peninsula, across the Andaman Sea from the 2004 rupture. Northern Thailand displaced a few centimeters, central Thailand ∼6-8 cm , and the peak displacements of ∼ 0.3 m were observed on the island of Phuket, offshore of southern Thailand. Northern Malaysia had ∼8-15 cm of horizontal displacement and Singapore, on the bottom of the Malay Peninsula had 2 cm (shown in Figure 6.12a, data from Vigny et al. [2005]). PHUK and the sites further south experienced southward coseismic displacement during the 2005 earthquake on the order of centimeters. NTUS, in Singapore, also displaced a few centimeters trenchward during the 2007 earthquake, followed by a rapidly decaying transient on the order of a few months (see time series in Figure 6.6). During the first five years, these Thai and Malay Peninsula sites have already experienced more cumulative postseismic deformation than coseimic displacements, peaking at PHUK with ∼0.4 m of southwestward motion (see time series in Figures 6.5, 6.6).

The very far-field sites in the Indian Ocean and India experienced very little coseismic and postseismic deformation. The Indian sites moved eastward ∼1 cm during the 2004 earthquake, and have moved another ∼1 cm eastward in the first five years. COCO, in the Indian Ocean offshore of southern Sumatra displaced <1 cm during the 2004 earthquake, and ∼1 cm north during the 2007 earthquake. It has moved another ∼1 cm north during the first 5 years (see time series in Figure 6.7).

6.4 Viscoelastic Modeling Method

6.4.1 Finite Element Model

We use the Abaqus finite element modeling software to model the postseismic deformation following the 2004, 2005, and 2007 megathrust earthquakes. The subduction interface, used both as the fault contact and for geometrical constraints, is based on the Sumatra-Java slab model from Slab1.0 [Hayes et al., 2012]. Slab1.0 is a compilation of 3-D subduction geometries, based on probabilistic non-linear fit to a combination of independent data sets including: active source seismic data, several earthquake catalogs, global plate boundaries, high-resolution bathymetry data, and sediment thickness data. We contoured the Sumatra-Java slab surface at 20 km, 30 km, 50 km, 70 km, 150 km, 300 km, and 500 km depths. We assume that the trench is at the surface, and do not consider seafloor bathymetry or

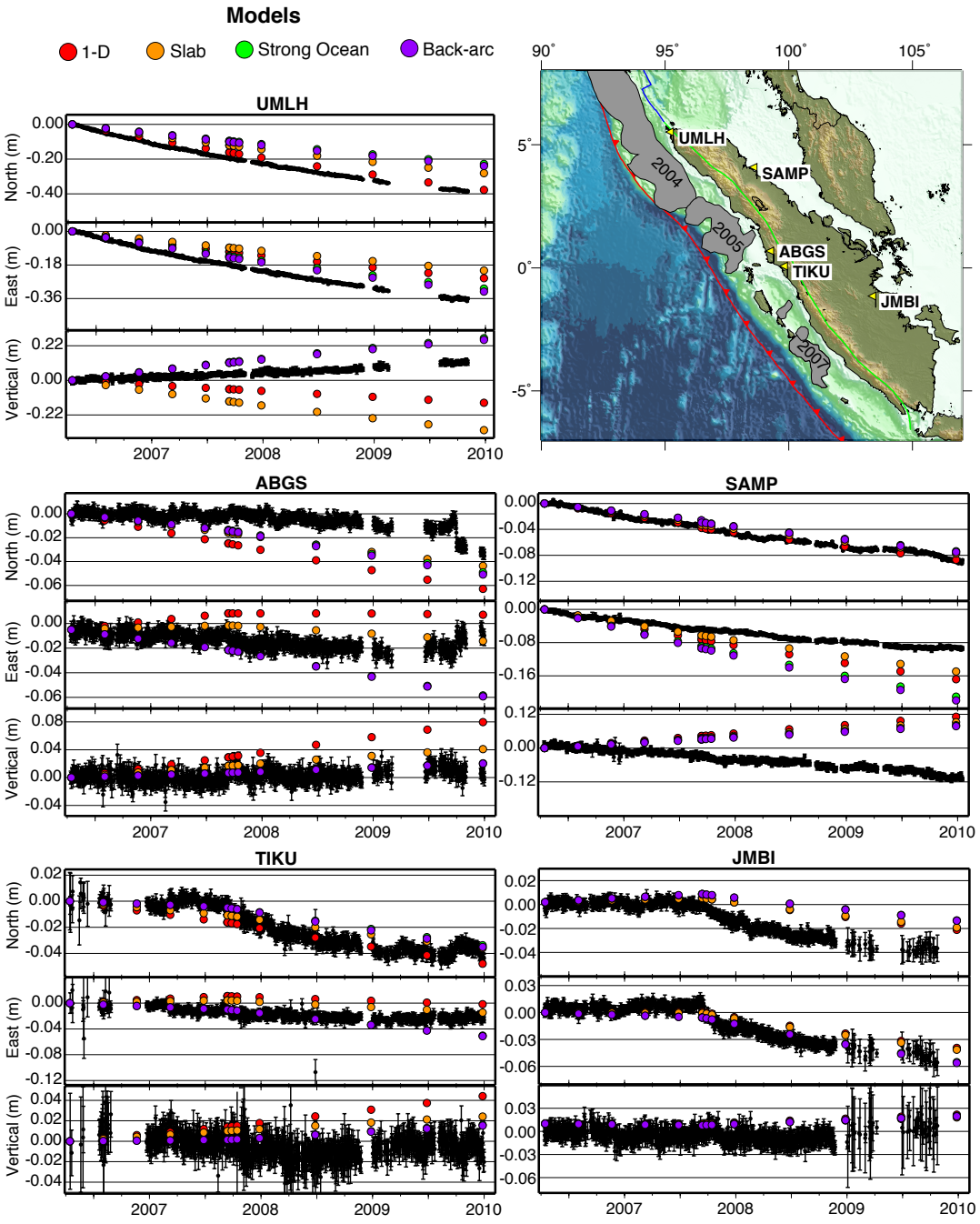

Figure 6.4: Sumatran time series (SuGAr and BAKOSURTANAL GPS network data, processed by Paramesh Banerjee [personal communication, 2012] and SOPAC) compared with viscoelastic models, starting 1year after the 2005 Nias earthquake, after the rapidly decaying transient motions. The 2007 coseismic displacement has been removed from the ABGS, TIKU, and JMBI time series and models.

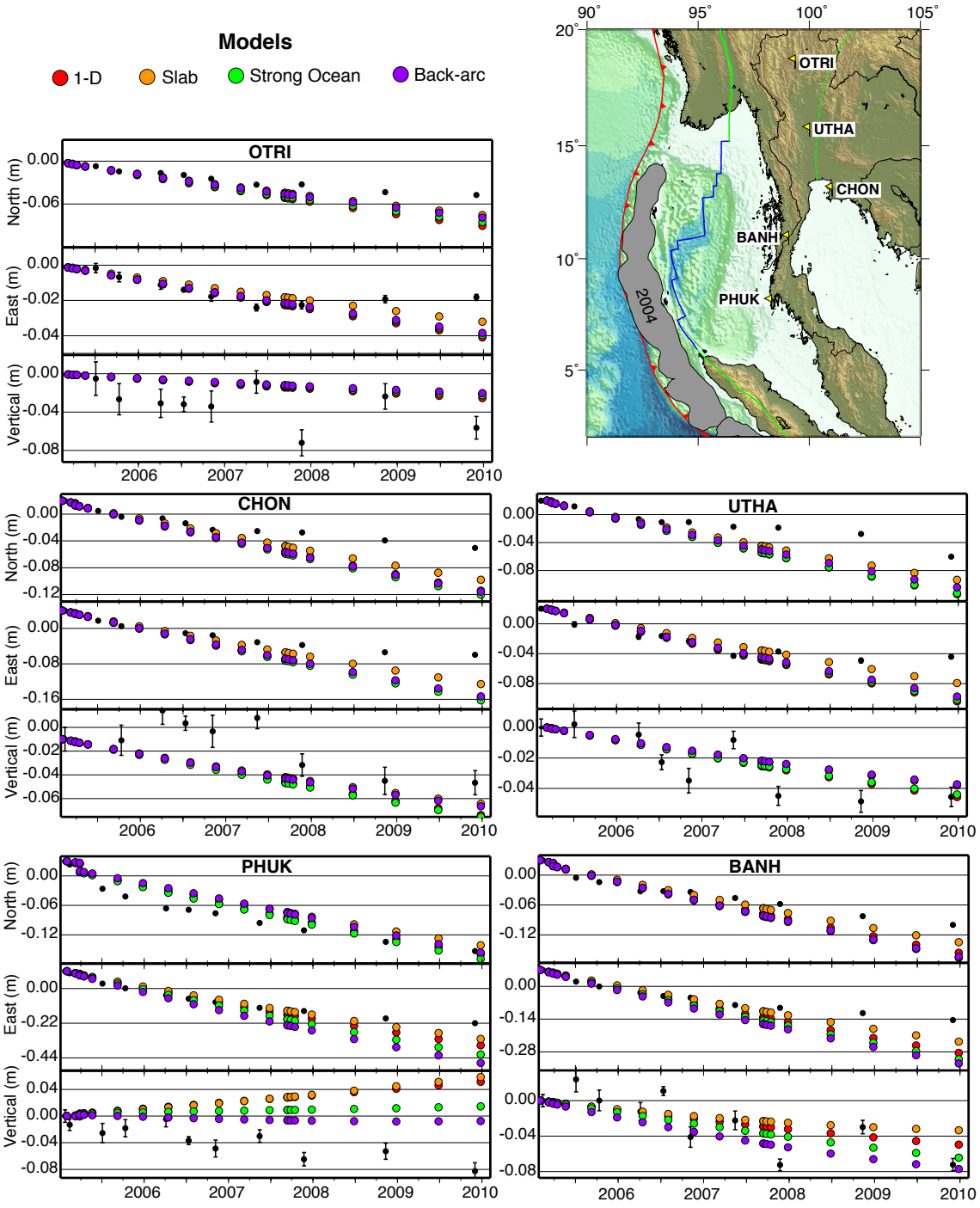

Figure 6.5: Thai time series (RTSD GPS network data, processed by Panumastrakul et al. [2012]) compared with viscoelastic models for the first 5 years following the 2004 Sumatra-Andaman earthquake.

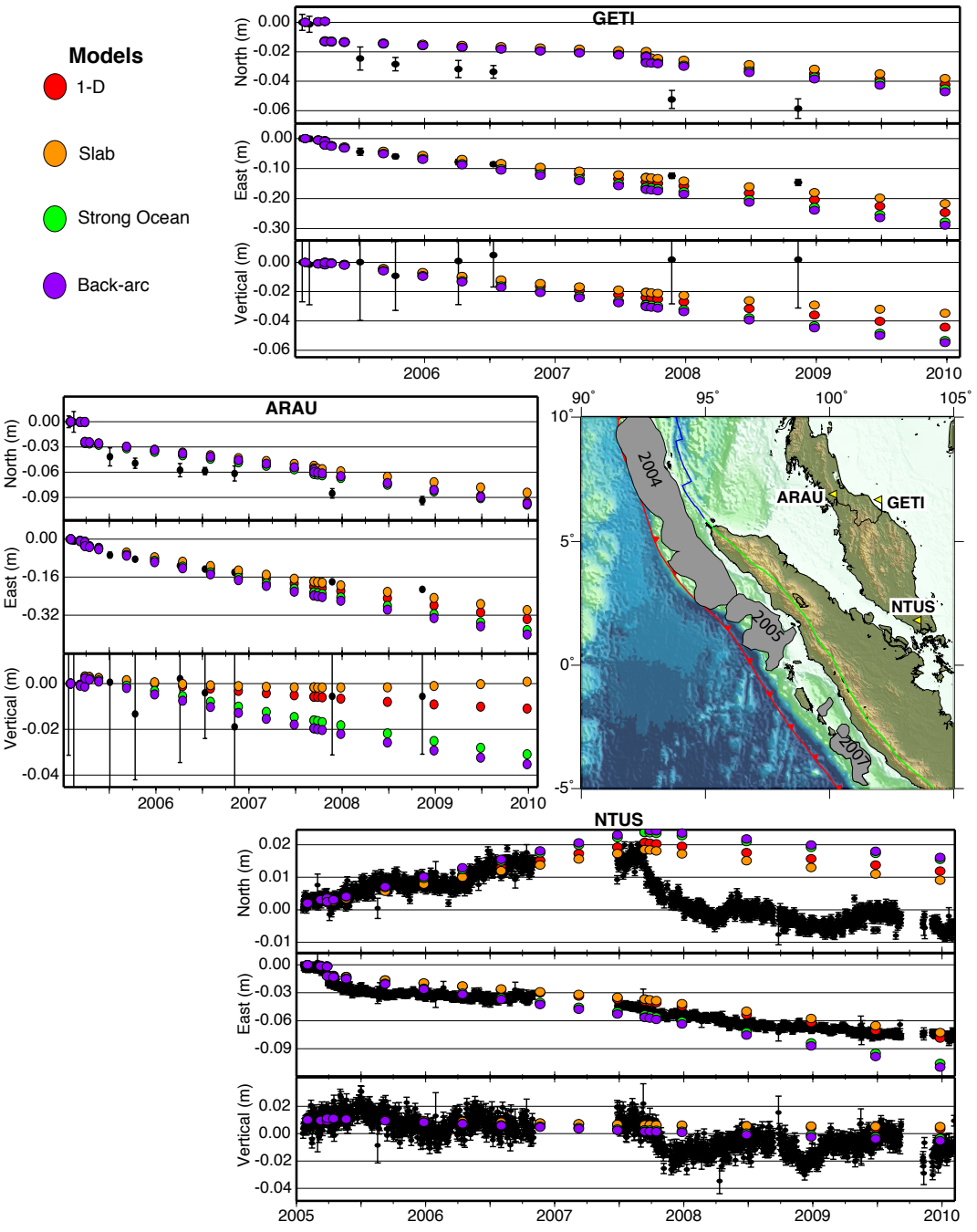

Figure 6.6: Malay Peninsula time series (MASS and IGS GPS network data, processed by Panumastrakul et al. [2012] and SOPAC) compared with viscoelastic models for the first 5 years following the 2004 Sumatra-Andaman earthquake. The 2007 coseismic displacement has been removed from the NTUS time series and models.

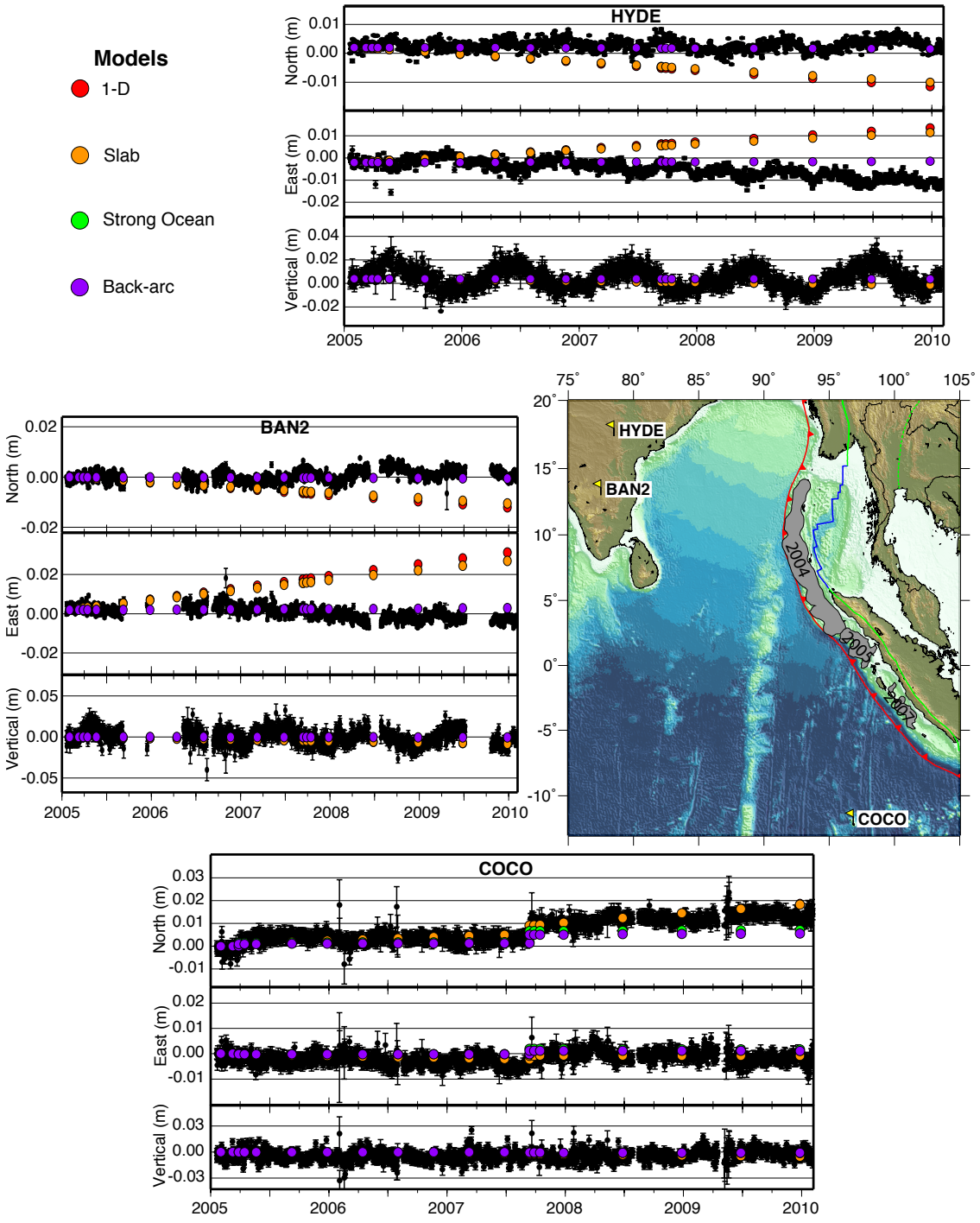

Figure 6.7: Indian Ocean and Indian time series (IGS GPS network data, processed by SOPAC) compared with viscoelastic models for the first 5 years following the 2004 Sumatra-Andaman earthquake.

topography. To simplify the slab geometry, we manually decimated the Slab1.0 model along strike, keeping the prominent structural features intact while segmenting the slab surface on average every 240 km. We extend the Sumatra slab beyond the 10° N limit of Slab 1.0 along the strike of the Andaman trench until 24° N, while assuming the same slab dips as at the northern extent of the Slab1.0 model. We use the Java slab surface until 115° E. We additionally extend the model volume, and subduction interface, 1000 km to the north and east to ensure that our GPS sites are located far from the model boundaries. The western edge of the model volume is ∼3000 km west of the 2004 rupture and the eastern edge of the model is ∼2500 km east of the 2007 rupture. The total rectangular volume is $\sim$ 6600 km $\times$ $\sim$ 5900 km $\times$ 500 km. We use quadratic tetrahedral elements for the mesh, with between $\sim 400,000 - 450,000$ thousand elements for the various 3-D models (example mesh shown in Figure 6.11). For all of the models, the boundary conditions are a free surface with zero displacements or rotations at the lateral and bottom boundaries.

6.4.2 Model Geometry and Rheology

The simplest model we test is a 1-D layered model (Figure 6.8). It includes a 70 km thick elastic lithosphere, above a ductile asthenosphere and upper mantle. The asthenosphere and upper mantle have the same viscosity in this 1-D model, and in the more complex models discussed next. We justify this simplification based on the postseismic deformation study by Panet et al. [2010], that modeled the first ∼3 years of far-field GPS data and regional GRACE gravity signal following the 2004 and 2005 megathrust earthquakes, and found that constant steady-state viscosity throughout the entire ductile portion of the mantle provides the best fit to the GRACE data. Since this study is focused on deducing the impacts of 3-D earth heterogeneity in viscoelastic models, we chose to use a simple Maxwell rheology for the ductile portions of the mantle. Using a forward modeling approach, we optimized the steady-state viscosity to fit the far-field GPS sites in Thailand and the Malay Peninsula. We tested viscosities ranging between 4×10^{17} Pa s and 8×10^{18} Pa s, the values used in the Panet et al. [2010] study for the transient and steady-state viscosity in their bi-viscous Burgers body rheology model. The preferred steady-state viscosity to fit the first five years of far-field postseismic deformation is 3×10^{18} Pa s. In the rest of the earth models, we add 3-D geometrical complexity in an attempt to improve the fit to the near-to-intermediate field postseismic observations.

In the next model, we include a subducting slab. The elastic slab is 40 km thick, and follows the geometry of the slab interface as described in the Finite Element Model section above. The mantle rheology is the same on both the oceanic and continental sides of the slab, and we use the same Maxwell viscosity as determined for the 1-D model (Figure 6.8).

In the next iteration, we use a different Maxwell rheology on either side of the slab (Fig-

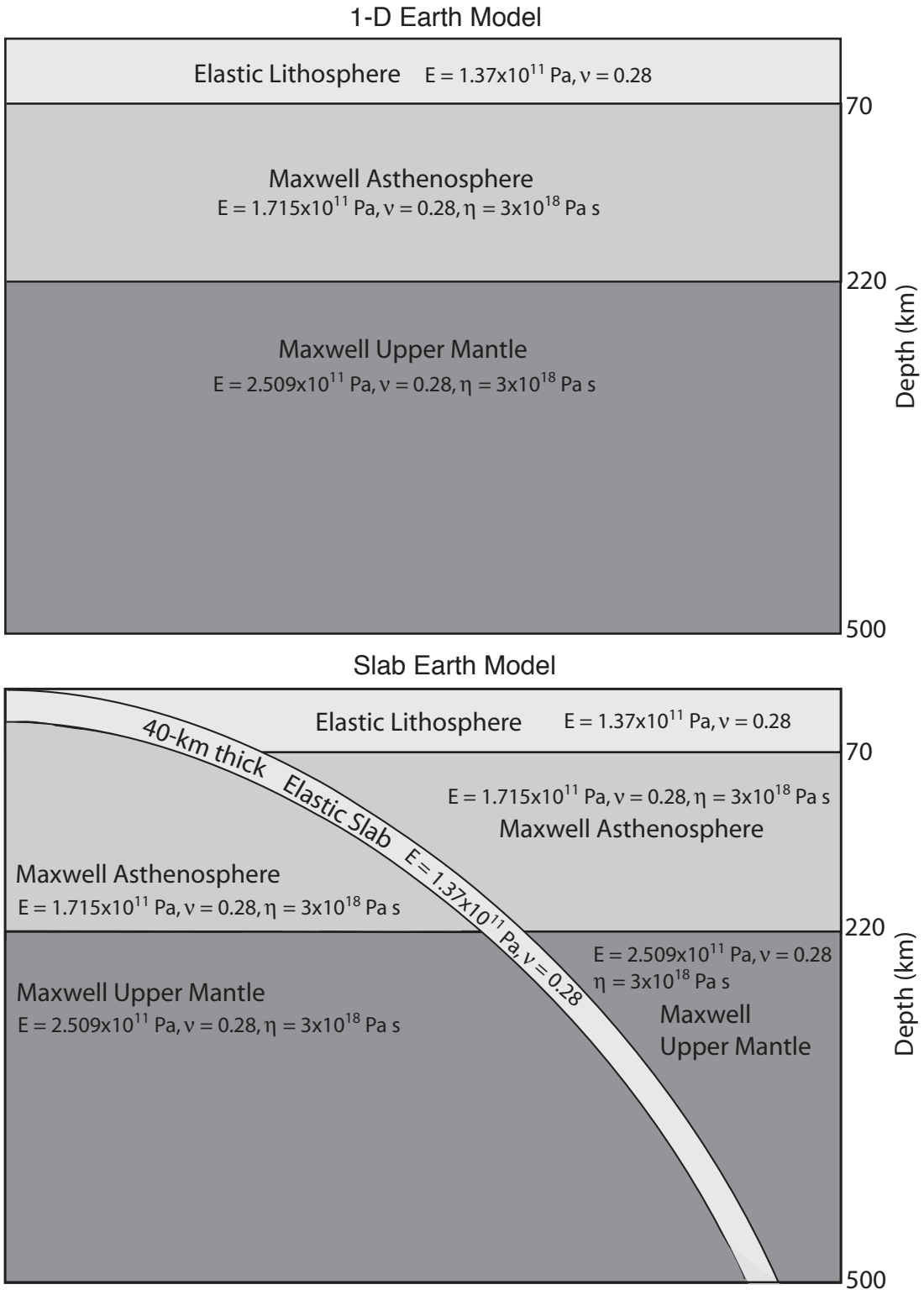

Figure 6.8: 1-D and Slab Earth Model schematics

ure 6.9). Wang [2007] determines that a strong oceanic mantle, with an order of magnitude higher viscosity than the continental mantle, is necessary to fit the uplift histories of the Washington coast following the last great Cascadia megathrust earthquake. The shear-wave tomography study by Shapiro et al. [2008], that spans the Andaman-Sunda-Java subduction zone, also suggests a stronger oceanic asthenosphere based on higher shear wave velocities for depths ranging from ∼25-150 km. The shear wave anomalies between the oceanic and continental sides of the trench are more pronounced in the Andaman segment of the subduction zone than in the Sumatran segment. For simplicity we neglect the second order variations, and assume a uniform oceanic mantle viscosity 10 times larger than the continental mantle viscosity.

In the final model, we add a low-viscosity zone representing the Andaman back-arc spreading center (Figure 6.9). We approximate the geometry of the low-viscosity zone based on the Shapiro et al. [2008] low shear-wave region beneath the Andaman Sea. Shapiro et al. [2008] can't constrain the seismic velocities shallower than ∼40 km depth, so the low-velocity zone may in actuality be shallower than we are currently modeling it (3-D geometry shown in Figure 6.10). We assume a steady-state viscosity equal to half the continental mantle viscosity.

6.4.3 Input Source Models

We adapt previously published source models for the megathrust earthquakes for our coseismic input. We start by projecting the 1, 3, 6, 9, and 15 m slip contours from the geodetically constrained Chlieh et al. [2007] 2004 source model onto our slab interface. The slip contours are manually adjusted to fit within our fault segment constraints. Then we tweak the slip magnitudes at each contour by forward modeling until we get a good fit to the geodetic data (Figure 6.12a). We are actually able to fit the Andaman and Nicobar Island coseismic displacements better than the original Chlieh et al. [2007] model. We are also able to fit the far-field geodetic data, confirming that our model volume is large enough for our zero displacements and rotation boundary conditions. We use the same approach for the 2005 and 2007 earthquakes, projecting the 1, 3, and 6 m slip contours from the Konca et al. [2007] 2005 and Konca et al. [2008] 2007 source models, both of which are constrained by both geodetic and seismic data. We include both the M_w 8.4 mainshock and the M_w 7.9 afterhshock for the 2007 earthquake source. We refrain from including the small, deep, and outlying 1-m slip contours for the 2005 and 2007 earthquakes, thus our fits to the geodetic data (Figure 6.12b,c) are slightly worse than the original model fits.

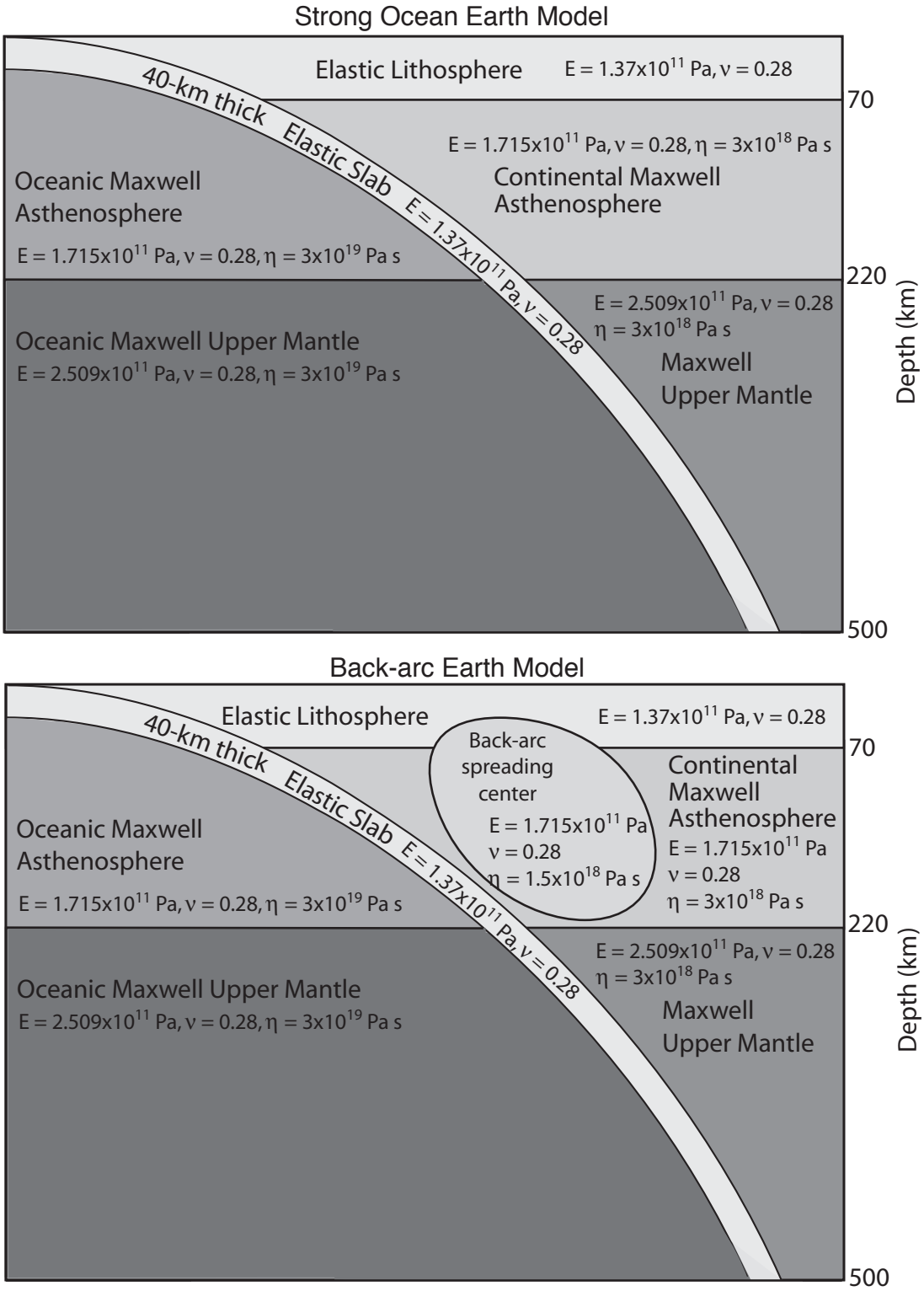

Figure 6.9: Strong Ocean and Back-arc Earth Model schematics

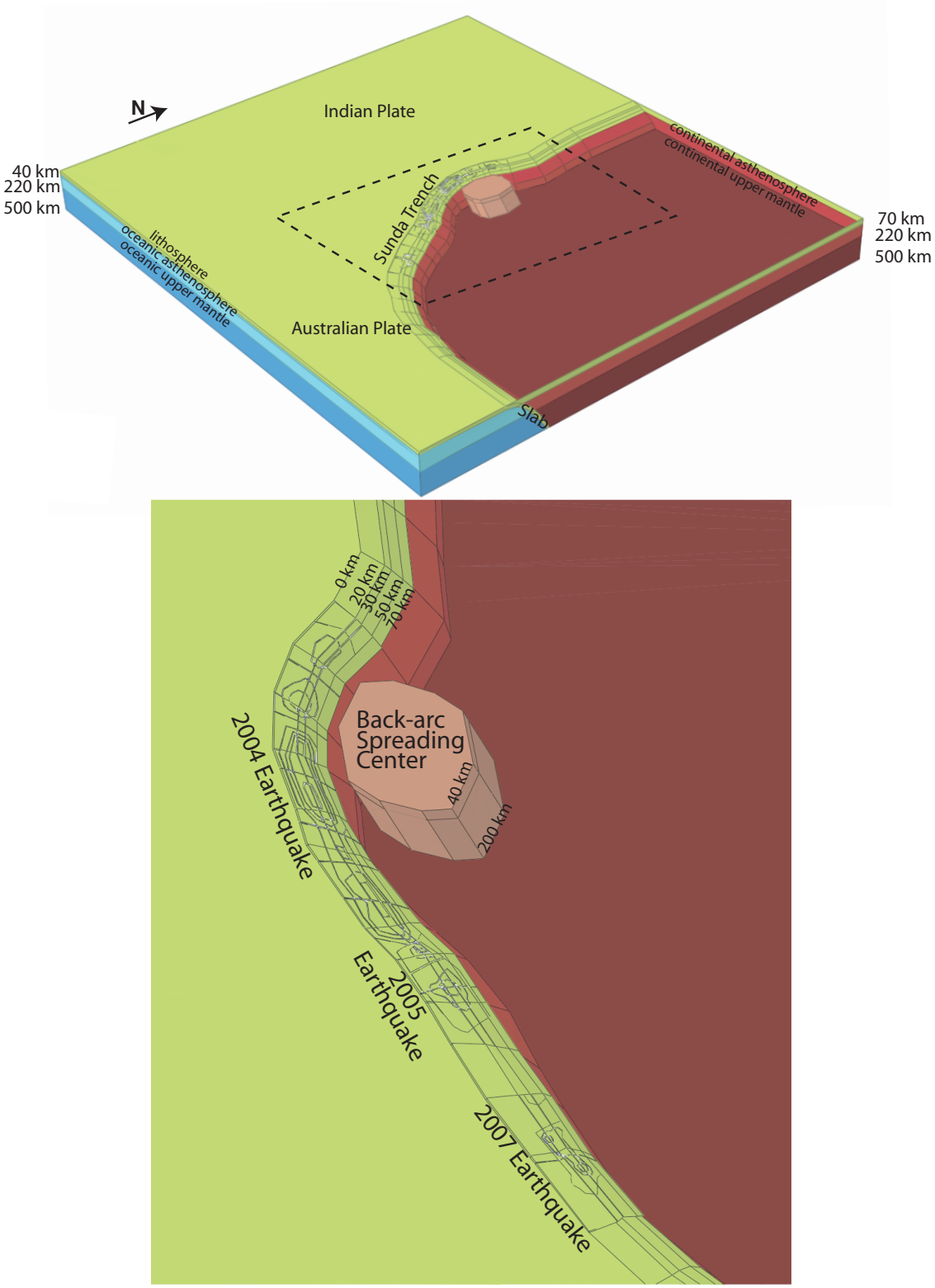

Figure 6.10: 3-D geometry used in the Back-arc Earth Model.

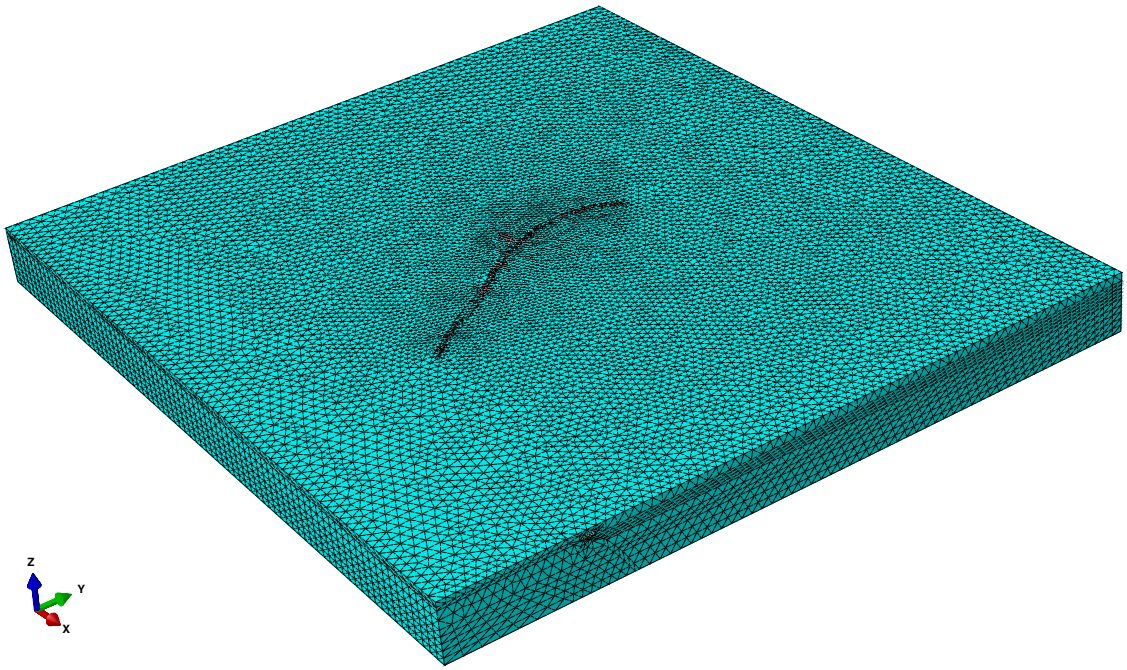

Figure 6.11: Mesh used in the Back-arc Earth Model

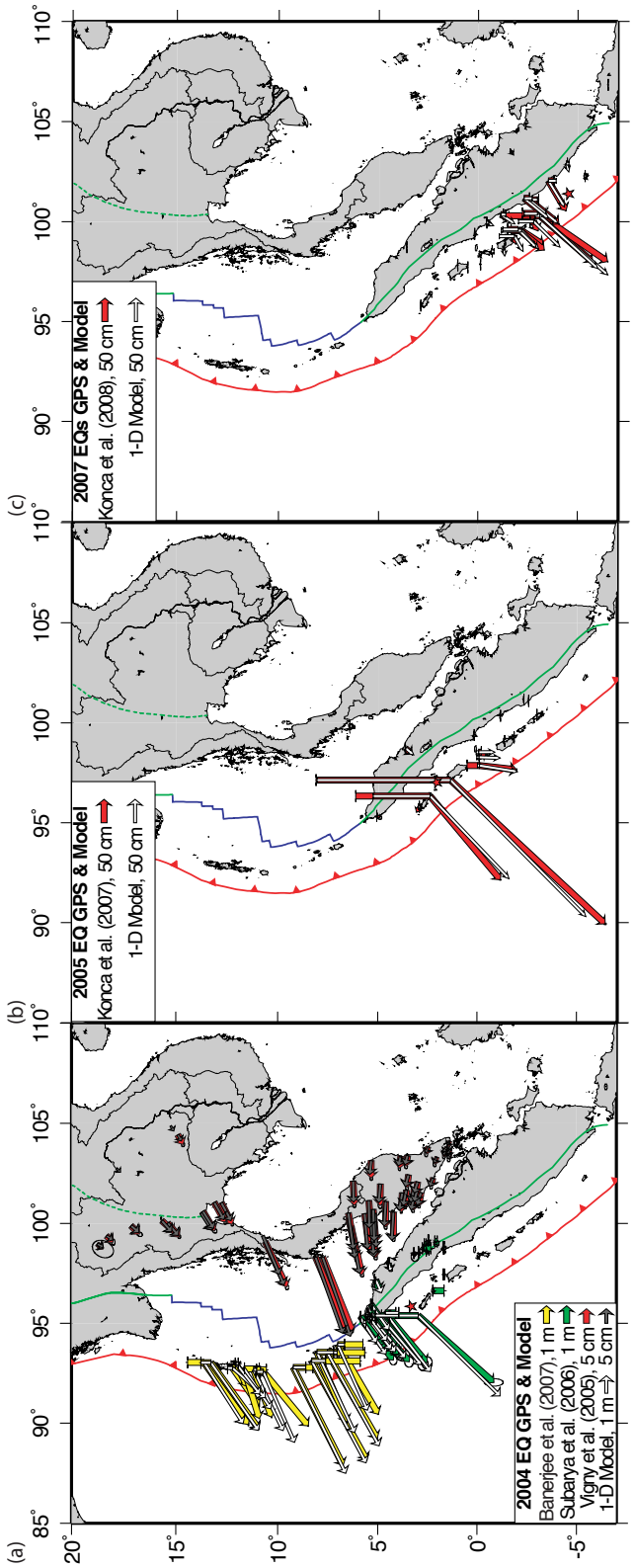

Figure 6.12: 1-D Earth Model fits to the coseismic GPS data for the a) 2004 M_w 9.2 Sumatra-Andaman earthquake [Banerjee et al., 2007; Subarya et al., 2006; Vigny et al., 2005], b) 2005 M_w 8.8 Nias earthquake [Konca et al., 2007], and c) 2007 M_w 8.4 and 7.9 Bengkulu earthquakes [Konca et al., 2008]. There are minimal differences when using the other earth models.

6.5 Model results

6.5.1 1-D Model

The 1-D Model produces horizontal deformation at the earth's surface oriented towards the downdip end of the coseismic rupture planes. Subsidence is localized to the zone above the rupture bottom, surrounded by a broad regional uplift. The magnitude of horizontal and vertical displacements are close to symmetric about the downdip end of the rupture planes. Figure 6.13 compares the cumulative viscoelastic relaxation during the first five years following the 2004, 2005, and 2007 earthquakes, with the GPS observations that span the entire time period. The near-field GPS observations fit the model very poorly, with the opposite sense of horizontal and vertical motion (also see time series in Figures 6.2,6.3). The intermediate-field sites on Sumatra have the correct sense of horizontal motion, but wrong sense of vertical displacement (Figure 6.4). The far-field sits in Thailand and the Malay Peninsula have the correct sense of motion, except for the vertical at the western most site PHUK (Figures 6.5,6.2). The model also over-predicts the cumulative postseismic deformation at the Indian sites (Figure 6.7).

6.5.2 Slab Model

Adding the 3-D structure of the elastic, subducting slab increases the eastward component of deformation in the near-field and shifts the pivot line separating uplift from subsidence further east. (Figure 6.14b). The addition of the elastic slab has a greater influence on vertical than on horizontal motions. It reduces the symmetry of the uplift pattern, so that there is much more postseismic uplift near the trench than in the Andaman back-arc basin. The north and vertical components of deformation improve at the Andaman sites, but the fit to eastern component worsens (Figure 6.2). BITI and LEWK have improved fits to the vertical deformation, but otherwise the Sumatran Islands sites do not show improvement. The far-field sites are minimally affected by the addition of the slab.

6.5.3 Strong Ocean Model

Adding a strong oceanic mantle dramatically changes the near-field deformation. There is added trenchward motion and uplift at the location of the forearc islands and subsidence near the trench (Figure 6.15b). The Strong Ocean Model produces the correct orientation of horizontal motion at the forearc islands, and the correct sense of vertical motion at all of the sites except BSIM (Figures 6.15a, 6.2, 6.3). The model also improves the fit to the vertical data at the northern Sumatra site UMLH (Figure 6.4). Deformation seaward of the trench is substantially reduced for the 5-year observation period, correlating with the lack

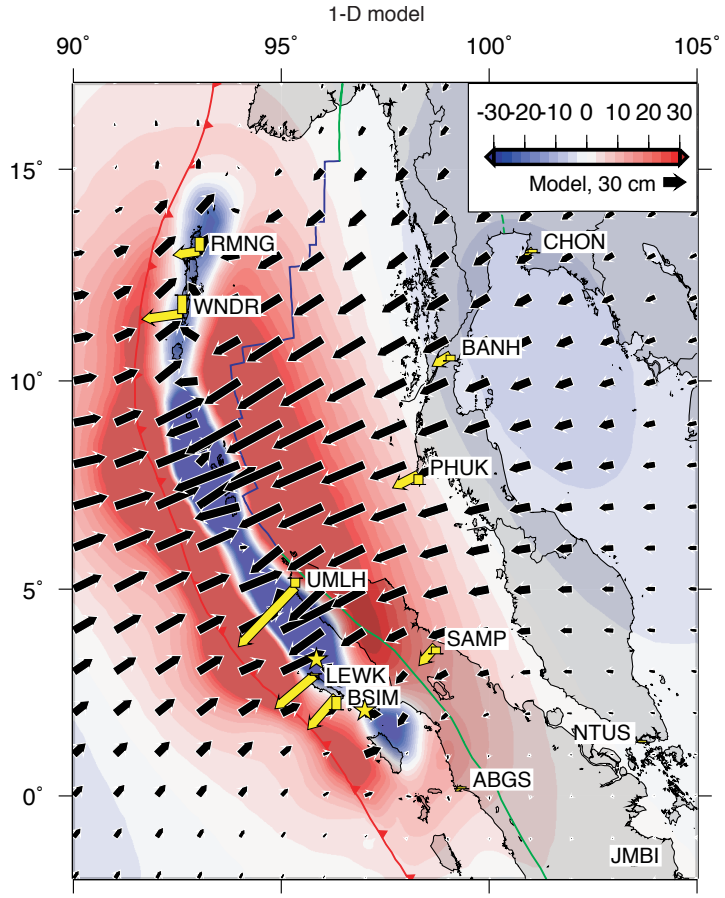

Figure 6.13: 5 years of cumulative viscoelastic relaxation following the 2004, 2005, and 2007 megathrust earthquakes using the 1-D Earth Model. Coseismic displacements for the megathrust earthquakes have been removed from both the model and GPS data.

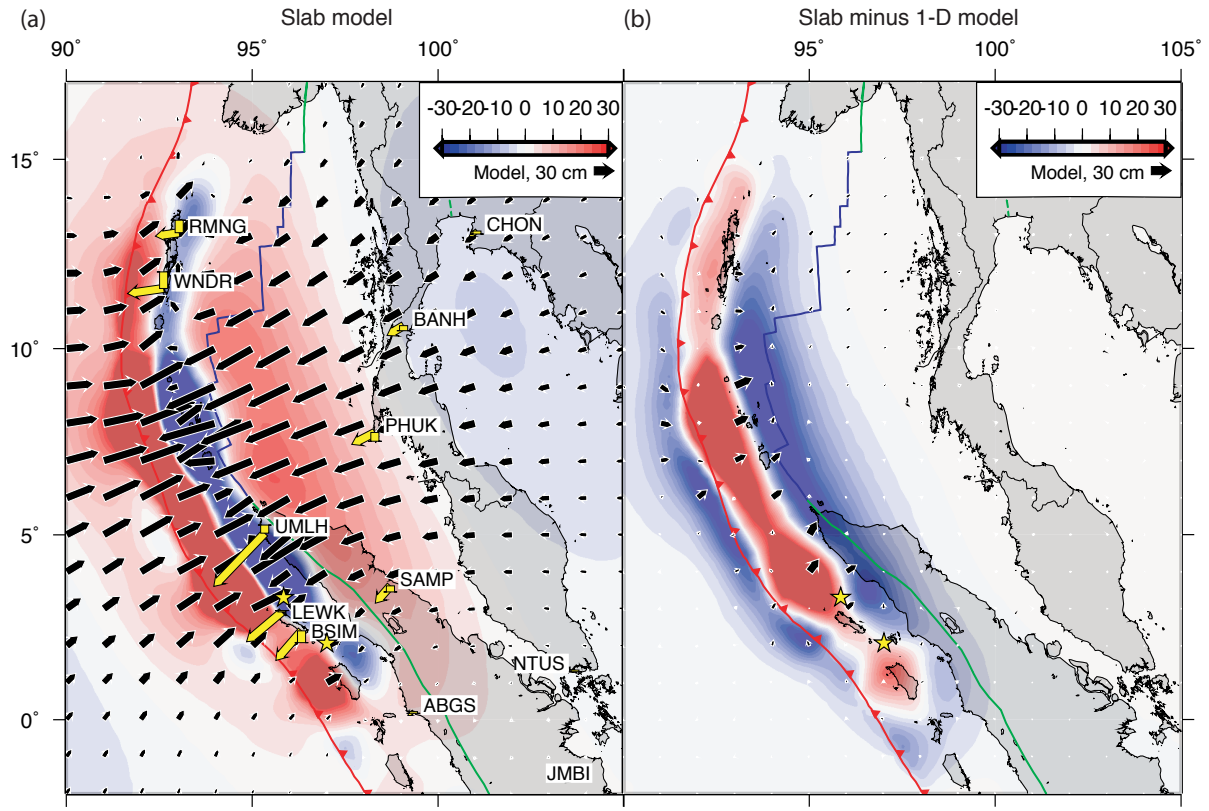

Figure 6.14: a) 5 years of cumulative viscoelastic relaxation following the 2004, 2005, and 2007 megathrust earthquakes using the Slab Earth Model. Coseismic displacements for the megathrust earthquakes have been removed from both the model and GPS data. b) The difference between the Slab Earth Model and the 1-D Earth Model cumulative viscoelastic relaxation.

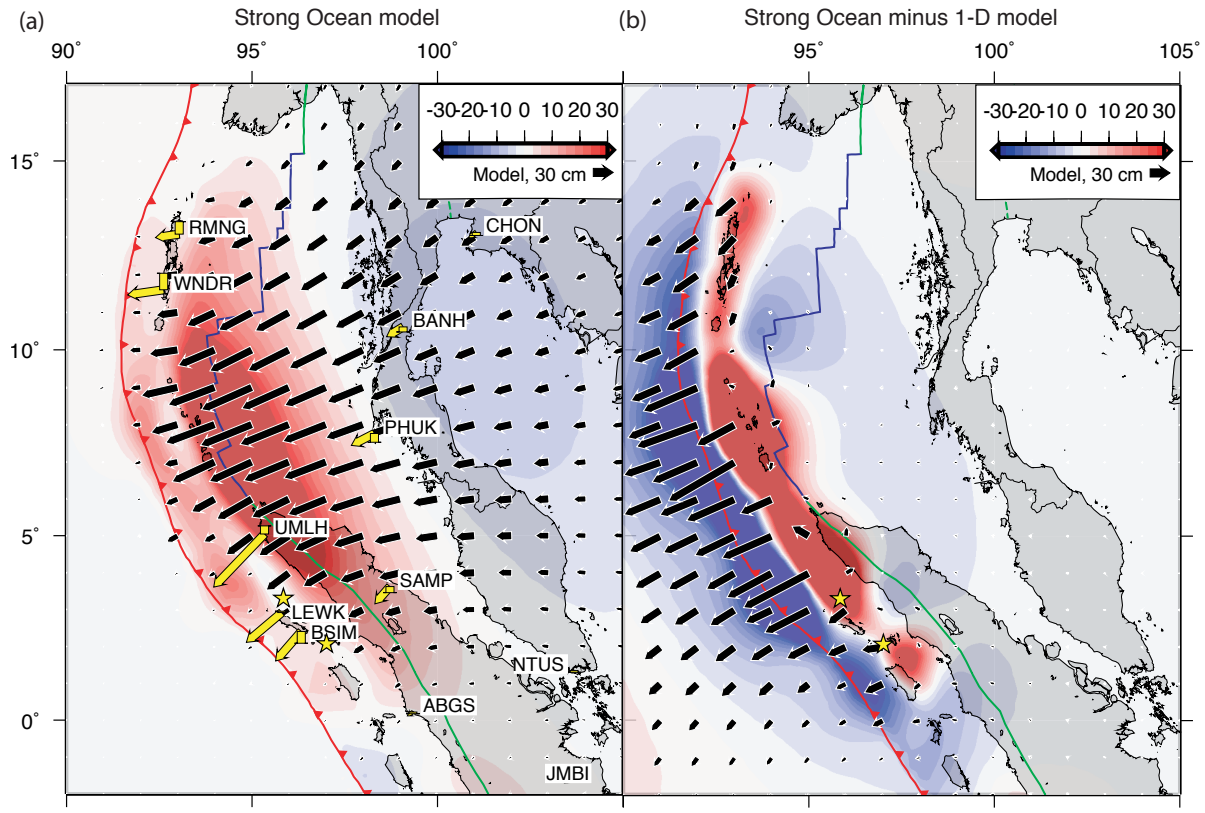

Figure 6.15: a) 5 years of cumulative viscoelastic relaxation following the 2004, 2005, and 2007 megathrust earthquakes using the Strong Ocean Earth Model. Coseismic displacements for the megathrust earthquakes have been removed from both the model and GPS data. b) The difference between the Strong Ocean Earth Model and the 1-D Earth Model cumulative viscoelastic relaxation.

of postseismic deformation observed in India (Figure 6.7).

6.5.4 Back-arc Model

The low-viscosity back-arc region adds southwest oriented deformation under the Andaman Sea, uplift just east of the Andaman Islands, and a broad zone of subsidence between the Andaman transform and rift system and Thailand (Figure 6.16c). There's a slight difference observed at the Thai and Malaysian sites (Figures 6.5, 6.2), but otherwise the GPS station locations are not optimally placed to observe a low-viscosity back-arc spreading center. The Nicobar Islands would be the best location for observing this feature, but we do not have access to postseismic data from those sites. The effects of the low-viscosity zone would

be amplified if we shallow it's upper depth limit or increase the viscosity contrast with the continental mantle.

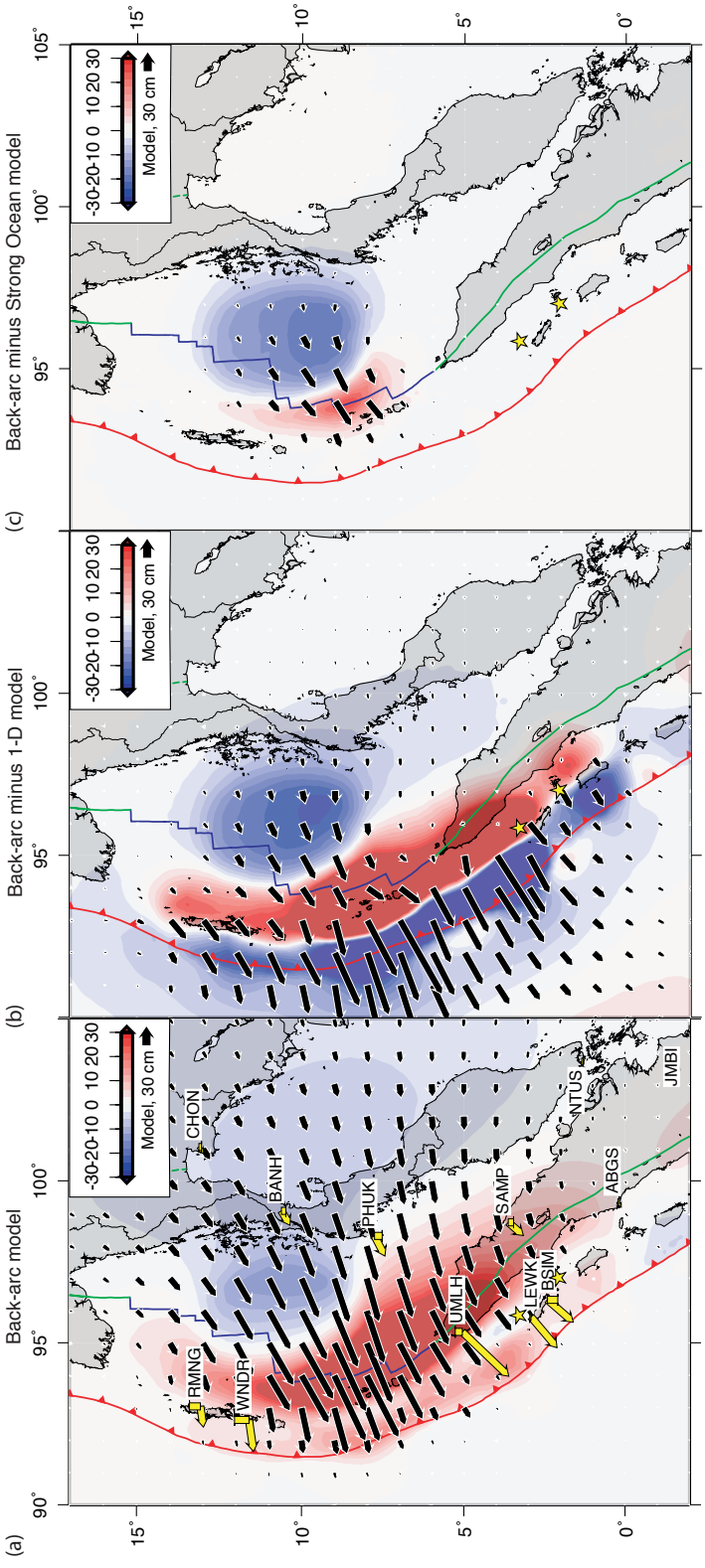

Figure 6.16: a) 5 years of cumulative viscoelastic relaxation following the 2004, 2005, and 2007 megathrust earthquakes using the Back-arc Earth Model. Coseismic displacements for the megathrust earthquakes have been removed from both the model and GPS data. b) The difference between the Back-arc Earth Model and the 1-D Earth Model cumulative viscoelastic relaxation. c) The difference between the Back-arc Earth Model and the Strong Ocean Earth Model cumulative viscoelastic relaxation.

6.6 Discussion and Conclusions

Our exploration of several viscoelastic relaxation models suggests that it is a of first order importance to include a stronger oceanic mantle to fit the postseismic deformation observations following the succession of megathrust earthquakes in Southeast Asia. This allows for one postseismic mechanism to fit the orientation of the observations at sites located in the near-field, intermediate-field and far-field. The early postseismic period after each of the megathrust earthquakes is characterized by a rapidly decaying transient at the near-field sites (see representative site CARI in Figure 6.17). We are not fitting this decaying transient with our linear Maxwell rheology, therefore it may be appropriate to use a bi-viscous rheology that includes a transient viscosity, such as the Burgers body model used by Panet et al. [2010] and Pollitz et al. [2008]. Aseismic afterslip has been observed in many tectonic environments following large earthquakes, although the magnitude and duration of the afterslip varies widely (e.g. Melbourne et al. [2002], Johanson et al. [2006]). Based on the large stresses imparted to the transition zones updip and downdip of the coseismic ruptures, aseismic afterslip is expected to follow the Sunda megathrust earthquakes and could also help to explain the early postseismic transients. Gahalaut et al. [2008] and Paul et al. [2012] have argued that significant afterslip is neccesary to fit the Andaman Island postseismic observations. Based on the first two years of postseismic observations, Gahalaut et al. [2008] argue the Andaman and Nicobar Island deformation can be fit with afterslip downdip of the Andaman coseismic rupture segments, and overlapping with the Car Nicobar and Nicobar Islands rupture segments. They require between ∼1-3 m of afterslip in 2005 and between ∼0.3-1.4 m of slip in 2006, combining to a geodetic moment magntiude of M_w 8.5. Paul et al. [2012] attempts to fit the 2008.5-2010.5 Andaman observations with a combination of viscoelastic relaxation and afterslip. Their preferred model includes ∼ 1 m/yr of afterslip located beneath and downdip of the Andaman Islands, and viscoelastic relaxation assuming a 90-km thick elastic lithosphere and 3×10^{17} Pa s asthenosphere. Their steady-state mantle viscosity is much lower than other studies (e.g. Wang [2007], Panet et al. [2010]) and their model would likely not fit the observations in the far-field. Starting in 2006, our Strong Ocean Model fits the northern and southern Andaman Island and Car Nicobar observations very well, primarily within uncertainties. CARI and HAV2, in the middle Andaman Islands, have unaccounted for uplift and southward motion, suggesting there may still be some localized afterslip or poroelastic rebound. Our models show that it's possible to fit the postseismic observations primarily with viscoelastic relaxation, requiring much less, and shorter duration, afterslip.

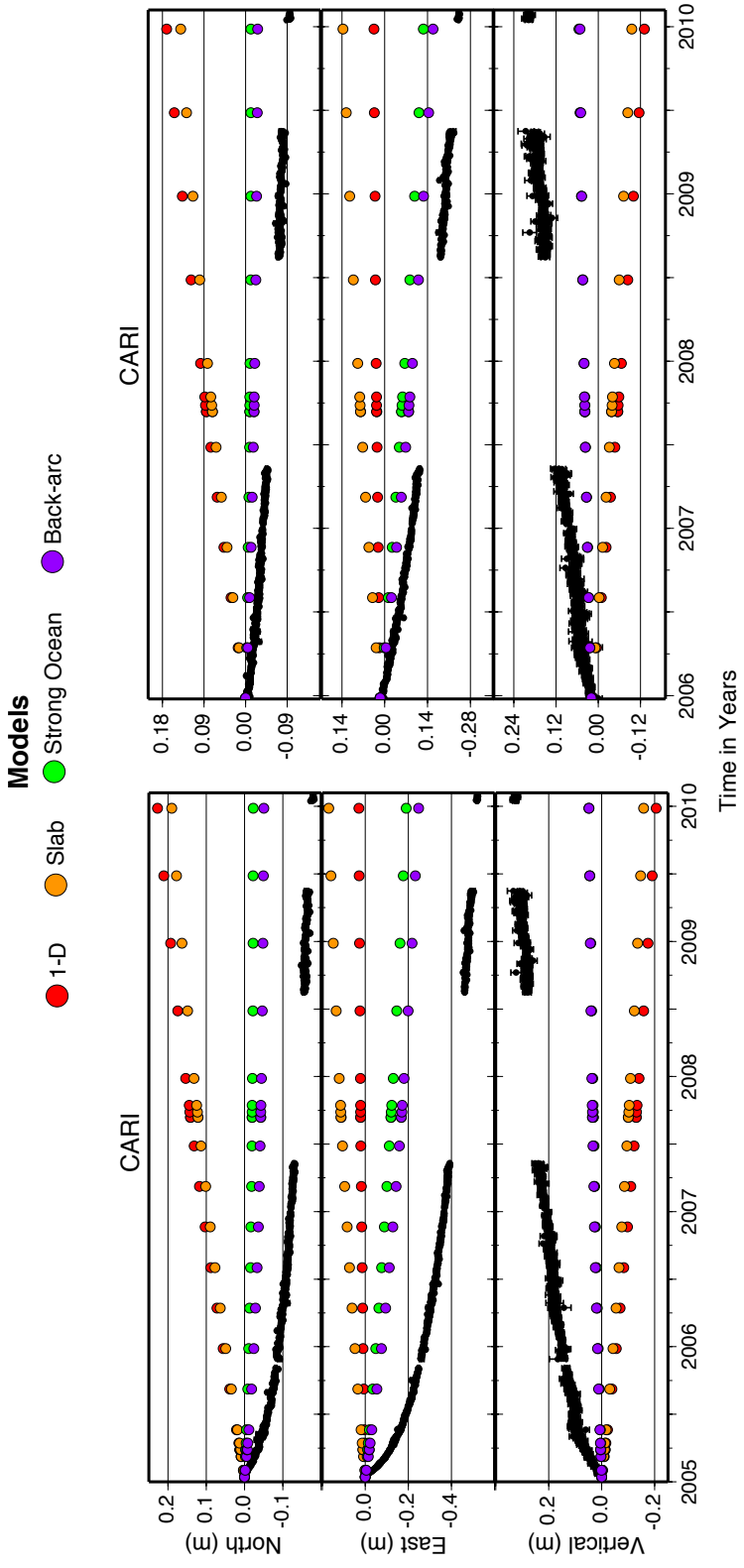

Figure 6.17: Comparison of model fits to the full CARI time series (ANPN GPS network data, processed by Paul et al. [2012]) and time series without the first year of post-2004 earthquake deformation.

Chapter 7

Conclusion and Recommendations

Seismicity levels have increased throughout much of the Sunda subduction zone following the great 2004 Sumatra-Andaman megathrust earthquake. There have been two additional M 8+ megathrust earthquakes, increased levels of seismicity in the upper plate - including the reactivation of the Mentawai backthrust system, increased intraslab seismicity - the largest being the damaging M_w 7.6 2009 Padang earthquake, and two M 8+ strike-slip earthquakes in the incoming India-Australia plate. The obvious questions that come to mind are: are all of these events related to each other and when and where will the next big earthquake occur?

There is no clear answer to the first question, are all these events causally related or just correlated in time and space? Analysis of the stress changes induced by both the coseismic and postseismic deformation from the 2004 Suamtra-Andaman and 2005 Nias megathrust earthquakes indicate that these events were too far away to have triggered the 2007 Bengkulu earthquake - as they produced insignificant stress changes at the 2007 hypocenter. The earlier and smaller 2000 earthquake actually produced larger stress changes at the 2007 hypocenter, and promoted increased seismicity levels in the future 2007 rupture zone for several years. The first Mentawai backthrust cluster started within a week of the 2005 Nias earthquake, however the static stress changes induced by the Nias earthquake were too small to explain the renewed activity, suggesting a dynamic stressing process may have triggered the cluster activity. The 2007 M_w 7.9 earthquake relieved stress on the section of the Mentawai backthrust that slipped in 2005 and enhanced stress on the northern segment - encouraging the 2009 cluster to migrate further northwest. This deep, 2007 Bengkulu aftershock also positively stressed the subducting slab, and is the likeliest triggering event for the 2009 Padang earthquake. The 2004 Sumatra-Andaman earthquake both coseismically and postseismically loaded the incoming oceanic plate for WNW-ESE and NNE-SSW oriented strike-slip faulting, and likely triggered the 2012 M_w 8.6 mainshock. The static stress changes that potentially triggered all of these earthquakes are small, between $\sim 20 - 90\ kPa$, therefore a necessary caveat is that the fault zones needed to be very close to failure at the time of the triggering events.

The next important question is where and when will the next big earthquake occur?

The Siberut section of the Sunda megathrust last participated in a major rupture in 1797 and appears from paleogeodetic evidence to be poised for another great rupture. The 2005 Nias earthquake has stressed the segment from the north, the 2007 Bengkulu earthquake and aftershocks have stressed the segment from the south, the 2009 intraslab earthquake and 2005 and 2009 backthrust clusters have stressed the deeper section between the forearc islands and the west coast of Sumatra. Thus this segment of the subduction zone is the most likely location for the next megathrust earthquake. Analysis of sparse paleogeodetic data have suggested another possible earthquake hazard could be a large backthrust or joint megathrust-backthrust event on the Mentawai segment of the subduction zone, but more data is needed to better constrain the recurrence interval of large Mentawai backthrust earthquakes. Other potential hazards that require further study are the nearby Myanmar and Java subduction zones.

A compilation of geodetic observations from throughout Southeast Asia, spanning the first five years following the 2004 megathrust earthquake, reveals that the far-field sites have already deformed more postseismically than coseismically. It appears the continental Sunda Plate is deforming more than the oceanic India-Australian Plate in response to the megathrust earthquakes, but we are limited to a sparse network of GPS sites west of the trench. I would strongly recommend the installation of oceanic GPS receivers in the Andaman back-arc region, in the Indian Ocean west of the Andaman Islands, and in the Northern Wharton Basin - the location of the 2012 strike-slip earthquakes. 3-D viscoelastic relaxation models suggest it is of first order importance to include a strong oceanic mantle to simultaneously fit the near-field, intermediate-field, and far-field postseismic deformation. However, a linear Maxwell rheology is not fitting the early rapidly decaying transients, and additional research exploring 3-D bi-viscous rheology models, and models with a combination of postseismic processes, are necessary to fit the entire postseismic deformation history.

Bibliography

Abercrombie, R. E., Antolik, M. A., and Ekstrom, G. (2003). The June 2000 M_w 7.9 earthquakes south of Sumatra: Deformation in the India-Austrailia Plate. *J. Geophys. Res.*, 108:B1,2018.

Aki, K. (1966). Generation and propagation of G waves from the Niigata earthquake of June 16, 1964. Part 2. Estimation of earthquake moment, released energy, and stress-strain drop from the G wave spectrum. *Bull. Earthquake Res. Inst., Tokyo Univ.*, 44:73–88.

Apel, E. V. (2011). *Shells on s sphere: tectonic plate motion and plate boundary deformation*. PhD thesis, University of California, Berkeley.

Banerjee, P., Pollitz, F. F., Nagarajan, B., and Bürgmann, R. (2007). Coseismic slip distributions of the 26 December 2004 Sumatra-Andaman and 28 March 2005 Nias earthquakes from gps static offsets. *Bull. Seismol. Soc. Am.*, 97:S86–S102.

Briggs, R. W., Sieh, K., Meltzner, A. J., Natawidjaja, D., Galetzka, J., Suwargadi, B., Hsu, Y., Simons, M., Hananto, N., Suprihanto, I., Prayudi, D., Avouac, J., Prawirodirdjo, L., and Bock, Y. (2006). Deformation and slip along the Sunda megathrust in the great 2005 Nias-Simeulue earthquake. *Science*, 311:1897–1901.

Bürgmann, R., Segall, P., Lisowski, M., and Svarc, J. (1997). Postseismic strain following the 1989 Loma Prieta earthquake from GPS and leveling measurements. *J. Geophys. Res.*, 102:4933–4955.

Cattin, R., Chamot-Rooke, N., Pubellier, M., Rabaute, A., Delescluse, M., Vigny, C., Fleitout, L., and Dubernet, P. (2009). Stress change and effective friction coefficient along the Sumatra-Andaman-Sagaing fault system after the 26 December 2004 ($M_w = 9.2$) and the 28 March 2005 ($M_w = 8.7$) earthquakes. *Geochem. Geophys. Geosys.*, 10:Q03011.

Chauhan, A. P. S., Singh, S. C., Hananto, N. D., Carton, H., Klingelhoefer, F., Dessa, J.-X., Permana, H., White, N. J., Graindorge, D., and Team, S. S. (2009). Seismic imaging of forearc backthrusts at northern Sumatra subduction zone. *Geophys. J. Int.*, 179:1772–1780.

Chlieh, M., Avouac, J., Hjorleifsdottir, V., Song, T. A., Ji, C., Sieh, K., Sladen, A., Hebert, H., Prawirodirdjo, L., Bock, Y., and Galetzka, J. (2007). Coseismic slip and afterslip

of the great M_w 9.15 Sumatra-Andaman earthquake of 2004. *Bull. Seismol. Soc. Am*, 97:S152–S173.

Chlieh, M., Avouac, J. P., Sieh, K., Natawidjaja, D. H., and Galetzka, J. (2008). Heterogenous coupling of the Sumatran megathrust constrained by geodetic and paleogeodetic measurements. *J. Geophys. Res.*, 113:B05305.

Choi, B. H., Hong, S. J., and Pelinovsky, E. (2006). Distribution and runup heights of the December 26, 2004 tsunami in the Indian Ocean. *Geophys. Res. Lett.*, 33:L13601.

Collings, R., Lange, D., Rietbrock, A., Tilmann, F., Natawidjaja, D., Suwargadi, B., Miller, M., and Saul, J. (2012). Structure and seismogenic properties of the Mentawai segment of the Sumatra subduction zone revealed by local earthquake travel-time tomography. *J. Geophys. Res.*, 117:B01312.

Curray, J. (2005). Tectonics and history of the Andaman Sea region. *J. Asian Earth Sci.*, 25:187–232.

Delescluse, M. and Chamot-Rooke, N. (2007). Instantaneous deformation and kinematics of the India-Australia Plate. *Geophys. J. Int.*, 168:818–842.

Delescluse, M., Chamot-Rooke, N., Cattin, R., Fleitout, L., Trubienko, O., and Vigny, C. (2012). April 2012 intra-oceanic seismicity off Sumatra boosted by the Banda-Aceh megathrust. *Nature*, 490:240–244.

Deplus, C. (2001). Indian Ocean Actively Deforms. *Science*, 292:1850–1851.

Deplus, C., Diament, M., Hebert, H., Bertrand, G., Dominguez, S., Dubois, J., Malod, J., Patriat, P., Pontoise, B., and Sibilla, J. (1998). Direct evidence of active deformation in the eastern Indian oceanic plate. *Geology*, 26:131–134.

Diament, M., Harjono, H., Karta, K., Deplus, C., Dahrin, D., Jr., M. T. Z., Gerard, M., Lassal, O., Martin, A., and Malod, J. (1992). Mentawai fault zone off Sumatra: A new key to the geodynamics of western Indonesia. *Geology*, 20:259–262.

Dodge, D. A., Beroza, G. C., and Ellsworth, W. L. (1996). Detailed observations of California foreshock sequences: Implications for the earthquake initiation process. *J. Geophys. Res.*, 101:22,371–22,392.

Dow, J. M., Neilan, R. E., and Rizos, C. (2009). The International GNSS Service in a changing landscape of Global Navigation Satellite Systems. *J. of Geodesy*, 83:191–198.

Dziewonski, A. M. and Anderson, D. L. (1981). Preliminary reference earth model. *Phys. Earth Planet. Int.*, 25:297–356.

Engdahl, E. R., Villasenor, A., DeShon, H. R., and Thurber, C. H. (2007). Teleseismic relocation and assessment of seismicity (1918-2005) in the region of the 2004 M_w 9.0 Sumatra-Andaman and 2005 M_w 8.6 Nias Island great earthquakes. *Bull. Seismol. Soc. Am*, 97:S43–S61.

Fauzi, McCaffrey, R., Wark, D., Sunaryo, and Haryadi, P. Y. P. (1996). Lateral variation in slab orientation beneath Toba Caldera, northern Sumatra. *Geophys. Res. Lett.*, 23:443–446.

Felzer, K. R., Becker, T. W., Abercrombie, R. E., Ekström, G., and Rice, J. R. (2002). Triggering of the 1999 M_w 7.3 Hector mine earthquake by aftershocks of the 1992 M_w 7.3 Landers earthquake. *J. Geophys. Res.*, 107:2190.

Fialko, Y. (2004). Evidence of fluid-filled upper crust from observations of postseismic deformation due to the 1992 M_w 7.3 Landers earthquake. *J. Geophys. Res.*, 109:B08401.

Fitch, T. J. (1972). Plate convergence, transcurrent faults, and internal deformation adjacent to Southeas Asia and Western Pacific. *J. Geophys. Res.*, 77:4432–4460.

Freed, A. M. (2005). Earthquake triggering by static, dynamic, and postseismic stress transfer. *Annu. Rev. Earth Planet. Sci.*, 33:335–367.

Gahalaut, V. (2005). 28 March 2005 Sumatra earthquake: Expected, triggered or aftershock? *Curr. Science*, 89:452–454.

Gahalaut, V. K., Jade, S., Catherine, J. K., Gireesh, R., Ananda, M. B., Kumar, P. D., Narsaiah, M., Jafri, S. S. H., Ambikapathy, A., Bansal, A., Chadha, R. K., Gupta, D. C., Nagarajan, B., and Kumar, S. (2008). Gps measurements of postseismic deformation in the Andaman-Nicobar region following the giant 2004 Sumatra-Andaman earthquake. *J. Geophys. Res.*, 113:B08401.

Goldfinger, C., Grijalva, K., Bürgmann, R., Morey, A. E., Johnson, J. E., Nelson, C. H., Gutierrez-Pastor, J., Ericsson, A., Karabanov, E., Chaytor, J. D., Patton, J., and Gracia, E. (2008). Late holocene rupture of the northern San Andreas Fault and possible stress linkage to the Cascadia Subduction Zone. *Bull. Seismol. Soc. Am.*, 98:861–889.

Hartzell, S. H. and Heaton, T. H. (1983). Inversion of strong ground motion and teleseismic waveform data for the fault rupture history of the 1979 Imperial Valley, California, earthquake. *Bull. Seism. Soc. Am.*, 73:1553–1583.

Hayes, G. P. and Wald, D. J. (2009). Developing framework to constrain the geometry of the seismic rupture plane of subduction interface a priori - a probabilistic approach. *Geophys. Journal International*, 176:951–964.

Hayes, G. P., Wald, D. J., and Johnson, R. L. (2012). Slab1.0: A three-dimensional model of global subduction zone geometries. *J, Geophys. Res.*, 117:B01302.

Hermawan, I. (2010). *Sismotectonique des failles actives en Indonesie, vue par geodesie spatiale*. PhD thesis, Ecole Normale Superieure, Paris.

Herring, T. A. (2005). *GLOBK, Global Kalman filter VLBI and GPS analysis program*. Massachusetts Institute of Technology, release 10.2 edition.

Hill, E. M., Borrero, J. C., Huang, Z., Qiu, Q., Banerjee, P., Natawidjaja, D. H., Elosegui, P., Fritz, H. M., Suwargadi, B., Pranantyo, I. R., Li, L., Macpherson, K. A., Skanavis, V., Synolakis, C. E., and Sieh, K. (2012). The 2010 mw 7.8 Mentawai earthquake: Very shallow source of a rare tsunami earthquake determined from tsuanmi field survey and near-field GPS data. *J. Geophys. Res.*, 117:B06402.

Hough, S. E. (2005). Remotely triggered earthquakes following moderate mainshocks (or, why California is not falling into the ocean). *Seismol. Res. Lett.*, 76:58–66.

Hsu, Y., Simons, M., Avouac, J., Galetzka, J., Sieh, K., Chlieh, M., Natawidjaja, D., Prawirodirdjo, L., and Bock, Y. (2006). Frictional afterslip following the 2005 Nias-Simeulue earthquake, Sumatra. *Science*, 312:1921–1926.

Ichinose, G. A., Thio, H. K., and Somerville, P. G. (2004). Rupture process and near-source shaking of the 1965 Seattle-Tacoma and 2001 Nisqually, intraslab earthquakes. *Geophys. Res. Lett.*, 31:L10604.

Johanson, I. A., Fielding, E. J., Rolandone, F., and Burgmann, R. (2006). Coseismic and postseismic slip of the 2004 Parkfield earthquake from space-geodetic data. *Bull. Seismol. Soc. Am.*, 96:S1–S13.

Kaverina, A., Dreger, D., and Price, E. (2002). The combined inversion of seismic and geodetic data for the source process of the 16 October 1999 mw 7.1 Hector Mine, California, earthquake. *Bull. Seism. Soc. Am.*, 92:1266–1280.

King, R. and Bock, Y. (2005). *Documentation for the GAMIT GPS analysis software*. Massachusetts Institute of Technology, Scripps Institute of Oceanography, release 10.2 edition.

Konca, A. O., Avouac, J., Sladen, A., Meltzner, A. J., Sieh, K., Fang, P., Li, Z., Galetzka, J., Genrich, J., Chlieh, M., Natawidjaja, D. H., Bock, Y., Fielding, E. J., Ji, C., and Helmberger, D. V. (2008). Partial rupture of a locked patch of the Sumatra megathrust during the 2007 earthquake sequence. *Nature*, 465:631–635.

Konca, A. O., Hjorleifsdottir, V., Song, T. A., Avouac, J., Helmberger, D. V., Ji, C., Sieh, K., Briggs, R., and Meltzner, A. (2007). Rupture kinematics of the 2005 M_w 8.6 Nias-Simeulue earthquake from the joint inversion of seismic and geodetic data. *Bull. Seismol. Soc. Am*, 97:S307–S322.

Kositsky, A. P. and Avouac, J.-P. (2010). Inverting geodetic time series with a principal component analysis-based inversion method. *J. Geophys. Res.*, 115:B03401.

Lange, D., Tilmann, F., Riebrock, A., Collings, R., Natawidjaja, D. H., Suwargadi, B. W., Barton, P., Henstock, T., and Ryberg, T. (2010). The fine structure of the subducted investigator fracture zone in Western Sumatra as seen by local seismicity. *EPSL*, 298:47–56.

Lay, T., Ammon, C. J., Kanamori, H., Kim, M. J., and Xue, L. (2011a). Outer trench-slope faulting and the 2011 Mw 9.0 off the Pacific coast of Tohoku earthquake. *Earth Planets Space*, 63:713–718.

Lay, T., Ammon, C. J., Kanamori, H., Xue, L., and Kim, M. J. (2011b). Possible large near-trench slip during the 2011 Mw 9.0 off the Pacific coast Tohoku earthquake. *Earth Planets Space*, 63:687–692.

Lin, J. and Stein, R. S. (2004). Stress triggering in thrust and subduction earthquakes, and stress interaction between the southern San Andreas and nearby thrust and strike-slip faults. *J. Geophys. Res.*, 109:B02303.

Liu, C. (1983). New constraints on the tectonic evolution of the eastern Indian Ocean. *EPSL*, 65:331–342.

Masterlark, T. (2003). Finite element model predictions of static deformation from dislocation sources in a subduction zone: Sensitivities to homogeneous isotropic, Poisson-solid, and half-space assumptions. *J. Geophys. Res.*, 108:2540.

Masterlark, T., DeMets, C., Wang, H. F., Sanchez, O., and Stock, J. (2001). Homogenous vs heterogeneous subduction zone models: Coseismic and postseismic deformation. *Geophys. Res. Lett.*, 28:4047–4050.

McCaffrey, R. (1991). Slip vectors and stretching of the Sumatran Fore Arc. *Geology*, 19:881–884.

McCloskey, J., Lange, D., Tilmann, F., Nalbant, S. S., Bell, A. F., Natawidjaja, D. H., and Rietbrock, A. (2010). The September 2009 Padang earthquake. *Nature Geosci.*, 3:70–71.

McCloskey, J., Nalbant, S. S., and Stacy, S. (2005). Earthquake risk from co-seismic stress. *Nature*, 434:291.

McGuire, J. and Beroza, G. (2012). A rogue earthquake off Sumatra. *Science*, 336:1118–1119.

Melbourne, T. I., Webb, F. H., Stocl, J. M., and Reigber, C. (2002). Rapid postseismic transients in subduction zones from continuous GPS. *J. Geophys. Res.*, 107:2241.

Meltzner, A. J., Sieh, K., Chiang, H.-W., Shen, C.-C., Suwargadi, B. W., Natawidjaja, D. H., Philibosian, B., and Briggs, R. W. (2012). Persistent Termini of the 2004-and 2005-like Ruptures of the Sunda Megathrust. *J. Geophys. Res.*, 117:B04405.

Meltzner, A. J., Sieh, K., Chiang, H.-W., Shen, C.-C., Suwargadi, B. W., Natawidjaja, D. H., Philibosian, B. E., Briggs, R. W., and Galetzka, J. (2010). Coral evidence for earthquake recurrence and an A.D. 1390-1455 cluster at the south end of the 2004 Aceh-Andaman rupture. *J. Geophys. Res.*, 115:B10402.

Meng, L., Ampuero, J.-P., Stock, J., Duputel, Z., Luo, Y., and Tsai, V. (2012). Earthquake in a maze:compressional rupture branching during the April 11 2012 M8.6 Sumatra earthquake. *Science*, 337:724–726.

Müller, R. D., Roest, W. R., Royer, J.-Y., Gahagan, L. M., and Sclater, J. G. (1997). Digital isochrons of the world's ocean floor. *J. Geophys. Res.*, 102:3211–3214.

Nalbant, S. S., Stacy, S., Sieh, K., Natawidjaja, D., and McCloskey, J. (2005). Earthquake risk on the Sunda trench. *Nature*, 435:756–757.

Natawidjaja, D., Sieh, K., Ward, S., Cheng, H., Edwards, R., Galetzka, J., and Suwargadi, B. (2004). Paleogeodetic records of seismic and aseismic subduction from central Sumatran microatolls, Indonesia. *109*, 109:B04306.

Natawidjaja, D. H., Sieh, K., Chlieh, M., Galetzka, J., Suwargadi, B. W., Cheng, H., Edwards, R. L., Avouac, J., and Ward, S. N. (2006). Source parameters of the great Sumatran megathrust earthquakes of 1797 and 1833 inferred from coral microatolls. *J. Geophys. Res.*, 111:B06403.

Ogawa, R. and Heki, K. (2007). Slow postseismic recovery of geoid depression formed by the 2004 Sumatra-Andaman earthquake by mantle water diffusion. *Geophys. Res. Lett.*, 34:L06313.

Okada, Y. (1985). Surface deformation due to shear and tensile faults in a half-space. *Bull. Seismol. Soc. Am.*, 75:1135–1154.

Panet, I., Pollitz, F., Mikhailov, V., Diament, M., Banerjee, P., and Grijalva, K. (2010). Upper mantle rheology from GRACE and GPS postseismic deformation after the 2004 Sumatra-Andaman earthquake. *Geochem. Geophys. Geosys.*, 11:Q06008.

Panumastrakul, E., Simons, W. J. F., and Satirapod, C. (2012). Modeling post-seismic displacements in Thai geodetic network due to the Sumatra-Andaman and Nias earthquakes using GPS observations. *Survey Review*, 44:72–77.

Paul, J., Lowry, A. R., Bilham, R., Sen, S., and Smalley, R. (2007). Postseismic deformation of the Andaman Islands following the 26 december, 2004 Great Sumatra-Andaman earthquake. *Geophys. Res. Lett.*, 34:L19309.

Paul, J., Rajendran, C. P., Lowry, A. R., Andrade, V., and Rajendran, K. (2012). Andaman postseismic deformation observations: Still slipping after all these years? *Bull. Seismol. Soc. Am.*, 102:343–351.

Perfettini, H., Stein, R. S., Simpson, R., and Cocco, M. (1999). Stress transfer by the 1988-1989 M = 5.3 and 5.4 Lake Elsman foreshocks to the Loma Prieta fault: Unclamping at the site of peak mainshock slip. *J. Geophys. Res.*, 104:20,169–20,182.

Pesicek, J. D., Thurber, C. H., Zhang, H., DeShon, H. R., Engdahl, E. R., and Widiyantoro, S. (2010). Teleseismic double-difference relocation along the Sumatra-Andaman subduction zone using a 3-d model. *J. Geophys. Res.*, 115:B10303.

Plafker, G., Nishenko, S., Cluff, L., and Syharial, D. (2006). The cataclysmic 2004 tsunami on NW SumatraPreliminary evidence for a play fault secondary source along the western Aceh basin. *Seismol. Res. Lett.*, 77:231.

Pollitz, F., Banerjee, P., Bürgmann, R., Hashimoto, M., and Chhoosakul, N. (2006a). Stress changes along the Sunda trench following the 26 December 2004 Sumatra-Andaman and 28 March 2005 Nias earthquakes. *Geophys. Res. Lett.*, 33:L06309.

Pollitz, F. F. (1992). Postseismic relaxation theory on the spherical earth. *Bull. Seismol. Soc. Am.*, 82:422–453.

Pollitz, F. F. (1996). Coseismic deformation from earthquake faulting on a layered spherical earth. *Geophys. J. Int.*, 125:1–14.

Pollitz, F. F., Banerjee, P., Grijalva, K., Nagarajan, B., and Bürgmann, R. (2008). Effect of 3-D viscoelastic structure on post-seismic relaxation from the 2004 M = 9.2 Sumatra earthquake. *Geophys. J. Int.*, 173:189–204.

Pollitz, F. F., Bürgmann, R., and Banerjee, P. (2006b). Post-seismic relaxation following the great 2004 Sumatra-Andaman earthquake on a compressible self-gravitating Earth. *Geophys. J. Int.*, 167:397–420.

Prawirodirdjo, L., McCaffrey, R., Chadwell, C. D., Bock, Y., and Subarya, C. (2010). Geodetic observations of an earthquake cycle at the Sumatra subduction zone: Role of interseismic strain segmentation. *J. Geophys. Res.*, 115:B03414.

Reasenberg, P. (1985). Second-order moment of central California seismicity 1969-1982. *J. Geophys. Res.*, 90:5479–5495.

Reasenberg, P. A. and Simpson, R. W. (1992). Response of regional seismicity to the static stress change produced by the Loma Prieta earthquake. *Science*, 255:1687–1690.

Rubinstein, J. L., Gomberg, J., Vidale, J., Wech, A., Kao, H., Creager, K., and Rogers, G. (2009). Seismic wave triggering of nonvolcanic tremor, episodic tremor and slip, and earthquakes on Vancouver Island. *J. Geophys. Res.*, 114:B00A01.

Rydelek, P. A. and Sacks, I. S. (1999). Large earthquake occurrence affected by small stress changes. *Bull. Seismol. Soc. Am.*, 89:822–828.

Sager, W. W., Paul, C. F., Krishna, K. S., Pringle, M., Eisin, A. E., Frey, F. A., Rao, D. G., and Levchenko, O. (2010). Large fault fabric of the Ninetyeast Ridge implies near-spreading ridge formation. *Geophys. Res. Lett.*, page L17304.

Saikia, C. K. (1994). Modified frequency-wave number algorithm for regional seismograms using Filon's quadrature-modeling of L(g) waves in eastern North America. *Geophys. J. Int.*, 118:142–158.

Satriano, C., Kiraly, E., Bernard, P., and Vilotte, J.-P. (2012). The 2012 Mw 8.6 Sumatra earthquake: Evidence of westward sequential seismic ruptures associated to the reactivation of a N-S ocean fabric. *Geophy. Res. Lett.*, page L15302.

Scholz, C. H. (2010). Large earthquake triggering, clustering, and the synchronization of faults. *Bull. Seism. Soc. Am.*, 100:901–909.

Sevilgen, V., Stein, R. S., and Pollitz, F. F. (2012). Stress imparted by the great 2004 Sumatra quake shut down transforms and activated rifts up to 400 km away in the Andaman Sea. *Proc. Natl. Acad. Sci.*, 109:15152–15156.

Shapiro, N., Ritzwoller, M., and Engdahl, E. (2008). Structural context of the great Sumatra-Andaman Islands earthquake. *Geophys. Res. Lett.*, 35:L05301.

Shearer, P. and Bürgmann, R. (2010). Lessons learned from the 2004 Sumatra-Andaman megathrust rupture. *An. Rev. Earth Planet. Sci.*, 38:103–131.

Sieh, K. and Natawidjaja, D. (2000). Neotectonics of the Sumatran fault, Indonesia. *J. Geophys. Res.*, 105:28,295–28,326.

Sieh, K., Natawidjaja, D. H., Meltzner, A. J., Shen, C., Cheng, H., Li, K., Suwargadi, B. W., Galetzka, J., Philibosian, B., and Edwards, R. L. (2008). Earthquake supercycles inferred from sea-level changes recorded in the corals of West Sumatra. *Science*, 322:1674–1678.

Simons, W. J. F., Socquet, A., Vigny, C., Ambrosius, B. A. C., Abu, S. H., Promthong, C., Subarya, C., Sarsito, D. A., Matheussen, S., Morgan, P., and Spakman, W. (2007). A decade of GPS in Southeast Asia: resolving Sundaland motion and boundaries. *J. Geophys. Res.*, 112:B06420.

Singh, S. C., Carton, H., Chauhan, A. S., Androvandi, S., Davaille, A., Dyment, J., Cannat, M., and Hananto, N. D. (2011a). Extremely thin crust in the Indian Ocean possibly resulting from Plume-Ridge Interaction. *Geophys. J. Int.*, 184:29–42.

Singh, S. C., Hananto, N. D., and Chauhan, A. P. S. (2011b). Enhanced reflectivity in the recent great Sumatran earthquake rupture zones. *Geophys. Res. Lett.*, 38:L04302.

Singh, S. C., Hananto, N. D., Chauhan, A. P. S., Permana, H., Denolle, M., Hendriyana, A., and Natawidjaja, D. (2010). Evidence of active backthrusting at the NE margin of Mentawai Islands, SW Sumatra. *Geophys. J. Int.*, 180:703–714.

Somerville, P. G., Irikura, K., Graves, R., Sawada, S., Wald, D., Abrahamson, N., Iwasaki, Y., Kagawa, T., Smith, N., and Kowada, A. (1999). Characterizing crustal earthquake slip models for the prediction of strong ground motion. *Seism. Res. Lett.*, 70:59–80.

Stein, R. S. (1999). The role of stress transfer in earthquake occurence. *Nature*, 402:605–609.

Subarya, C., Chlieh, M., Prawirodirdjo, L., Avouac, J., Bock, Y., Sieh, K., Meltzner, A. J., Natawidjaja, D. H., and McCaffrey, R. (2006). Plate-boundary deformation associated with the great Sumatra-Andaman earthquake. *Nature*, 440:46–51.

Suppe, J. (2007). Absolute fault and crustal strength from wedge tapers. *Geology*, 35:1127–1130.

Tilmann, F. J., Craig, T. J., Grevemeyer, I., Suwargadi, B., Kopp, H., and Flueh, E. (2010). The updip seismic/aseismic transition of the Sumatra megathrust illuminated by aftershocks of the 2004 Aceh-Andaman and 2005 Nias events. *Geophys. J. Int.*, 181:1261–1274.

Toda, S., Lin, J., and Stein, R. S. (2011). Using the 2011 m=9.0 tohoku earthquake to test the Coulomb stress triggering hypothesis and to calculate faults brought closer to failure. *Earth Planets Space*, 63:725–730.

Toda, S., Stein, R. S., Richards-Dinger, K., and Bozkurt, S. (2005). Forecasting the evolution of seismicity in southern California: Animations built on earthquake stress transfer. *J. Geophys. Res.*, 110:B05S16.

Vallée, M., Bouchon, M., and Schwartz, S. Y. (2003). The 13 January El Salvador earthquake: A multidata analysis. *J. Geophys. Res.*, 108:2203.

Vigny, C., Simons, W. J. F., Abu, S., Bamphenyu, R., Satirapod, C., Choosakul, N., Subarya, C., Socquet, A., Omar, K., Abidin, H. Z., and Ambrosius, B. A. C. (2005). Insight into the 2004 Sumatra-Andaman earthquake from GPS measurements in southeast asia. *Nature*, 436:201–206.

Wada, I., Mazzotti, S., and Wang, K. (2010). Intraslab stresses in the Cascadia subduction zone from inversion of earthquake focal mechanisms. *Bull. Seismol. Soc. Am.*, 100:2002–2013.

Wang, K. (2007). Elastic and viscoelastic models of crustal deformation in subduction earthquake cycles. In Dixon, T. H. and Moore, J. C., editors, *The Seismogenic Zone of Subduction Thrust Faults*. Columbia University Press.

Wang, K. and He, J. (1999). Mechanics of low-stress forearcs: Nankai and Cascadia. *J. Geophys. Res.*, 104:15,191–15,205.

Wang, K., Mulder, T., Rogers, G. C., and Hyndman, R. D. (1995). Case for very low coupling stress on the Cascadia subduction fault. *J. Geophys. Res.*, 100:12,907–12,918.

Wang, R., Martin, F. L., and Roth, F. (2003). Computation of deformation induced by earthquakes in a multi-layered elastic crust - FORTRAN programs EDGRN/EDCMP. *Computers and Geosciences*, 29:195–207.

Wells, D. L. and Coppersmith, K. J. (1994). New empirical relationship among magnitude, rupture length, rupture width, rupture area, and surface displacement. *Bull. Seism. Soc. Am.*, 84(4):974–1002.

Wiemer, S. (2001). A software package to analyze seismicity: ZMAP. *Seismol. Res. Lett.*, 72:373–382.

Wiseman, K., Banerjee, P., Bürgmann, R., Sieh, K., , Dreger, D., and Hermawan, I. (2012). Source model of the 2009 Mw 7.6 Padang intraslab earthquake and its effect on the Sunda megathrust. *Geophys. J. Int.*, 190:1710–1722.

Wiseman, K., Banerjee, P., Sieh, K., Bürgmann, R., and Natawidjaja, D. H. (2011). Another potential source of destructive earthquakes and tsunami offshore of sumatra. *Geophys. Res. Lett.*, 38:L10311.

Wiseman, K. and Bürgmann, R. (2011). Stress and seismicity changes on the Sunda megathrust preceding the 2007 Mw 8.4 earthquake. *Bull. Seismol. Soc. Am.*, 101:313–326.

Wiseman, K. and Bürgmann, R. (2012). Stress triggering of the great Indian Ocean strike-slip earthquakes in a diffuse plate boundary zone. *Geophys. Res. Lett.*, 39.

Yue, H., Lay, T., and Koper, K. (2012). En echelon and orthogonal fault ruptures of the 11 April 2012 great intraplate earthquakes. *Nature*, 490:245–249.

Zachariasen, J. (1998). *Paleoseismology and paleogeodesy of the Sumatran subduction zone: A study of vertical displacement using coral microatolls*. PhD thesis, Calif. Inst. of Technol., Pasadena.

Zhou, Y. H., Xu, L. S., and Chen, Y. T. (2002). Source process of the 4 June 2000 southern Sumatra, Indonesia, earthquake. *Bull. Seismol. Soc. Am.*, 92:2027–2035.